NON-INVASIVE QUANTIFICATION OF CARDIOVASCULAR FLOW METRICS IN VERTEBRATES

by

Sreyashi Chakraborty

A Dissertation

Submitted to the Faculty of Purdue University

In Partial Fulfillment of the Requirements for the degree of

Doctor of Philosophy

School of Mechanical Engineering

West Lafayette, Indiana

May 2021

THE PURDUE UNIVERSITY GRADUATE SCHOOL
STATEMENT OF COMMITTEE APPROVAL

Dr. Pavlos P. Vlachos, Chair

Department of Mechanical Engineering

Dr. Marisol S. Sepúlveda

Department of Forestry and Natural Resources

Dr. Eric A. Nauman

Department of Mechanical Engineering

Dr. Arezoo M. Ardekani

Department of Mechanical Engineering

Approved by:

Dr. Nicole Key

Dedicated to Shirdi Sai Baba, Brahmarishi Mohanji, Ma, and Tarak

ACKNOWLEDGMENTS

I am deeply grateful to Professor Vlachos for giving me the opportunity to work in several cutting-edge research projects and improve my expertise on a plethora of topics and techniques. His support and kindness in the last year gave me strength to pick myself up inspite of my sickness and finish this journey. I would like to thank Professor Sepulveda and her student Elizabeth Allmon for their constant encouragement and collaboration in the medaka project. Professor Nauman and Professor Ardekani have given invaluable feedback at early stages of my PhD that shaped my critical reasoning ability. Professor Rylander and her student Alican Ozkan have been instrumental in improving the work on nanoparticle transport. I have the fondest memories of my fellow graduate students in Aether Lab. There are not enough words to thank them for their kindness every time I went through a crisis. I would like to thank Sayantan, Brian, Tianqi, Adib, Javad, Lalit, Jiacheng, Brett, Melissa and Rozhin for the many fun conversations in the office that made frequent failures more bearable. I would specially thank Sayantan for being an awesome friend as well and bringing groceries, cooked food, typing documents during the period of my sickness.

My parents and my husband, Tarak, have made tremendous sacrifices in the last year so that I could reach this finish line. They are the reason I did not give up even when quitting looked like the best option. Tarak and both my parents have risked their own career to cook, clean, look after me multiple times a day even when there was no sign of improvement of my condition. My little nephew Krish has been a source of eternal joy throughout these ups and downs.

My soul family all over the world have sent me positive vibes and healing energies till I could step out on my own again. My next goal in life to be as loving and compassionate as them.

I nurture eternal gratitude towards my beloved Guru Brahmarishi Mohanji and Shirdi Saibaba for reconnecting me back to my spirit. I experienced the joy of complete freedom only after I surrendered my mind, body and soul to the Divine.

Finally, I would like to thank and cheer the loudest for the loving pair of eyes that stared back at me everytime I looked into the mirror. Thank You for always choosing Hope and Love in the face of every storm that comes your way.

I hope this PhD work embodies this spirit of healing and be a stepping-stone for development of clinical tools that accelerate diagnosis and treatment of serious medical conditions.

TABLE OF CONTENTS

LIST OF TABLES 9
LIST OF FIGURES 10
ABSTRACT 15
1. MIXTURE THEORY MODELING FOR CHARACTERIZING SOLUTE TRANSPORT IN BREAST TUMOR TISSUES 17
1.1 Abstract 17
1.2 Background 18
1.3 Results 20
1.3.1 Test 1: Effect of solute size in three configurations for fixed intercapillary separation 21
1.3.2 Test 2: Effect of flow direction in microvessels 22
1.3.3 Test 3: Effect of intercapillary separation on transport of 3 kDa and 10 kDa solutes 23
Double Blood Capillary (2 BC) embedded in tissue cylinder 25
Blood Capillary and Lymph Capillary (BC_LC) embedded in tissue cylinder 26
Non-dimensional Time vs Peak Non-dimensional Concentration Analysis 26
1.4 Discussion 27
1.5 Conclusions 30
1.6 Methods 30
1.6.1 Mixture Theory Model Parameters 30
1.6.2 Experimental Validation of Mixture Theory Model 31
1.6.3 Experimental and numerical comparison of concentration-time histories 31
1.6.4 Vascular Tissue Configurations and Test Matrix 33
Test 1: Effect of solute size on transport 33
Test 2: Effect of flow direction in capillaries on transport 33
Test 3: Effect of intercapillary separation on transport 34
1.6.5 Non-Dimensionalization of the Convection-Diffusion-Decay process 35
1.7 Declarations 36
1.7.1 Competing Interests 36
1.7.2 Funding 36
1.7.3 Authors' Contributions 37
1.7.4 Acknowledgement 37

1.8 Appendix 38
2. A WAVELET APPROACH FOR THE ESTIMATION OF LEFT VENTRICULAR EARLY FILLING WAVE PROPAGATION VELOCITY FROM COLOR-M-MODE ECHOCARDIOGRAMS 45
2.1 Abstract 45
2.2 Introduction 46
2.3 Materials and Methods 47
2.3.1 CMM Acquisition 47
Patient Cohorts 48
2.3.2 Continuous Wavelet Transform Applied on Wave Propagation Velocity 49
2.3.3 Calculating Wave Component Propagation Velocity 51
2.3.4 Conventional Propagation Velocity (V_p) and Filling Strength (V_s) 52
2.3.5 CMM Derived IVPD 53
2.3.6 Intra-Operator and Inter-Operator Variability Analysis 53
2.3.7 Statistical analysis 53
2.4 Results 54
2.4.1 Intra-Operator and Inter-Operator Variability Analysis 54
2.4.2 Group A: Diastolic Dysfunction 55
2.4.3 Group B: Dependence on Left Ventricle Geometry 56
2.5 Discussion 58
2.6 Acknowledgements 62
2.7 Appendix 63
3. HEMODYNAMIC DEPENDENCE OF MECHANO-GENETIC EVOLUTION OF THE CARDIOVASCULAR SYSTEM IN JAPANESE MEDAKA 65
3.1 Abstract 65
3.2 Introduction 65
3.3 Results and Discussion 68
3.3.1 Cardiac function and geometry 68
3.3.2 Hematocrit, viscosity and shear rate in the ventricle 70
3.3.3 Spatial Velocity profile in AVC and OFT 71
3.3.4 Velocity and WSS measurement in AVC and OFT 72
3.3.5 Area, velocity and WSS measurement in tail vessels 74
3.3.6 Gene expressions from qRT-PCR analysis 77

3.3.7 Correlation between peak WSS and gene expression along fish age progression 77
3.3.8 Effect of WSS magnitude and retrograde flow on cardiac landmarks along fish age progression 78
3.3.9 Relation of gene expression with cardiac landmarks along fish age progression 79
3.3.10 Relation of Cardiac flow with Vascular flow along fish age progression 80
3.4 Conclusion 81
3.5 Author contributions 82
3.6 Methods 82
3.6.1 Japanese Medaka husbandry and embryo collection 82
3.6.2 Fish Selection for Imaging and gene expression 82
3.6.3 Data Acquisition 83
3.6.4 Flow velocity analysis in heart 83
Signal amplification of raw images 83
Heart function measurement 83
3.6.5 μPIV analysis 84
Velocity measurement location in medaka 84
3.6.6 WSS analysis in AVC and OFT 85
Wall position calculation 85
WSS calculation 86
Hematocrit (Ht) calculation 87
Viscosity (μ) calculation 88
WSS measurement 88
3.6.7 Flow and WSS analysis in vessels 88
3.6.8 qPCR analysis of gene expression profiles 89
3.7 Statistical Analysis 90
3.7.1 Cardiac Function and geometry 90
3.7.2 Hematocrit, viscosity and shear rate in the ventricle 92
3.7.3 Cardiac gene expression 94
4. EVOLUTION OF CARDIAC TISSUE AND FLOW MECHANICS IN DEVELOPING JAPANESE MEDAKA 97
4.1 Abstract 97
4.2 Introduction 97
4.3 Results 99

4.3.1 Cardiac function and geometry 99
4.3.2 Pressure contours across the AVC and the OFT 99
4.3.3 Time variation of pressure drop across AVC and OFT 102
4.3.4 Strain measurements of the ventricle wall 103
4.3.5 EW measurement from ΔPAVC-strain loop 104
4.3.6 Peak EW, peak ΔP at AVC, OFT and peak diastolic strain measurement 105
4.4 Discussion 107
4.5 Limitations 108
4.6 Conclusion 108
4.7 Methods 109
4.7.1 Velocity reconstruction across the AVC and the OFT 109
4.7.2 Pressure analysis of the cardiac chambers 109
4.7.3 Strain analysis of the ventricle wall 110
4.7.4 EW measurement of the ventricle 111
4.8 Statistical Analysis 111
REFERENCES 113

LIST OF TABLES

Table 1-1: Input parameters for mixture theory model. Values are for different types of cancer tissues adopted from the literature. References are listed in the last column of table. 20

Table 1-2: Intercapillary distance from invivo tissues with capillary diameter, d=10 $\boldsymbol{\mu m}$ 26

Table 1-3: Parameters from the fabricated tissue platform used in equivalent simulation..... 32

Table 1-4: Test matrix developed for conducting the study 34

Table 1-5: Solute dependent timescales that influence concentration in tissue across time..... 36

Table 2-1: Group A patient characteristics 48

Table 2-2: Group B patient characteristics 49

Table 2-3: Results of intra-observer variability and inter-observer variability for each parameter. Peak-V_W reports the smallest variability when compared to conventional parameters. 53

Table 2-4: Summary of results for Group A. 54

Table 2-5: p-values from Tukey-Kramer HSD test for Group A. The shaded values signify statistical significance. The wavelet based peak propagation velocity has highest statistical significance. 55

Table 2-6: Summary of results for Group B. 57

Table 3-1: Comparison of cardiac development times in zebrafish and japanese medaka 79

Table 3-2: List of primers used for real time PCR. All sequences are 5′ to 3′ and reverse primers are reverse compliments of the genetic sequence. 89

Table 3-3: P-values from Tukey Kramer HSD tests comparing heart rate (HR), Reynolds number (Re) and Womersley number (Wo) at the atrial inflow, end-diastolic ventricle area (A), ventricle ejection fraction (EF) and fractional ventricle diastolic time (t_{diast}/T) between each pair of dpfs. n=5 for each dpf. *** denotes p<0.0001. ** denotes p<0.001. * denotes p<0.05..... 91

Table 3-4: P-values from Tukey Kramer HSD tests comparing hematocrit (Ht), viscosity (μ), peak shear rate (γ) and peak wall shear stress (WSS) at the atrioventricular canal (AVC), peak WSS at ventricle outflow tract (OFT) between each pair of dpfs. n=5 at each dpf. *** denotes p<0.0001. ** denotes p<0.001. * denotes p<0.05..... 93

Table 3-5: p-values from Tukey Kramer HSD test comparing relative gene expressions of *fgf8, hoxb6b, nkx2.5, bmp4* and *smyd1* between each pair of dpfs. n=8-10 at each dpf. *** denotes p<0.0001. ** denotes p<0.001. * denotes p<0.05. 95

Table 4-1 : Cardiac function and geometry parameters..... 99

Table 4-2: p-values from Tukey Kramer HSD tests comparing Peak $Strain_{dias}$, peak ΔP_{AVC}, peak ΔP_{OFT}, peak $\Delta P_{AVC}/(HR*\mu)$, Peak $\Delta P_{OFT}/(HR*\mu)$ and EW between each pair of dpfs. n=4-5 at each dpf. *** denotes p<0.0001. ** denotes p<0.001. * denotes p<0.05. 111

LIST OF FIGURES

Figure 1-1: Three schematic tissue configurations with transport pathways that have been numerically modelled. A) single capillary embedded in tissue cylinder B) parallel flow blood capillaries in tissue cylinder C) lymph vessel parallel to blood vessel enclosed in tissue cylinder. d is the capillary diameter, L is the intercapillary separation and D is tissue diameter. The arrows show the main transport mechanisms of a solute in the tissue. The extravascular space contains interstitial fluid flowing through a fibrous matrix. The blood vessel contains an inner core of red blood cells (RBC) surrounded by an outer plasma layer. The lymph vessel contains the interstitial fluid in it. No extravasation occurs in lymph vessels. 21

Figure 1-2: Extravascular concentration-time history of five solutes in a) the SBC configuration b) The 2 BC configuration and c) the BC_LC configuration. Extravascular solute concentration is normalized by the maximum intravascular concentration in the blood capillary volume. Solute concentration in the tissue space decreases with time and varies with solute size. The inset in each subplot is a magnified view to show the concentration variation at earlier times for all three vessel configurations. 23

Figure 1-3: Extravascular concentration-time history of five solutes for a) Co-current (CO) flow in microvessels in 2 BC configuration b) Counterflow (CN) in microvessels in 2 BC configuration c) Co-current (CO) flow in microvessels in BC_LC configuration and d) Counterflow (CN) in microvessels in BC_LC configuration. Extravascular solute concentration is normalized by the maximum intravascular concentration in the blood capillary volume. Counterflow (CN) reduces the solute concentration in tissue space more than co-current flow (CO) in parallel capillary configuration. 24

Figure 1-4: a) Schematic showing the setup and the calculation of % concentration deviation. b) Non-dimensional intercapillary separation (L/d) between 5 and 25 shows significant deviation of solute concentration in 2 BC and BC_LC configurations compared to SBC configuration for 3 kDa and 10 kDa solute sizes. The dotted lines represent L/d values of 5 (yellow) and 21.5 (purple) which are the lower and upper limits of normalized intercapillary separation in breast tumors. L/d values above 21.5 are typically found in normal (non-diseased) tissues. 25

Figure 1-5: a) Non-dimensional concentration time history (T* vs C*) for all solute sizes in all tissue configurations with varying intercapillary separation b) A magnified view of the non-dimensional concentration time history to identify time occurrences of peak concentrations (C*) c) The peak concentration (C*) values are plotted separately to find an average non-dimensional time of occurrence as 0.027 ($\boldsymbol{Tpeak}*$)$\pm$0.018 ($\boldsymbol{\sigma std}$). 27

Figure 1-6: Comparison of experimental and numerical normalized concentration-time histories for 3kDa and 70 kDa solutes in a single capillary cancer tissue. 32

Figure 1-7: Schematic tissue configuration showing the three regions in a tissue modeled by the mixture theory equations: the intravascular space (the blood vessel and the lymph vessel), the capillary wall and the extravascular space. The stromal cells are shown to indicate the non-homogeneity in the extravascular space that the mixture theory can account for. 38

Figure 1-8: Concentration vs Time profile of five solutes at the blood vessel inlet. 41

Figure 1-9: 3D vascularized *in vitro* microfluidic platform for experimental validation. a) CAD drawing of the platform. b) Confocal image of blood vessel with endothelial cells (red) surrounded by breast carcinoma cells (green). 43

Figure 2-1: On the top left a heartbeat from a CMM scan is selected and two spatially varying signals corresponding to times t1 and t2 are extracted from it on top right. The CWT transform for each time signal (on bottom left) provides the power spectra shown in the bottom middle figure, from which the dominant wavenumber is determined. The bottom right figure shows a schematic of a representative spatial variation of power for each time signal at its dominant wavenumber. The spatial lag, $\Delta \boldsymbol{x}$, shown in the figure, the known time difference, $\Delta \boldsymbol{t}$, and the dominant wavenumber, $\boldsymbol{Kdom}$ combine to give the peak propagation velocity, $\boldsymbol{VW, k}$..... 51

Figure 2-2: Representative wavelet analysis. The first column shows the CMM echocardiogram for a normal filling representative patient with t1 and t2 indicated by the vertical blue lines. The next two columns show the CWT power spectra at t1 and at t2. The yellow lines show the motion of the peaks at different wavenumbers. The CWT is applied to each temporal velocity signal on the CMM echocardiogram resulting in a CWT power spectrum localized in space, time and wavenumber. The spatial lag of the peak on the CWT power spectra is calculated between two time steps, for each wavenumber (horizontal location). The spatial lag and the time between the two time signals are used to calculate a propagation velocity for each wavenumber. As evident from the CWT images, higher wavenumbers have higher displacements than lower wave numbers. The range of dominant wavenumbers is specific to each patient. The minimum wave number considered is the inverse of the physical length of the LV. The maximum wavenumber is also specific to each patient and is dependent on the most energetic wave components in each signal. 52

Figure 2-3: Color-M-Mode based parameters for each patient cohort for group A. The black star at the circle center denotes the median value of each parameter in each cohort. The radius of the circle denotes the deviation in each parameter. Color of the deviation circles denotes methodology and corresponds to axis colors. 54

Figure 2-4: Receiver Operator Characteristic (ROC) curves for three conventional parameters and for the proposed wavelet parameter of Group A. The area under the curve (AUC) is noted in the legend for each parameter. The plot differentiates the normal filling cases from diseased filling ones. The maximum wave component peak-VW displays the highest AUC. 56

Figure 2-5: CMM based parameters for each patient cohort in group B. The black star at the circle center denotes the median value of each parameter in each cohort. The radius of the circle denotes the deviation in each parameter. Color of the deviation circles denotes methodology and corresponds to axis colors. 57

Figure 2-6: Operator Characteristic (ROC) curves for all methods of the Group B. The area under the curve (AUC) is noted in the legend for each parameter. (a) The classification is based on normal ventricle geometry versus remodeled ones. (b) The classification is based on LVH ventricle geometry versus DCM ones for the plot on right. 58

Figure 2-7: Variation of peak-VW (labelled as peak VP for this demonstration) with changing time step size shown for 3 sample patients in each of the Normal, Restrictive, LVH and DCM cohorts. 60

Figure 3-1: Variation of mean a) heart rate (HR), b) Reynolds number (Re) and c) Womersley number (Wo) at atrial inflow, d) end-diastolic ventricle area (A), e) ventricle ejection fraction (EF) and f) fractional ventricle diastolic time (t_{diast}/T) with medaka age progression (dpf). The black vertical line between 8 dpf and 9 dpf denotes hatching. Error bars ± SD. n=5 for each parameter at each dpf. Parameters were compared to 3 dpf values. *** denotes $p < 0.0001$; ** denotes $p < 0.001$; * denotes $p < 0.05$. 69

Figure 3-2: Variation of mean a) peak shear rate (γ), b) hematocrit (Ht) and c) blood dynamic viscosity (μ) in ventricle with medaka age progression (dpf). The black vertical line between 8 dpf and 9 dpf denotes hatching. n=5 for each parameter at each dpf. Error bars denote ± SD. Parameters were compared to 3 dpf values. * denotes $p < 0.05$. 70

Figure 3-3 : Spatial Variation of phase averaged streamwise velocity in AVC and OFT of the medaka heart at three different times and at 3 dpf, 6 dpf, 9 dpf and 12 dpf. The profiles at each dpf are extracted at times t1, t2 and t3. The times occur during peak ventricle diastole for the top plots while it occurs during peak ventricle systole for the bottom plots. The time interval at 3 dpf and 6 dpf is 25 ms and at 9 dpf and 12 dpf is 20 ms. 71

Figure 3-4: Time variation of velocity profiles in the a) atrioventricular canal (AVC) and b) ventricle outflow tract (OFT). Black lines denote the median profiles while the pink shade denotes the region between maximum and minimum profiles. The peak values of the median profile are marked on each plot by a blue circle and the minimum values on the median profile are marked by a blue star. n=5 for each dpf. 72

Figure 3-5: Time variation of WSS profiles in the a) atrioventricular canal (AVC) and b) ventricle outflow tract (OFT). Black lines denote the median profiles while the pink shade denotes region between maximum and minimum profiles. The peak values of the median profile are marked on each plot by a blue circle and the minimum values on the median profile are marked by a blue star. n=5 for each dpf. 74

Figure 3-6: Variation of tail vessel cross-sectional area (μm2) with fish age progression (dpf). a) Caudal vein and caudal artery variation are captured from 3 dpf to 8 dpf. b) Dorsal artery (DA), caudal artery (CA), caudal vein (CV), and dorsal vein (DV) area variation is captured from 9 dpf to 14 dpf. n=5 for each dpf. 75

Figure 3-7: Time variation of a) velocity and b) WSS profiles in the tail vessels. Red lines denote arterial profiles while the blue lines denote venous profiles. Dotted curves correspond to dorsal vessels and solid curves correspond to caudal vessels. From 9 dpf to 14 dpf the red '+' markers correspond to the peak magnitude in dorsal artery while the red 'o' markers correspond to the peak magnitude in caudal artery. n=5 for each dpf. 76

Figure 3-8: Correlation of relative gene expressions and peak WSS variation in heart and tail vessels with fish age progression (dpf). The * in the middle and bottom plots denote statistical significance compared to the control values in 3 dpf. In the bottom plot, the diamond denotes statistical significance compared to control values in 9 dpf for Dorsal Aorta (DA) and the + denotes statistical significance compared to control values in 9 dpf for Caudal Aorta (CA). $p<0.05$ was considered statistically significant. 78

Figure 3-9: Location of heart and vessels in medaka and schematic diagram of medaka heart at different ages. (a) Location of heart, dorsal vessels and caudal vessels when viewed from the side

in a larval medaka (age 14 dpf). Location of AVC and OFT in a schematic medaka heart during (b) 3 dpf to 5 dpf, (c) 6 dpf to 8 dpf and (d) 9 dpf to 14 dpf. “A” represents atrium and “V” represents ventricle. Red rectangle represents location of measurement at AVC and green rectangle represents location of measurement at OFT. 85

Figure 3-10: Edge detection of the endocardial wall based on intensity gradients. a) Signal amplified image of flow through OFT b) Velocity vectors at the OFT walls with the color displaying high positive and negative intensity gradients c) Endocardial wall positions (circles colored by WSS magnitude) detected by edge detection of high intensity gradients. Images were taken from a 14 dpf medaka heart. V represents ventricle and BA stands for bulbus arteriosus. 86

Figure 3-11: Raw images to velocity vector fields. a) raw image b) signal amplified image and c) velocity vectors superimposed on raw image of a 13 dpf medaka heart during ventricle diastole. AVC = Atrioventricular canal; OFT = ventricle outflow tract. d) raw image e) signal amplified image and f) velocity vectors superimposed on raw image of caudal vein and caudal artery. Red vectors denote higher velocity than green vectors. 87

Figure 4-1: Pressure field across ventricle, atrium and AVC during ventricle diastole at 3 dpf, 8dpf and 13 dpf. 100

Figure 4-2: Pressure field across ventricle, VB and OFT during ventricle diastole at 3 dpf, 8dpf and 13 dpf. 101

Figure 4-3: Time variation profiles in the atrioventricular canal (AVC) for the flow parameters a) Velocity Magnitude (Vm_{AVC}) b) Pressure drop (ΔP_{AVC}) and c) Non-dimensionalized pressure drop $\Delta \boldsymbol{PAVCHR} * \boldsymbol{\mu}$. Black lines denote the median profiles while the pink shade denotes region between maximum and minimum profiles. The peak values of the median profile are marked on each plot by a blue circle. n=3-5 for each dpf..... 102

Figure 4-4: Time variation profiles in the atrioventricular canal (OFT) for the flow parameters a) Velocity Magnitude (Vm_{OFT}) b) Pressure drop (ΔP_{OFT}) and c) Non-dimensionalized pressure drop $\Delta \boldsymbol{POFTHR} * \boldsymbol{\mu}$. Black lines denote the median profiles while the pink shade denotes region between maximum and minimum profiles. The peak values of the median profile are marked on each plot by a blue circle. n=3-5 for each dpf..... 103

Figure 4-5: Strain measurement of the ventricle wall along a heart cycle. a) Pericardial and endocardial strain overlapped with velocity vectors on raw image of a 13 dpf medaka heart at peak diastole. V stands for ventricle. b)Variation of strain time history across medaka age progression. 104

Figure 4-6: Pressure drop (ΔP_{AVC}) vs endocardial wall strain plots from 3 dpf to 14 dpf. Three curves in each dpf denote minimum EW (black curve), median EW (blue curve) and maximum EW (red curve). The y-axis limits for subplots in each column is same. The x-axis limits for all subplots are same. 105

Figure 4-7: Variation of a) Peak EW, b) peak ΔP at AVC and OFT and c) peak diastolic ventricle strain with medaka age progression. The * in the plots denote statistical significance compared to the control values in 3 dpf. *** denote $p<0.0001$, ** denote $p<0.001$, and * denote $p < 0.05$. . 106

ABSTRACT

Cancer and cardiac diseases are the major causes of morbidity and mortality in the western world. Cardiovascular hemodynamics is increasingly being used to understand the pathophysiological progression of these diseases. Advancements in imaging modalities and development of multiscale numerical models have opened avenues for innovative quantification of flow metrics that may potentially aid in clinical diagnosis. The motivation behind this dissertation is to investigate three different physiological flow phenomena and develop new flow specific parameters as explained in the following paragraphs.

Drug transport efficacy in treating breast tumors has a strong correlation with tissue architecture, nanoparticle transport parameters and hemodynamic metrics that varies from one patient to another. The exact time interval between nanoparticle introduction and drug release must be accurately determined to achieve therapeutic efficacy. The first chapter of the current work implements a numerical model based on mixture theory equations to investigate effect of varying inter-capillary separation on solute transport in dual-channel tissues for various solute sizes (0.5-15 nm) and molecular weights (0.1-70 kDa). The predictive capability of the numerical model is validated by measurements of dextran transport in an invitro tumor platform containing multiple blood vessels. The main contribution of this work is in reporting a unique non-dimensional time at which solute concentration peaks in any location in the tissue in absence of pharmacokinetics.

The second chapter focuses on the development of a physics-based metric from color-m-mode (CMM) echocardiography scans to correctly diagnose different stages of left ventricle diastolic dysfunction (LVDD). Current practice of diagnosing LVDD involves calculating a combination of parameters like intraventricular pressure difference (IVPD) and propagation velocity (Vp) from the CMM scans. The conventional Vp measurement is based on heuristics. This definition does not utilize the entire information from the spatio-temporal velocity distribution of the ventricle filling cycle. The present work challenges the underlying assumption of the early ventricle filling wave moving with a constant velocity. The proposed method in this chapter uses wavelets to analyze the early diastolic ventricle filling wave and introduces a wavelet based peak propagation velocity (Peak-Vw). Peak-Vw is free of the inherent assumptions of the subjective selection of an iso-contour in the scan and measuring a slope from it. The novelty of the

Peak-Vw measurement can provide new insights for understanding the complicated pathophysiology of the left ventricle (LV) diastolic function.

The final focus of this dissertation is to investigate the evolving hemodynamics of the cardiovascular system of Japanese medaka while it is growing from embryonic state to larval stages. Cross-correlation of red blood cell patterns from 2D micro-particle image velocimetry (μPIV) images provide measurements of velocity fields in the fish heart and vessels. Accurate velocity gradient measurements are required to further derive flow quantities like wall shear stress (WSS), pressure drop across valves and cardiac strain.

WSS experienced by endocardial cells and vascular endothelial cells are linked to changes in cardiac specific gene expressions. Previous studies with other vertebrate models investigating mechano-genetic correlations were focused on mutating genes or introducing some perturbation in the blood circulation. In the third chapter of this dissertation, a baseline longitudinal study tracking the change in cardiovascular WSS and gene expressions with natural progression of fish age is presented for the first time. Peak WSS changes with fish age calculated at the valves located at the ventricle inflow (AVC) and outflow (OFT), at the caudal artery (CA) showed an inflection trend that coincides with developmental landmarks of cardiac morphogenesis. Retrograde flow in the medaka heart valve locations have been documented for the first time. Contrary to intuition, the caudal and dorsal vessels in the fish tail displayed a reduction in cross-sectional area with age progression. Identification of these unique trends in the mechano-genetic tapestry of vertebrates prepares the ground for future studies that can test the mechano-transduction mechanisms.

The fourth chapter delves deeper into the flow induced pressure drop (ΔP) across the AVC and OFT of the ventricle and the peak strain experienced by the ventricle wall remodeling through fish age progression. Valve regions record the dynamic variations of ΔP that may induce WSS fluctuations with age progression. A variation of cardiac strain with age is the key driver of varying chamber morphology. This is the first study in teleost species literature that analyzes the endocardial work (EW) calculated from a ΔP-strain loop. The increase in EW observed across fish age progression can be directly related to the heart's metabolic demand. EW can be used in future studies of human hearts to distinguish between healthy and diseased ventricles.

Overall, this dissertation provides an in-depth study of three separate biophysical processes of the vertebrate cardiovascular system and designs new metrics that have translational clinical potential.

1. MIXTURE THEORY MODELING FOR CHARACTERIZING SOLUTE TRANSPORT IN BREAST TUMOR TISSUES

Sreyashi Chakraborty[1], Alican Ozkan[2], Marissa Nichole Rylander,[2,3,4] Wendy A. Woodward[5], and Pavlos Vlachos[1]

[1] Department of Mechanical Engineering, Purdue University, West Lafayette, IN 47907

[2] Department of Mechanical Engineering, The University of Texas at Austin, Austin, Texas 78712

[3] Department of Biomedical Engineering, The University of Texas at Austin, Austin, Texas 78712

[4] The Institute for Computational Engineering and Sciences, The University of Texas at Austin, Austin, Texas 78712

[5] Department of Radiation Oncology, MD Anderson Cancer Center, Houston, TX 77030

This chapter has been previously published in Journal of Biological Engineering **13,** 46(2019)

DOI: https://doi.org/10.1186/s13036-019-0178-z

1.1 Abstract

Background

Tumor numerical models have been used to quantify solute transport with a single capillary embedded in an infinite tumor expanse, but measurements from different mammalian tumors suggest that a tissue containing a single capillary with an infinite intercapillary distance assumption is not physiological. The present study aims to investigate the limits of the intercapillary distance within which nanoparticle transport resembles solute extravasation in a breast tumor model as a function of the solute size, the intercapillary separation, and the flow direction in microvessels.

Methods

Solute transport is modeled in a breast tumor for different vascular configurations using mixture theory. A comparison of a single capillary configuration (SBC) with two parallel cylindrical blood vessels (2 BC) and a lymph vessel parallel to a blood vessel (BC_LC) embedded in the tissue cylinder is performed for five solute molecular weights between 0.1 kDa and 70 kDa. The effects

of counter flow (CN) versus co-current flow (CO) on the solute accumulation were also investigated and the scaling of solute accumulation-decay time and concentration was explored.

Results

We found that the presence of a second capillary reduces the extravascular concentration compared to a single capillary and this reduction is enhanced by the presence of a lymph vessel. Varying the intercapillary distance with respect to vessel diameter shows a deviation of 10-30 % concentration for 2 BC and 45-60% concentration for BC_LC configuration compared to the reference SBC configuration. Finally, we introduce a non-dimensional time scale that captures the concentration as a function of the transport and geometric parameters. We find that the peak solute concentration in the tissue space occurs at a non-dimensional time, $T^*_{peak} = 0.027 \pm 0.018$, irrespective of the solute size, tissue architecture, and microvessel flow direction.

Conclusions

This work suggests that the knowledge of such a unique non-dimensional time would allow estimation of the time window at which solute concentration in tissue peaks. Hence this can aid in the design of future therapeutic efficacy studies as an example for triggering drug release or laser excitation in the case of photothermal therapies.

Keywords – Solute transport, breast tumor, mixture theory modeling

1.2 Background

The total cost of cancer care in the United States is projected to increase by 39% from 2010 to 2020 (1). Primary areas of cancer research involve improving the efficacy of chemotherapeutic agents at the tumor sites and minimizing their toxic side effects in the non-target sites (2-4). Conventional chemotherapeutic agents (5) are non-specifically distributed in the body which limits the effectiveness of the drug dose and increases toxicity in normal cells. Drug carriers with hydrodynamic diameter 3-200 nm accumulate preferentially in tumors owing to the enhanced permeability and retention (EPR) effect (6) exploiting the wider pores in tumor vessels and the impaired lymphatic drainage in diseased tissues. The transport mechanism of these nanoparticles in tumors is a function of the hemodynamics, nanoparticle transport parameters (solute

permeability, solute diffusivity, reflection coefficient) as well as the extravascular matrix properties (porosity, hydraulic conductivity). Before the binding/uptake by the cancer cell these particles overcome three major transport barriers: transport through microvasculature, translocation across the endothelial wall, and diffusion within the extracellular tissue matrix. Using a numerical model to investigate the nanoparticle transport mechanics could enable determination of the exact time interval between nanoparticle introduction and drug release to achieve desired therapeutic efficacy based on patient specific tumor measurements.

The majority of the existing multiscale models use the Darcy's law, Starling's law, and Poiseuille's law to analyze extravascular, trans-capillary, and intravascular transport respectively (7-12). Poiseuille's law cannot account for variations in capillary diameter and the inhomogeneous nature of blood. Deviations from Starling's law are expected when osmotic terms would include other endogenous solutes in addition to proteins. Darcy's law does not include the dependence of interstitial flow on local fluid chemical potential. Schuff et al. (13, 14) used mixture theory equations in an axisymmetric tissue geometry containing a concentric blood vessel and showed the dependence of extravascular fluid transport on chemical gradients in addition to hydrostatic pressure which was previously suggested (15, 16) and observed (17) but not commonly accounted for in previous transport models. **Recently developed tumor numerical models (11, 18, 19) focus on complex capillary distribution in the tissue, multi-stage drug delivery systems and dynamically changing tumor geometry but for the nutrient transport they rely on the advection-diffusion equation only instead of considering each type of particle (solute, fluid, cells etc) as a mixture component**. In the present work, we focus on nanoparticle transport only, neglecting, drug pharmacokinetics, dynamic tumor geometry variation and complex capillary network to delineate a characteristic metric applicable to all kinds of solute and fluid transport in tumors. The mixture theory model is implemented in dual-tissue geometries to predict nanoparticle distribution in cancerous breast tissues over a wide range of particle sizes (0.5-15 nm) and molecular weights (0.1-70 kDa).

We hypothesize that nanoparticle distribution in breast tumors is a function of solute size, intercapillary separation, and flow direction and there exists a characteristic non-dimensional time, T^*_{peak}, for which solute concentration in the tissue space is maximum. We test this hypothesis by investigating the transport mechanisms of five solute types (0.1, 3, 10, 40 and 70 kDa) in tumor systems containing a single vessel (SBC) and compare with tumors possessing dual-vessel (blood

capillaries only (2 BC), blood capillary and a lymph capillary (BC_LC)) tissue systems with varying intercapillary separation. The mixture theory equations are used for the first time and their predictive capability validated with measurements of dextran transport in an *in vitro* tumor platform containing multiple blood vessels.

1.3 Results

Numerical simulations with baseline values of breast tumor transport (**Table 1-1**) show a strong influence of vascular configurations on the solute accumulation-decay temporal history in the tissue space. A schematic of the vascularized breast tumor configuration along with the transport pathways is shown in **Figure 1-1**. The blood vessel in **Figure 1-1** allows both intravasation and extravasation depicted by blue and red arrows respectively. The lymph vessel allows intravasation (blue arrow) only and drains the lymphatic fluid out of the tissue. All the equations used in the simulations are explained in the **Appendix A.**

Table 1-1: Input parameters for mixture theory model. Values are for different types of cancer tissues adopted from the literature. References are listed in the last column of table.

Solute Dependent Parameters						
Solute Molecular Weight (kDa), MW	0.1	3.0	10.0	40.0	70.0	
Hydrodynamic Diameter (nm)	0.69	1.6	5.46	13.2	14.4	(20-22)
Reflection coefficient, σ	0.00025	0.00025	0.02500	0.08600	0.14000	(13, 14, 23, 24)
Solute Permeability coefficient, P_d ($x10^{-8}$ m/s)	800	174	70	33	30	(13, 14, 25-27)
Diffusion Coefficient ($x10^{-11}$ m^2/s), D_f	89.6	17.0	9.6	7.8	3.6	(28-31)
Retardation factor, R_F	1.10	1.10	1.07	0.94	0.84	(29-33)
Initial solute concentration (mol/m^3), Co	6.11	0.20	0.08	0.02	0.01	(28)
Flow Parameters						
Pressure gradient along blood vessel (Pa), dP			2394			(34-37)
Hydrostatic pressure in arteriole (Pa), Par			4394			(34-37)
Boundary tissue pressure (Pa), Po			2700			(38-41)
Osmotic Pressure gradient (Pa)			2500			(13, 14, 20, 34)

Table 1-1 continued

Hydraulic conductivity (x10^{-15}) (m^2/Pa-s)	**400**	**(13, 14, 39, 42)**
Hydraulic permeability (x10^{-10}) (m/Pa-s)	10	(13, 14, 39)
Tissue porosity, ∅	0.4	(39, 43-45)
Geometrical Parameters		
Length of microvessels (mm), l	1	(46, 47)
Diameter of microvessels (μm), d	10	(46, 48, 49)
Diameter of tissue (μm), D	200	(46, 48, 50-52)

1.3.1 Test 1: Effect of solute size in three configurations for fixed intercapillary separation

The effect of solute size in the double blood capillary (2 BC) and the blood capillary-lymph vessel (BC_LC) configurations compared to the single capillary (SBC) is shown in **Figure 1-2**. The tissue volume surrounding each capillary is equal. The concentration-time history essentially shows an initial accumulation period until the solute reaches its maximum concentration in the tissue space,

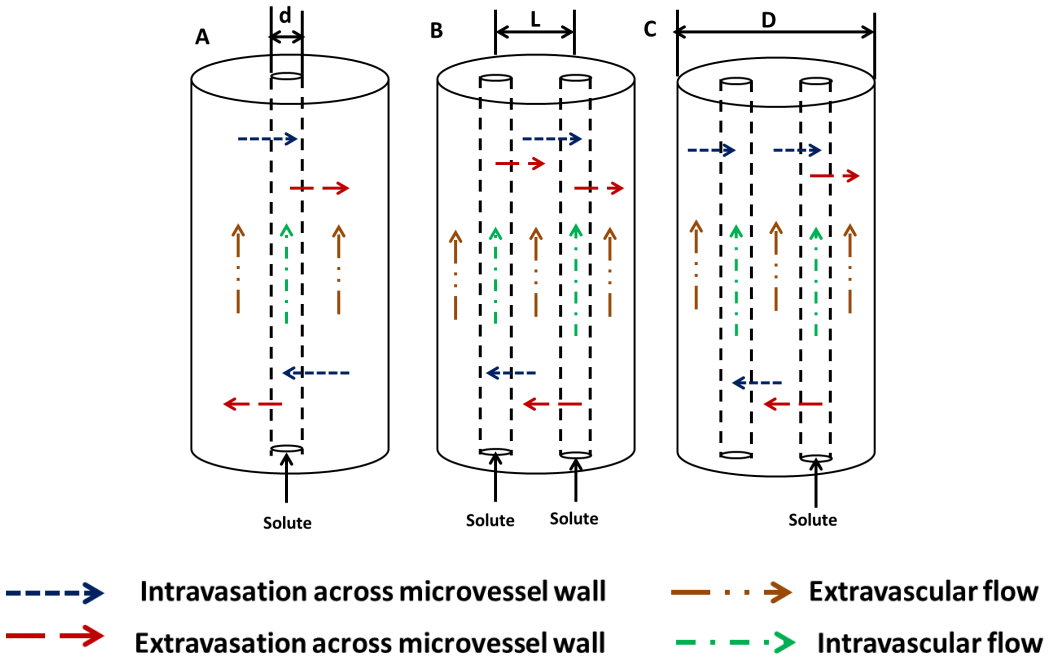

Figure 1-1: Three schematic tissue configurations with transport pathways that have been numerically modelled. A) single capillary embedded in tissue cylinder B) parallel flow blood capillaries in tissue cylinder C) lymph vessel parallel to blood vessel enclosed in tissue cylinder. d is the capillary diameter, L is the intercapillary separation and D is tissue diameter. The arrows show the main transport mechanisms of a solute in the tissue. The extravascular space contains interstitial fluid flowing through a fibrous matrix. The blood vessel contains an inner core of red blood cells (RBC) surrounded by an outer plasma layer. The lymph vessel contains the interstitial fluid in it. No extravasation occurs in lymph vessels.

then it is followed by a concentration decay. It is observed in the accumulation phase of the SBC configuration (**Figure 1-2a** inset) the 0.1 kDa, 3 kDa and 10 kDa solutes attain peak concentration with 41.3%, 40.3% and 30.7% of their maximum intravascular concentrations at 2.4, 4.2, and 7.2 minutes respectively whereas heavier solutes like 40 kDa and 70 kDa attain 26.9% and 30.5% of their maximum intravascular concentrations at 13.2 and 21 minutes respectively. The time taken for 0.1 kDa, 3 kDa and 10 kDa solutes to reduce to 10% of their maximum intravascular concentrations are 25.8, 28.2 and 37.2 minutes respectively whereas the same for the 40kDa and 70kDa solutes are 1.57 and 3.25 hours respectively. The peak tissue concentration for 0.1 kDa, 3 kDa, 10 kDa, 40 kDa and 70 kDa solutes decreases by 25%, 28%, 31%, 28% and 25% respectively in the 2 BC configuration (**Figure 1-2b** inset) and by 55%, 52%, 50%, 53% and 40% respectively in the BC_LC configuration **(Figure 1-2c** inset) with respect to the SBC configuration. In comparison to the SBC tissue peak concentration, the peak occurs at later times (**Figure 1-2b**) in 2 BC configurations (3 kDa: 6.6 min vs 4.2 min; 10 kDa: 9.6 min vs 7.2 min; 40 kDa: 21 min vs 13.2 min) and at earlier times (**Figure 1-2c**) in BC_LC configurations (3 kDa: 3 min vs 4.2 min; 10 kDa: 4.2 min vs 7.2 min; 40 kDa: 9.6 min vs 13.2 min). For the smallest solute 0.1 kDa, the concentration attains peak value later compared to its SBC counterpart (2.4 mins) in both the 2 BC (4.2 mins) and BC_LC (3 mins) tissue spaces. On the contrary the largest 70 kDa solute attains peak concentration earlier in both 2 BC (17 mins) and BC_LC (7.8 mins) extravascular spaces compared to its SBC counterpart (21 mins). The 70 kDa solute, however, exhibits a faster onset of concentration decay both in the 2 BC and BC_LC configuration (SBC: 21 min; 2 BC: 17.4 min; BC_LC: 7.8 min) while a delayed concentration decay is seen for the 0.1 kDa solute (SBC: 2.4 min; 2 BC: 4.2 min; BC_LC: 3 min).

1.3.2 Test 2: Effect of flow direction in microvessels

The microvessel flows considered in **Test 1** are in the same axial direction and are called co-current (CO) flows. They are compared with oppositely directed axial flows in the microvessels which are called counter current (CN) flows. **Figure 1-3** compares the CN flow with the CO flow for 2 BC configuration and BC_LC configuration respectively. In both configurations there is no difference between the two flow types during the solute accumulation phase in the tissue. As the tissue concentration decays, the extravascular solute concentration is less in CN flow at later times compared to CO flow.

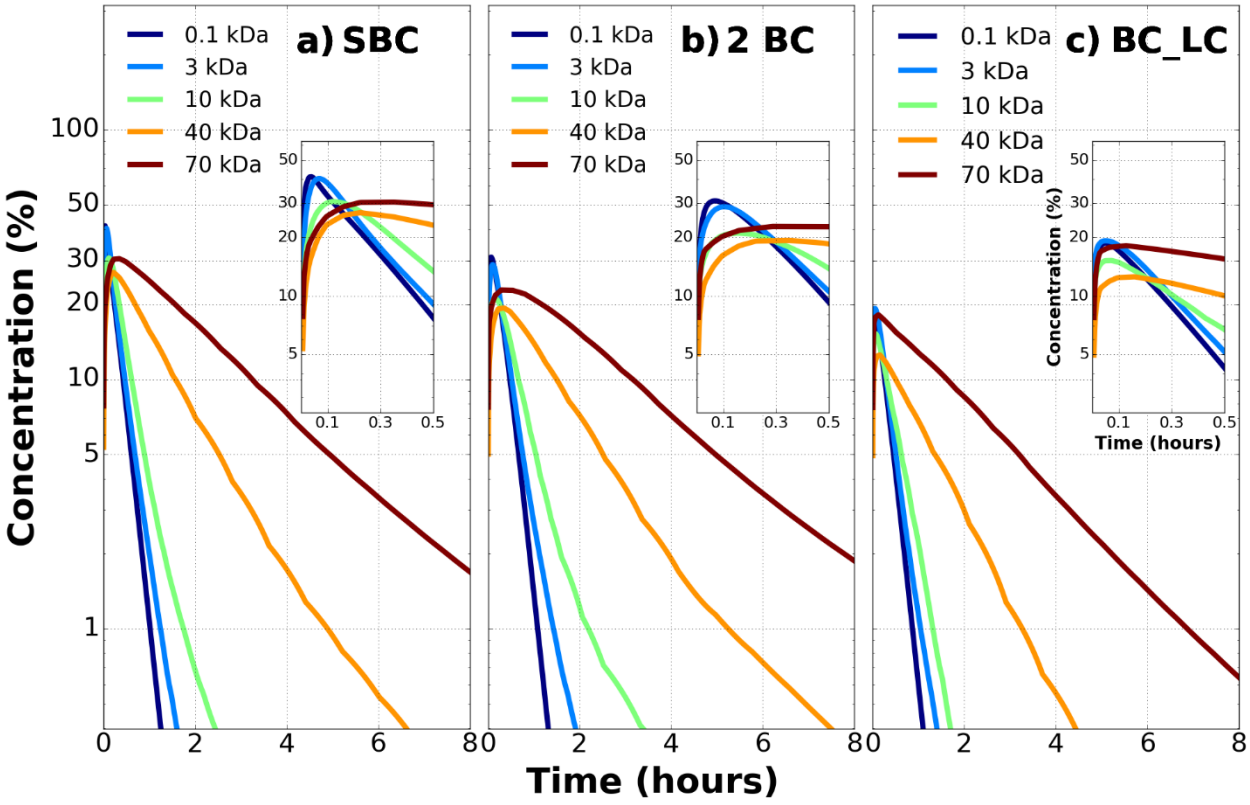

Figure 1-2: Extravascular concentration-time history of five solutes in a) the SBC configuration b) The 2 BC configuration and c) the BC_LC configuration. Extravascular solute concentration is normalized by the maximum intravascular concentration in the blood capillary volume. Solute concentration in the tissue space decreases with time and varies with solute size. The inset in each subplot is a magnified view to show the concentration variation at earlier times for all three vessel configurations.

The percentage reduction in concentration is more pronounced for larger (10 kDa: 0.5%; 40 kDa: 1.7%; 70 kDa: 2.5%) solutes in 2 BC configuration (**Figure 1-3a**, **Figure 1-3b**). A similar observation is made for heavier (10 kDa: 0.12%; 40 kDa: 0.4%; 70 kDa: 0.5%) solutes but the difference is less in BC_LC configuration (**Figure 1-3c**, **Figure 1-3d**) compared to the 2 BC configuration. The faster drainage in presence of additional capillaries delays the solute accumulation. Thus, it takes a longer time for the solute to reach its peak concentration in a tissue location and compared to SBC configuration the magnitude of the peak accumulation is lower.

1.3.3 Test 3: Effect of intercapillary separation on transport of 3 kDa and 10 kDa solutes

The intercapillary separation (L) was varied with respect to the vessel diameter (d) in the next set of tests for the 2 BC and BC_LC configurations. We calculated the surface averaged extravascular

concentration at a radial distance 0.2L from the blood vessel wall in SBC configuration (C_{SBC}) as well as in the 2 BC configuration (C_{2BC}) where L is the intercapillary separation (**Figure 1-4a**).

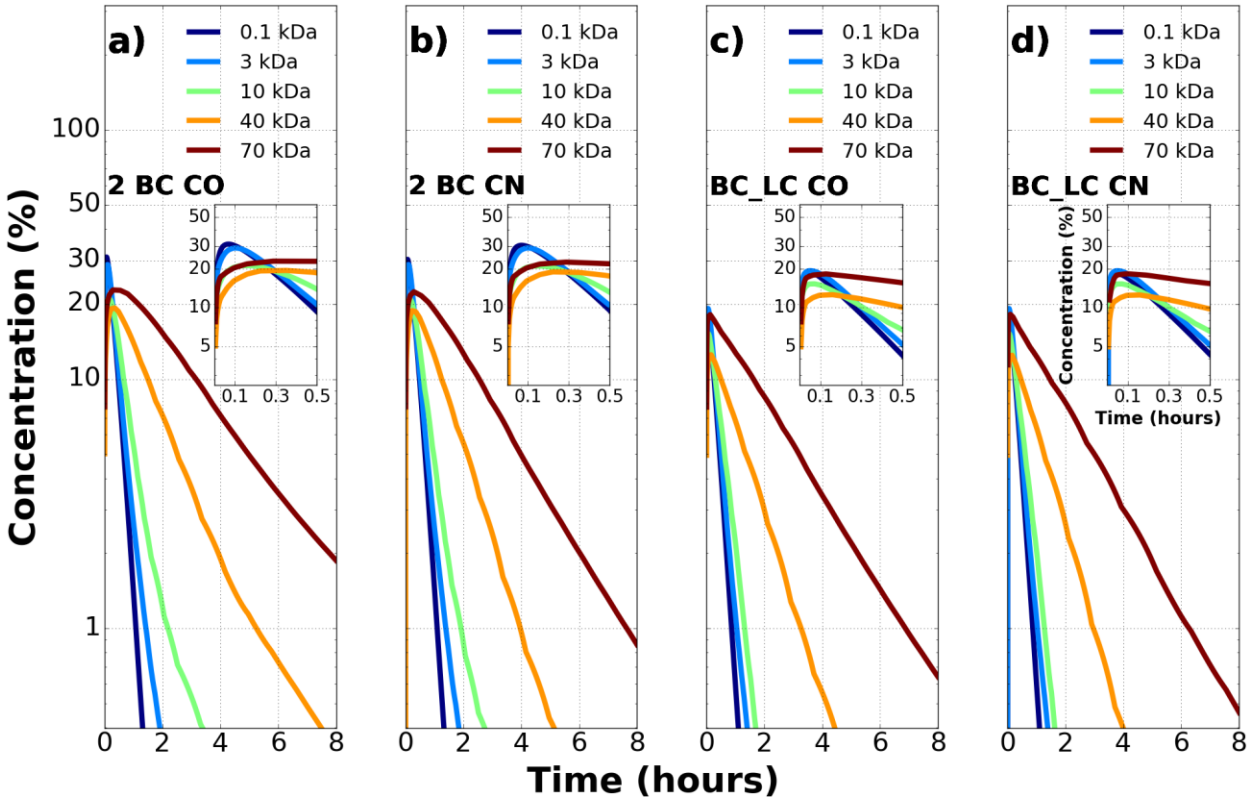

Figure 1-3: Extravascular concentration-time history of five solutes for a) Co-current (CO) flow in microvessels in 2 BC configuration b) Counterflow (CN) in microvessels in 2 BC configuration c) Co-current (CO) flow in microvessels in BC_LC configuration and d) Counterflow (CN) in microvessels in BC_LC configuration. Extravascular solute concentration is normalized by the maximum intravascular concentration in the blood capillary volume. Counterflow (CN) reduces the solute concentration in tissue space more than co-current flow (CO) in parallel capillary configuration.

The percentage deviation between these two terms is plotted in **Figure 1-4b** across different values of non-dimensional intercapillary separation (L/d=1, 5, 10, 25, 125) for 3 kDa and 10 kDa solute. The dotted lines represent L/d values of 5 (yellow) and 21.5 (purple) which are the lower and upper limits of normalized intercapillary separation in breast tumors. L/d values above 21.5 are typically found in normal (non-diseased) tissues.

Double Blood Capillary (2 BC) embedded in tissue cylinder

The 2 BC configuration shows minimum deviation (3 kDa: 1.5%; 10 kDa: 2.5%) from the SBC configuration for L/d=1 (**Figure 1-4b**). This is because the spacing between two blood capillary walls is so small that they effectively function as a single capillary with twice the original capillary diameter. So, the solute accumulation almost the resembles that in SBC configuration. The solute concentration deviation is substantial (9-33 %) for L/d=5-25 which is the range of interest as reported in **Table 1-2**. The isolated capillary assumption will not hold true for extravascular solute accumulation in this regime. The deviation (3 kDa: 4.7%; 10 kDa: 8.5%) reduces for L/d=125 because the large spacing between capillary walls minimizes the cumulative effect of the two blood vessels on the peak tissue concentration.

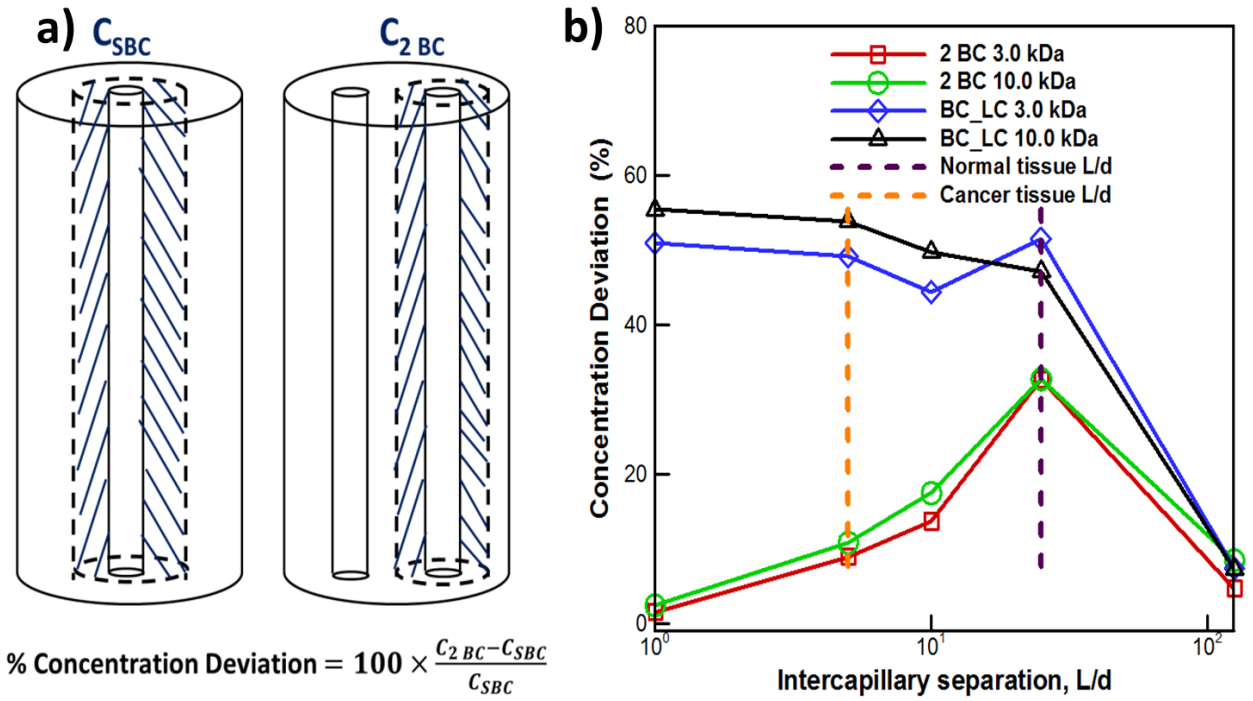

Figure 1-4: a) Schematic showing the setup and the calculation of % concentration deviation. b) Non-dimensional intercapillary separation (L/d) between 5 and 25 shows significant deviation of solute concentration in 2 BC and BC_LC configurations compared to SBC configuration for 3 kDa and 10 kDa solute sizes. The dotted lines represent L/d values of 5 (yellow) and 21.5 (purple) which are the lower and upper limits of normalized intercapillary separation in breast tumors. L/d values above 21.5 are typically found in normal (non-diseased) tissues.

Blood Capillary and Lymph Capillary (BC_LC) embedded in tissue cylinder

The BC_LC configuration (**Figure 1-4b**) shows minimum deviation (3 kDa: 7.4%; 10 kDa: 7.3%) from the SBC configuration for L/d=125 due to the same reason as the 2 BC configuration. But with decreasing L/d the sink action of the lymph vessel become increasingly dominant resulting in 44%-55% deviation of the maximum solute concentration in tissue volume from that in the corresponding SBC configuration in the L/d regime of 1 to 25.

Non-dimensional Time vs Peak Non-dimensional Concentration Analysis

The results discussed in the previous cases have shown that the variation of solute size, microvessel arrangement, number of microvessels and intercapillary separation all contribute differently to the solute accumulation time vs solute decay time in the tissue space. Hence the non-dimensional extravascular solute concentration (C*) and non-dimensional time (T*) were calculated for all test cases to account for variations of these four parameters. The non-dimensional profiles for fixed L/d=1, 5, 10, 25, 125 were plotted in **Figure 1-5a**. All concentration peaks lie within T*=0.1 shown by the dotted black line. So, in **Figure 1-5b** the scaled concentration time-histories from T*=0 to T*=0.1 were analyzed. The peaks were extracted and plotted in **Figure 1-5c**. The solid line red curves that correspond to the largest intercapillary distance (L/d=125) have T^*_{peak} values which

Table 1-2: Intercapillary distance from invivo tissues with capillary diameter, d=10 μm

Tissue Type	Intercapillary Separation (L, μm)	L/d	References
Rat mammary tumors	50	5	(46)
Rabbit neoplastic tissue	101	10.1	(50)
Mammary carcinoma	80-135	8-13.5	(51),(53),(52),(48)
Normal breast tissue	215	21.5	(53)
Human large intestine	107	10.7	(54)
Human colorectal tumor periphery	54	5.4	(55)
Human colorectal tumor center	177	17.7	(55)

are one order of magnitude less than the average T^*_{peak}. This is because for a large L, the second vessel does not contribute to the solute accumulation in the measurement location which is at a distance 0.2L from the first blood vessel. The concentration gradients across each capillary wall dynamically change the extravascular flux across the wall and for a large L the solute may get trapped within a certain distance of the capillary. The non-dimensional equations do not account for these and hence the deviation of T^*_{peak} for L/d=125. It was concluded that the average non-dimensional time at which the peak concentration occurs in all configurations for all solutes is T^*_{peak}=0.027 $\pm$0.018 (**Figure 1-5c**).

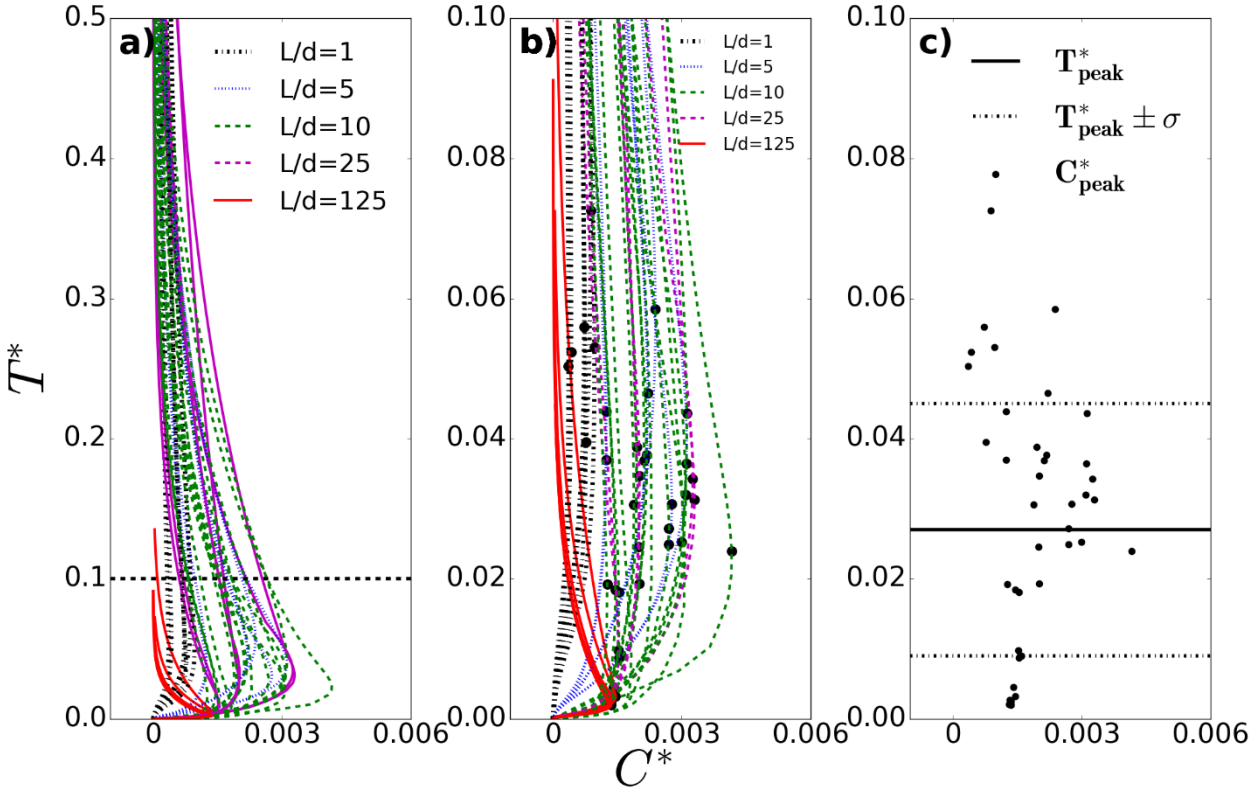

Figure 1-5: a) Non-dimensional concentration time history (T* vs C*) for all solute sizes in all tissue configurations with varying intercapillary separation b) A magnified view of the non-dimensional concentration time history to identify time occurrences of peak concentrations (C*) c) The peak concentration (C*) values are plotted separately to find an average non-dimensional time of occurrence as 0.027 (T^*_{peak})$\pm$0.018 (σ_{std}).

1.4 Discussion

We present a numerical model for breast tumor that can predict passive transport of nanoparticles across a multilayer barrier when the tissue architecture and nanoparticle properties are specified. The solute size (molecular weight and hydrodynamic diameter) influences its extravascular

concentration dynamically across time. Smallest solutes are cleared faster from the tissue but they are also susceptible to getting trapped in the recirculation zone set up by countercurrent blood flow in adjacent vessels (56, 57). High clearance rates measured for solutes <10 kDa during *in vivo* measurements in tumors validate this observation. The therapeutic outcome of breast cancer drugs (Doxorubicin: 0.54 kDa; Cisplatin: 0.3 kDa) having similar molecular weight as the smallest solute investigated here can now be predicted for patient-specific tumor biopsies.

Heavier nanoparticles (50-200 kDa) are preferred vehicles for the tumor location specific targeting and drug delivery (57, 58). According to the results, heavier solutes with hydrodynamic diameter (5-14 nm) take longer to attain maximum accumulation at a specific tissue location and are also removed slowly (59, 60). Presence of adjacent blood vessels with counter-current flow accelerate the clearance process owing to drainage from both ends of the tissue. Presence of a lymph vessel reduces the magnitude of their peak concentration considerably owing to high permeability cross the lymph capillary wall. In various *in vitro*/*in vivo* studies the lymph wall is shown to allow unidirectional flow only (61-64) that facilitates better drainage. Easy removal of all sizes of drugs through the lymphatic system contributes to role of lymphatics in worse response(65).

Blood vessels have been mostly modelled as non-porous structures permeable to solutes embedded in the flow (66, 67). To our knowledge, this is the first numerical model that account for endothelial porosity directly measured from dextran transport in an *in vitro* breast tumor model. Additionally, this work shows inclusion of multiple vessels in a tumor numerical model is necessary to accurately measure transport phenomena. The SBC assumption works only for tissues where capillaries are so close (L/d=1) that they act as a single vessel, e.g when nearby lymph vessels collapse (61, 62, 64, 65) during metastasis of some cancers or if they are so far apart (L/d=125) that the solute flux from one does not reach the other.

The dextran transport investigated using a fabricated 3D microfluidic platform measured tissue porosity, endothelial porosity, nanoparticle permeability and nanoparticle diffusivity. Simulations driven by these parameters showed a close correspondence of numerical and experimental concentration-time histories. These parameters, when reported in literature, span over several orders of magnitude. The wide range can be attributed to the complex *in vivo* measurements whose intrusive nature would perturb the tissue microenvironment (17, 68). Thus,

the ability to measure these parameters *in vitro* can be used to design future non-invasive transport investigation studies.

Condensing all the effects of tissue architecture, solute and fluid transport properties, we suggest there exists a unique time T^*_{peak} at which nanoparticle concentration in the tissue is maximum. Previous analytical solutions of a convective-dispersive solute transport equation with time-dependent inlet boundary condition (69, 70) have shown the dependence of time constant on the input timescale, convection timescale, decay timescale and the diffusion timescales but did not account for varying intercapillary separation. Later Chapman et al. and other researchers (8, 11, 12, 71) modeled transport in tumors characterized by intercapillary separation but did not account for the dynamic change of hydraulic permeability as a function of concentration gradients which in turn modulates the extravascular solute flux. The presented work, for the first time, analyzes the solute concentration in the tissue in the light of mixture theory equations for varying solute types, two parallel microvessels, differing flow directions in parallel vessels and tissue architecture and proposes a non-dimensional time at which solute concentration is maximum in the tissue.

Since this approach non-dimensionalizes the intercapillary separation (L) with the vessel diameter (d), T^*_{peak} can be predicted for tissues ranging over several scales and also for different disease stages (cancer vs normal). This prediction would aid in efficient endothelial targeting, triggering drug release and laser excitation for photothermal therapies (72-74). The T^*_{peak} estimation can hugely impact the clinical landscape as it would customize treatment based on tumor specificity. Future studies with varying nanoparticle design, changing dosage, presence of magnetic targeting, receptor binding can all be implemented first to the mixture theory model whose predictions would increase the efficacy of the targeted drug delivery in patient specific tumors.

The major limitation associated with the study are as follows: The complex vascular network has been simplified. The tortuosity and diameter variation of the microvessels were neglected. The extracellular matrix was considered stationary and not allowed to deform. A zero flux boundary condition was prescribed at each microvessel outlet which deviates from the physiological condition where a constant solute flux is drained to other organs like the liver from the microvessel outlets.

1.5 Conclusions

The study described in this paper focuses on quantification of solute transport across parallel blood vessels and initial lymph vessels in the light of mixture theory. Transport of nanoparticles to the targeted tumor volume is defined by the transport through microchannels, diffusion across endothelium and transport within the porous matrix, all of which were accounted for in the presented work. The results show that the solute size strongly influences its own rate of removal and rate of accumulation in the tissue. The flow physics in the extravascular space facilitate tissue drainage of nanoparticles depending on the solute size, the intercapillary separation and the microvessel arrangement in the tissue.

A unique non-dimensional time T^*_{peak} was reported for the first time for peak solute accumulation in absence of pharmacokinetics. This is the time at which peak concentration of a nanoparticle occurs at any tissue location. The knowledge of the nanoparticle introduction time, tissue mechanical properties and solute dependent properties will allow, in future, to design *in vitro* tissue models testing various nanoparticle designs and concomitantly, predict for patient specific tumors, the appropriate time of drug release that can substantially improve drug efficacy.

1.6 Methods

1.6.1 Mixture Theory Model Parameters

The mixture theory model requires fifteen input parameters that account for the mechanical properties of the porous matrix, type of the injected solute, and vascular geometry. The governing equations and boundary conditions for the mixture theory model have been derived in (13). A sensitivity analysis of the input parameters, calibration and subsequent validation of the model was carried out by Schuff et al. in (14). The mixture theory equations model the transport (13, 14) of the fluid and solute in three distinct regions of a representative vascularized tumor geometry: a) in the intravascular space which consists of the plasma layer concentric with an inner core of red blood cells, b) across the capillary wall which is thin and semi-permeable and c) the extravascular space that comprises of the interstitial fluids and solutes flowing through a fibrous matrix. A finite element software package COMSOL 4.2 (COMSOL, Burlington, MA) was used to run the simulations. The simulation run time for each solute transport in a specific tissue configuration was 1.5 days.

1.6.2 Experimental Validation of Mixture Theory Model

The accuracy of the computational model was confirmed with experimental measurements performed in a 3D vascularized *in vitro* tumor microenvironment. Essential model parameters such as tissue porosity, vessel porosity, solute permeability, and solute diffusivity were measured using the *in vitro* platform and implemented in the model (**Table 1-3**). The concentration-time histories were obtained from the mixture theory equations using the minimum, maximum, and mean values of the tissue parameters measured from *in vitro* platform. The simulation results were also compared with experimental measurements from dextran transport in the same vascularized *in vitro* platform (**Figure 1-6**). Details explaining the fabrication and measurement of porosity, solute permeability and solute diffusivity from the fabricated platform can be found in the **Appendix B**. To our knowledge, this is the first *in vitro* model that measured different porosity values in the extravascular and intravascular spaces.

1.6.3 Experimental and numerical comparison of concentration-time histories

Numerical simulations for the model validation studies were separately processed with identical tissue properties and boundary conditions as obtained from the experiment. The intensity-time histories were spatially averaged at a radial location of 600 μm. These were normalized by the maximum intensity inside the vessel at that time instant. For each of 3kDa and 70kDa solutes, transport was studied in N=3 tissue samples with identical fabrication parameters. The normalized intensity profile of dextran particles from these experiments corresponds to the normalized concentration from the numerical simulations (**Figure 1-6**). The error bars correspond to the experimental variability observed across 3 samples at each time instant.

Table 1-3: Parameters from the fabricated tissue platform used in equivalent simulation

Parameters from fabricated tissue platform	Mean	Min	Max
Vessel diameter (μm)	715	-	-
Tissue diameter (μm)	3000	-	-
Tissue Porosity	0.53	0.49	0.59
Vascular Porosity	0.4	0.37	0.43
Solute Diffusivity (m^2/s)	3 kDa: 25e-11 70 kDa: 4.3e-11	3 kDa: 20e-11 70 kDa: 3.7e-11	3 kDa: 30e-11 70 kDa: 4.9e-11
Solute Permeability (m/s)	3 kDa: 32e-8 70 kDa: 9e-8	3 kDa: 24e-8 70 kDa: 7e-8	3 kDa: 43e-8 70 kDa: 11e-8
Hydraulic Permeability (m^2)	1e-12	-	-

For 3kDa, the smaller solute, the experimental data till 1 hr matches with the simulation curve from maximum values of input parameters. The deviation of experimental results from mean simulated values decreases with increasing time from 1hr to 2 hrs. The higher deviation of the 3kDa numerical curves from the experimental curve can be attributed to the higher susceptibility of the small solutes (<10 nm) to get trapped in local recirculation zones in a non-homogeneous tissue (56, 64). The experimental data for the 70 kDa solute almost coincide with the mean simulation curve and is closely enveloped by the maximum and minimum simulation curves.

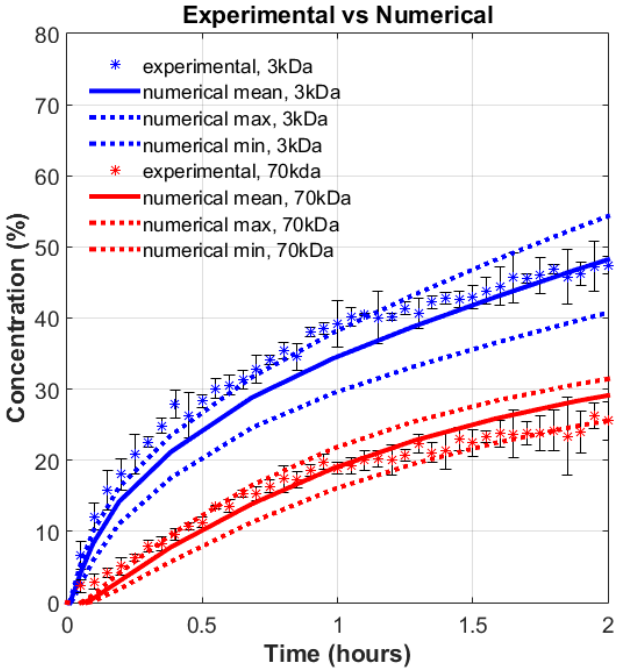

Figure 1-6: Comparison of experimental and numerical normalized concentration-time histories for 3kDa and 70 kDa solutes in a single capillary cancer tissue.

1.6.4 Vascular Tissue Configurations and Test Matrix

In the current study three geometrical configurations of the vessels in the tissue are considered: the single blood capillary (SBC) configuration, the double blood capillary (2 BC) configuration, the blood capillary and the lymph vessel (BC_LC) configuration. The simulations were split into 3 tests listed in **Table 1-4**. The flow direction is same (CO) in parallel microvessels for tests 1 and 3. The intercapillary distance (L) in the dual-microchannel configurations is 100 μm in Test 1 and Test 2 (29, 48, 52).

Test 1: Effect of solute size on transport

Five solutes (0.1 kDa, 3 kDa, 10 kDa, 40 kDa, 70 kDa) are injected at the inlet of the blood capillaries in each configuration to delineate the effect of solute size on transport. The geometry, hydraulic parameters and transport properties of the solute molecules in a breast tumor are in **Table 1-1**. The transport properties of 0.1 kDa solute are estimated from the calibration model developed in (14).

Test 2: Effect of flow direction in capillaries on transport

The second test investigates the influence of co-current flow and counter-current flow in both 2BC and BC_LC tissue configurations and compares the solute transport mechanisms with the SBC configuration.

Table 1-4: Test matrix developed for conducting the study

Configuration	Flow Direction Type	Intercapillary separation (μm)	Solute Molecular weight (kDa)
Test 1 : Effect of solute size			
SBC	N/A	N/A	0.1, 3.0, 10.0, 40.0, 70.0
2 BC	CO	100	0.1, 3.0, 10.0, 40.0, 70.0
BC_LC	CO	100	0.1, 3.0, 10.0, 40.0, 70.0
Test 2 : Effect of flow direction in microvessels			
2 BC	CO	100	0.1, 3.0, 10.0, 40.0, 70.0
2 BC	CN	100	0.1, 3.0, 10.0, 40.0, 70.0
BC_LC	CO	100	0.1, 3.0, 10.0, 40.0, 70.0
BC_LC	CN	100	0.1, 3.0, 10.0, 40.0, 70.0
Test 3 : Effect of intercapillary separation			
SBC	N/A	N/A	3.0, 10.0
2 BC	CO	10,50,100,250,1250	3.0, 10.0
BC_LC	CO	10,50,100,250,1250	3.0, 10.0

Test 3: Effect of intercapillary separation on transport

In the third test, the capillary separation (L) is varied with respect to blood capillary diameter (d), (L/d=1, 5, 10, 25, 125), to test the solute accumulation in the tissue space as compared to the SBC configuration. Due to long computational time for each solute, this test is run for two solutes, 3kDa (representative of a therapeutic drug) and 10 kDa (representative of the size of drug carrying nanoparticle). The intercapillary separation, L, is defined as the shortest distance measured between all non-adjacent capillary pairs in a loop (46). The tissue diameter (D) is twice the separation value (D=2L) to maintain the same volume of tissue around each microvessel with respect to the SBC configuration. The surface averaged extravascular concentration is calculated at a radial distance 0.2L from the blood vessel wall in SBC configuration (C_{SBC}) as well as in the 2 BC configuration (C_{2BC}). The percentage concentration deviation shown in **Figure 1-4a** is compared across different values of intercapillary separation. The intercapillary distances for different tissue types in humans and small animals are recorded in **Table 1-2**. The blood capillary diameter, d, is 10 μm in accordance with the values reported in literature across humans, mice and rats (46, 48, 49). The L/d for tissue types shown in **Table 1-2** lies between 5 and 21.5. So, the analysis was performed for L/d=1, 5, 10, 25 and 125 for two solute molecular weights of 3.0 kDa and 10 kDa. For all the tests, the average extravascular concentration in the tissue volume surrounding the blood capillary is measured for each configuration. They are normalized by the

maximum intravascular concentration in the blood capillary volume and the concentration-time history for each test is analyzed in the Results section.

1.6.5 Non-Dimensionalization of the Convection-Diffusion-Decay process

The final objective of this paper is to assimilate results of tests 1, 2 and 3 to provide a unique non-dimensional time at which tissue solute concentration is maximum. The solute concentration-time histories in specific radial locations of the tissue space are influenced by the drainage of the solutes in addition to the advection diffusion and decay processes as modelled by **Eq 1.1**. S is the density of the micro vessels (unit is no of vessels/m) whose walls act as a sink in the tissue volume. The product of S and solute permeability (P_d^s) is the decay constant k. We assume exponential decay and define τ as the time when the inlet concentration drops to 36.7% (1/e) of the maximum inlet concentration. The first form of **Eq 1.1** is non-dimensionalized to find the time scales of the other transport mechanisms involved. Defining the following scaled variables $C_s* = \frac{c^s}{Co}; t* = \frac{t}{\tau}; x* = \frac{x}{L}; U_f* = \frac{u_f}{Uo}$, where *Uo* is the average velocity of fluid in tissue. Substituting these in **Eq 1.1**; we get the non-dimensional form as shown in **Eq 1.2**.

$$\phi \frac{\partial c^s}{\partial t} + R_F^s u_f . \nabla c^s + \nabla . (-\phi D_{tissue} \nabla c^s) = -k c^s \qquad \textbf{Eq 1.1}$$

$$\phi \frac{\partial c^s}{\partial t} + R_F^s u_f . \nabla c^s + \nabla . (-\phi D_{tissue} \nabla c^s) = -P_d^s S c^s$$

$$\frac{\phi}{\tau} \frac{\partial C_s *}{\partial t *} + R_F^s \frac{Uo}{L} U_f * . \nabla C_s * + \frac{D_{tissue}}{L^2} \nabla . (-\phi \nabla C_s *) = -k C_s * \qquad \textbf{Eq 1.2}$$

The effect of τ on the solute accumulation in a tissue space is modified by the number of microvessels (n) present around it and the intercapillary separation (L/d) between them. The solute dependent timescales, obtained from **Eq 1.2** are the modified input time scale ($n\tau \frac{L}{d}$), the diffusion timescale ($\frac{L^2}{D_{tissue}}$) and the decay timescale ($\frac{1}{k}$). These values for each solute in SBC configuration are shown in **Table 1-5**. Since different timescales are dominant at different phases and radial

locations of transport for differing solute types, a sum of all solute dependent time scales is used to non-dimensionalize the time of solute accumulation and decay in tissue as shown in **Eq 1.3.**

$$T^* = \frac{t}{n\tau\frac{L}{d} + \frac{L^2}{D_{tissue}} + \frac{1}{k}} \quad \textbf{Eq 1.3}$$

The extravascular concentration is rescaled to account for the variable solute molecular weight (Mw), solute density (ρ), tissue porosity $\emptyset$, inlet solute concentration (Co) and varying intercapillary separation (L/d) as defined by **Eq 1.4**.

$$C^* = \frac{\rho}{\phi Mw}.\frac{L}{d}.\frac{1}{Co} \quad \textbf{Eq 1.4}$$

Table 1-5: Solute dependent timescales that influence concentration in tissue across time

Solute (kDa)	Input timescale (τ) (s)	Diffusion timescale ($\frac{L^2}{D_{tissue}}$) (s)	Decay timescale (1/k) (s)
0.1	284.5	25.4	125
3	440.1	133.4	574.7
10	604.8	241.7	1428.6
40	1302	328.2	3030.3
70	2319	778.9	3333.3

1.7 Declarations

1.7.1 Competing Interests

We declare that we have no competing interests.

1.7.2 Funding

We would like to acknowledge funding provided by the National Institutes of Health Grant 5R21EB019646.

1.7.3 Authors' Contributions

SC did the numerical simulations and AO did the experimental validation. MN, PV and WW discussed and reviewed the results. All authors edited and read the final version of the manuscript.

1.7.4 Acknowledgement

We would like to thank Professor Eric Nauman for introducing us to the mixture theory model for solute and fluid transport in tissues.

1.8 Appendix

Appendix A: Mixture theory model equations

The schematic tissue configuration showing the three regions in a tissue modeled by the mixture theory equations is shown in **Figure A-1**.The conservation of mass and linear momentum equations from which the mixture theory equations are derived are stated below. The equation derivation steps are described in (13, 14) by Schuff et al.

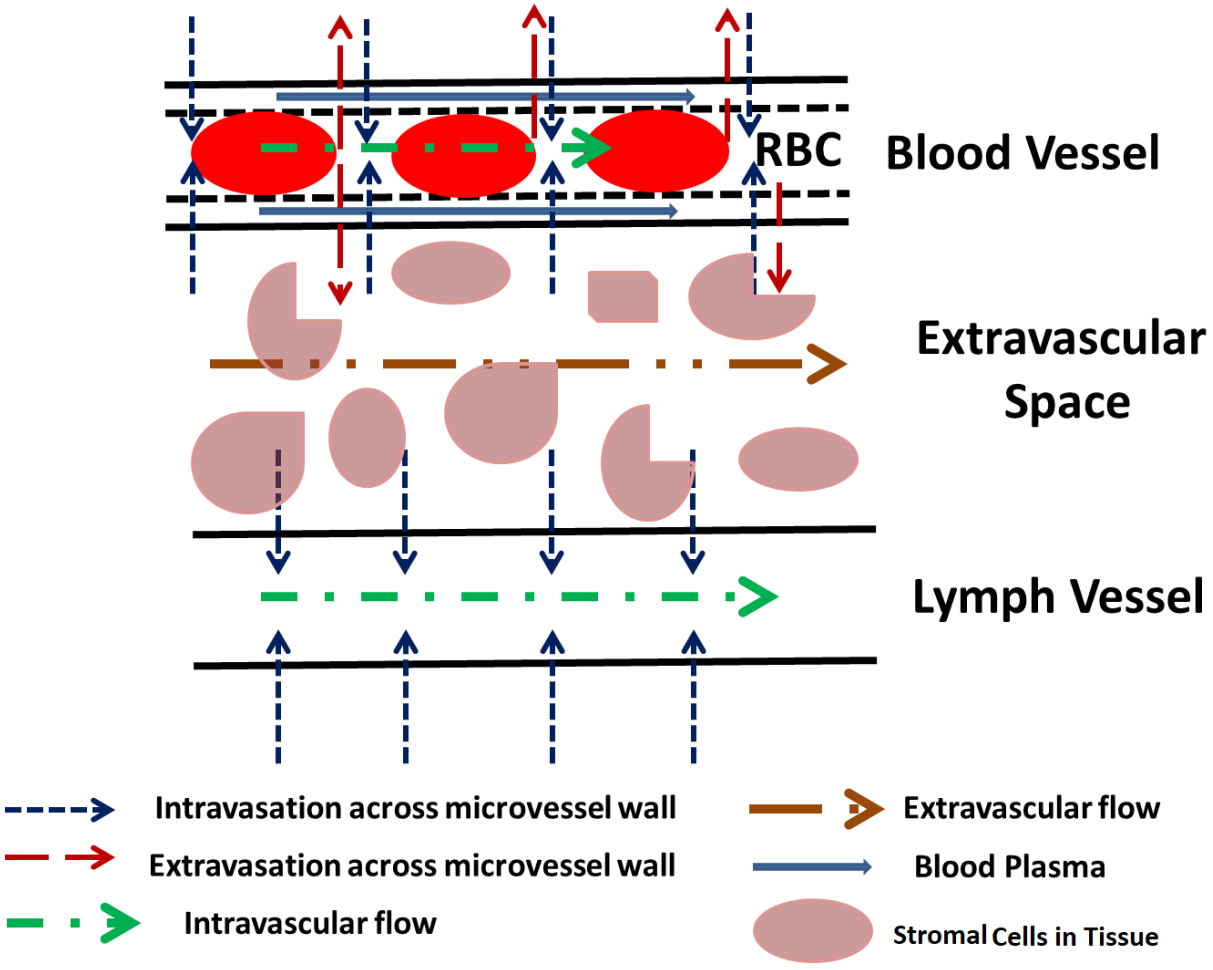

Figure A-1: Schematic tissue configuration showing the three regions in a tissue modeled by the mixture theory equations: the intravascular space (the blood vessel and the lymph vessel), the capillary wall and the extravascular space. The stromal cells are shown to indicate the non-homogeneity in the extravascular space that the mixture theory can account for.

Balance of Mass

Assuming zero rate of mass production of constituent α with density ρ^α and velocity $\boldsymbol{u}^\alpha$ in a mixture, the general expression for mass balance at each region is $\frac{\partial \rho^\alpha}{\partial t} + \nabla.(\rho^\alpha \boldsymbol{u}^\alpha) = 0$. $\boldsymbol{u}^\alpha$ is related to the extravascular/Darcy velocity of the same constituent as $\boldsymbol{U}^\alpha = \phi^\alpha \boldsymbol{u}^\alpha$ where ϕ^α is the volume fraction of constituent α. In each region the mixture was assumed to be saturated (i.e $\sum_\alpha \phi^\alpha = 1$). For the extravascular space, assuming incompressible flow and a stationary solid matrix, the mass conservation equation reduced to $\nabla.\boldsymbol{U}^f = \nabla.(\phi^f \boldsymbol{u}^f) = 0$. In our simulations due to assumption of dilute solution, $\phi^f = 1, \phi^s = \phi$.

Balance of Linear Momentum

Assuming absence of body forces per unit volume of any tumor space, the momentum equation for the constituent α is $\rho^\alpha \frac{d^\alpha \boldsymbol{u}^\alpha}{dt} = \nabla.(\boldsymbol{T}^\alpha) + \prod^\alpha$ where $\frac{d^\alpha(.)}{dt} = \frac{\partial(.)}{\partial t} + u_i{}^\alpha \frac{\partial(.)}{\partial x_i}$ is the material derivative, $\boldsymbol{T}^\alpha = -\phi^\alpha P\boldsymbol{I} + \phi^\alpha \boldsymbol{T}^{\alpha}$ is the Cauchy stress tensor, P=pore pressure and $\boldsymbol{T}^{\alpha}$ is the stress tensor for a **dense configuration** of constituent α. For fluids with viscosity μ^f, $\boldsymbol{T}^f = \mu^f(\nabla \boldsymbol{u}^f + (\nabla \boldsymbol{u}^f)^T)$. Assuming a dilute solution of solutes in the tumor, solute-solute interactions are negligible for constituent s, $\boldsymbol{T}^s = 0$. $\prod^\alpha$ accounts for the interaction terms between the different types of constituents and is subjected to the constraint $\sum_\alpha \prod^\alpha = 0$. The final forms of equations in the intravascular space, capillary wall and extravascular space are given below.

Fluid transport Equations

Intravascular Space: The arterial pressure, Par, is specified at the inlet while the prescribed hydrostatic pressure difference, ∇P balances the viscous stresses to govern the fluid flow inside the capillaries according to **Eq 1.5**.

$$-\nabla P + \mu \nabla^2 \boldsymbol{u}_f = 0 \qquad \textbf{Eq 1.5}$$

Capillary Wall: At the capillary wall, jump boundary conditions are applied as $[[\phi^f(\boldsymbol{u}^f)]].\boldsymbol{n} = 0$. The [[a]] denotes the difference of the quantity "a" across the walls where $\boldsymbol{n}$ is the unit normal outward to the wall. The fluid flux, $q_e = (\phi^f \boldsymbol{u}^f).\boldsymbol{n}$, across the capillary wall (of radius Ro) as shown in the final form (**Eq 1.6**) accounts for a) the hydrostatic pressure difference across the capillary wall due to the hydraulic conductivity, $\tilde{L}_p$, b) a constant osmotic pressure gradient, $\sigma^p(\tilde{\pi}_i^p - \tilde{\pi}_e^p)$, due to protein molecules; and c) a variable osmotic pressure that depends on the concentration difference of the injected solute (of molecular weight M_w^s and density ρ_T^s) in the intravascular (i) and the extravascular (e) space of a fibrous matrix with porosity $\emptyset$.

$$q_e = \tilde{L}_p[(P_i|_{r=Ro} - P_e|_{r=Ro}) - \sigma^p(\tilde{\pi}_i^p - \tilde{\pi}_e^p) - (\bar{P} + \frac{A}{\phi})\frac{M_w^s}{\rho_T^s}\sigma^s(c_i^s|_{r=Ro} - c_e^s|_{r=Ro})] \textbf{Eq 1.6}$$

Extravascular Space: The fluid transport in the extravascular space is influenced by a) the hydrostatic pressure difference in the tissue space, b) the hydraulic permeability of the tissue, k and c) the solute concentration gradients, ∇c^s in the tissue space as depicted in **Eq 1.7**. The retardation factor, R_F^s, is the ratio of the solute velocity and the inline fluid velocity in the tissue space. A is the interaction coefficient of the solute "s". A constant pressure Po is applied to the tissue boundary.

$$-\nabla P - \frac{\boldsymbol{U}_f}{k} + (\bar{P} + \frac{A}{\phi})\frac{M_w^s}{\rho_T^s}(1 - R_F^s)\nabla c^s = 0 \qquad \textbf{Eq 1.7}$$

Solute transport Equations

Intravascular Space: The initial solute concentration, C_o, is used to prescribe the concentration at the inflow according to **Eq 1.8**. The concentration time history for the five solutes prescribed at the blood vessel inlet is shown in **Figure A-2**. The concentration has been normalized by the peak intravascular concentration of each solute.

$$C_{inlet} = \begin{cases} \dfrac{C_o t}{15}, (t < 15s) \\ 0.5 C_o (e^{\frac{tA1}{60}} + e^{\frac{tA2}{60}}), (t > 15s) \end{cases}$$

Eq 1.8

$$A1 = -7.23(M_w^s)^{0.38}, A2 = -0.062\exp(-3.66e^{-5}M_w^s) - 0.0035\exp(-5.78e^{-7}M_w^s)$$

Assuming a dilute solution of solute "s" (i.e. $\phi^f \approx 1$) and defining the solute concentration c^s on a solvent volume basis as $c^s = \dfrac{\phi \rho^s}{M_w^s}$, the solute transport equation inside the microvessels where D_{sf} is the solute diffusion coefficient is shown below:

$$\frac{\partial c^s}{\partial t} + \boldsymbol{u}^f . \nabla c^s + \nabla . (-D_{sf} \nabla c^s) = 0$$

Eq 1.9

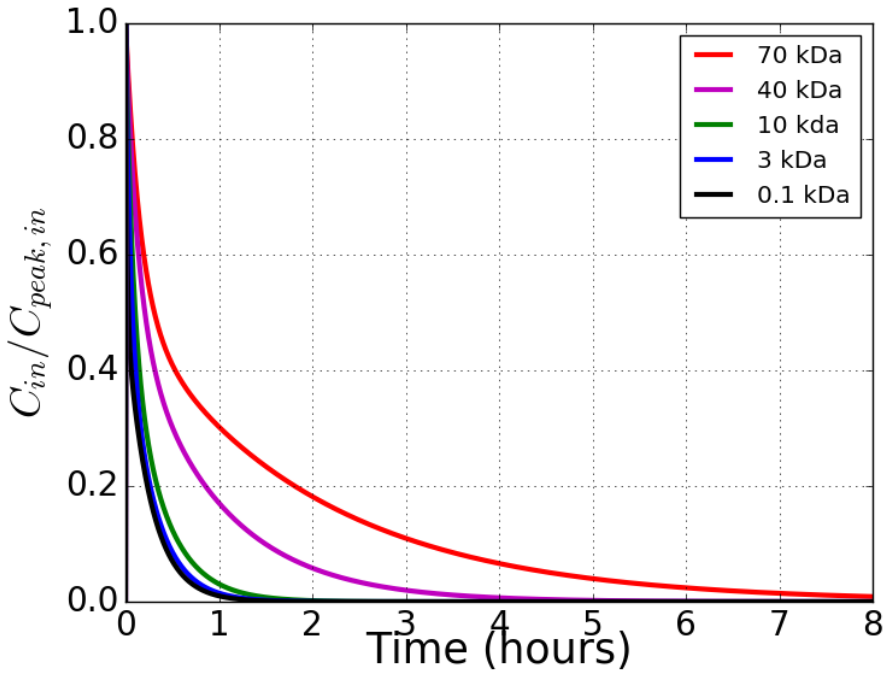

Figure A-2: Concentration vs Time profile of five solutes at the blood vessel inlet.

Capillary wall: The solute particles have the same jump boundary conditions as the fluid at the capillary wall. The solute particles carried by the fluid flux and those which permeate into the tissue space due to the concentration difference across the capillary wall constitute the solute flux

(J_s) across it. **Eq 1.10** is a modified version of Starling's law where P_d^s is the solute permeability coefficient and σ^s is the reflection coefficient.

$$J_s = \phi^f c^s \boldsymbol{u}^s . \boldsymbol{n} = P_d^s (c_i^s \mid_{r = Ro} - c_e^s \mid_{r = Ro}) + (1 - \sigma^s)\overline{c^s} q_e \qquad \textbf{Eq 1.10}$$

Extravascular Space: In the porous matrix of the extravascular space the solute undergoes both advection and diffusion as shown in the governing transport **Eq 1.11**.

$$\phi \frac{\partial c^s}{\partial t} + R_F^s \boldsymbol{u}^f . \nabla c^s + \nabla . (-\phi D_{tissue} \nabla c^s) = 0 \qquad \textbf{Eq 1.11}$$

The mixture theory equations are appropriate for this study since it shows the dependence of tissue mechanical properties like hydraulic conductivity on chemical gradients that is not captured by traditional transport models (13).

Difference of lymph vessel input parameters from that of blood vessel

Solute concentration is zero at the lymph capillary inlet. The osmotic pressure gradient due to protein molecules is absent in the lymph vessel, ($\sigma^p(\tilde{\pi}_i^p - \tilde{\pi}_e^p) = 0$). The solute permeability coefficient, P_d^s, across the lymph capillary wall is twice its value in blood capillary wall shown in **Table 1-1** to account for the free permeability of lymph vessels to macromolecules. The fluid flux and the solute flux equations are modified to allow intravasation only.

Appendix B: Fabrication of microfluidic platform

Type I collagen was used as the extracellular matrix of the tumor with a single integrated endothelialized blood vessel. Excised tendons from rat tails were dissolved in a pH 2.0 HCl solution for 12h at 23˚C. The solution was centrifuged at 30000g for 45 minutes and sterilized using 10% (v/v) chloroform for 24h at 4˚C.

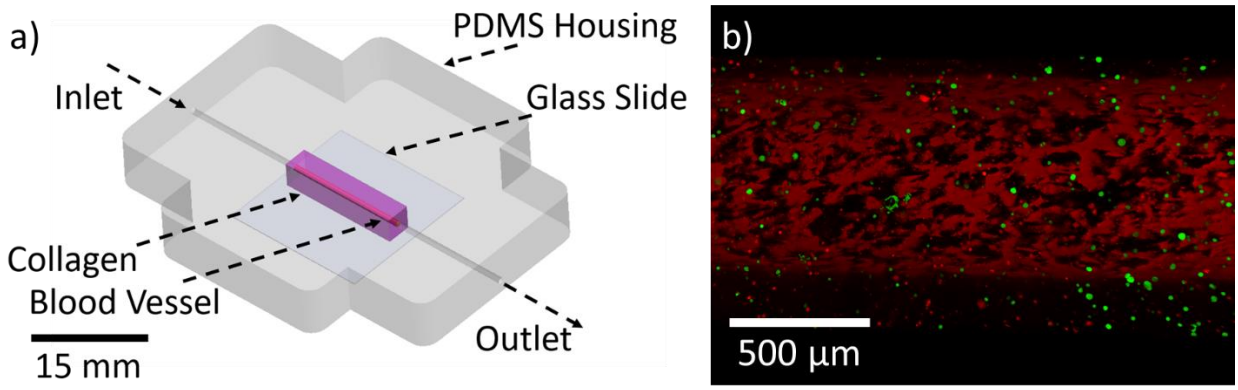

Figure B-1: 3D vascularized *in vitro* microfluidic platform for experimental validation. a) CAD drawing of the platform. b) Confocal image of blood vessel with endothelial cells (red) surrounded by breast carcinoma cells (green).

The mold for the *in vitro* tumor microfluidic platform with the embedded single vessel was fabricated as described in previous work (75, 76). PDMS housing was fabricated using common soft-lithography methods. Polydimethylsiloxane (PDMS) and curing agent was mixed with 10:1 ratio and baked at 75˚C for 1 hour. Hardened PDMS housing and the glass cover slip was plasma treated for 18W for 30 seconds. Plasma treated surfaces were assembled to create a permanent bonding. The housing was treated with 1% (v/v) polyethyleneimine in dH_2O for 10 min followed by 0.1% (v/v) glutaraldehyde in dH_2O for 20 min and washed with dH_2O twice. Collagen solution of 7 mg/ml was prepared by neutralizing stock solution with 1X DMEM, 10X DMEM, 1N NaOH, and mixing $1x10^6$/ml MDA-MB-231 breast cancer cells uniformly in collagen which was then placed in the housing. A 22G (711µm) needle was inserted into the mold and after polymerization and the needle removal, a cylindrical vascular channel was created within the collagen. $2x10^6$ TIME cells were injected into the vascular channel and exposed to flow preconditioning protocols for 3 days to form a confluent, aligned endothelialized vessel. As a result, *in vitro* platform shown in **Figure B-1** was fabricated.

Measuring mechanical properties from fabricated tissue platform

Porosity Vasculature porosity was measured using confocal microscopy and imaging mKate labeled TIME cells. Scanning electron microscopy (Zeiss, Super40) was used to image 3 fibrous matrix samples under 15kx, 20kx, and 25kx magnifications at three vertical planes. Tissue porosity was measured by applying a Frangi filter on obtained images.

Solute Permeability Obtained intensity profiles of 3 kDa and 70 kDa Dextran particles were used to calculate solute permeability coefficient as shown previously(77). 3kDa and 70kDa dextran particles were suspended in serum free endothelial basal medium at 10 µg/ml concentration and perfused in the vascular channel at 260 µL/min, which corresponds to 1 dyne/cm^2 physiological shear stress for tumor vasculatures at every 3 minutes for 2 hours. The transport of these solutes was imaged using a confocal microscope (Leica SP8, 10X magnification). Normalized intensity profiles from these images as a function of time were used to compare with normalized concentration profiles from the equivalent numerical simulations.

Solute Diffusivity Fluorescence recovery after photobleaching (FRAP) technique was used as described previously by Voigt et al. to measure the diffusion coefficient for a range of dextran molecular weights (4 kDa-150 kDa) for varying pH values, collagen concentrations and temperatures(78, 79). We selected diffusivity values of 3 kDa and 70 kDa for pH 7.6, collagen concentration 7mg/ml at 37^{0}C from the database of the mentioned study.

Hydraulic tissue permeability Hydraulic permeability for collagen at a concentration of 7 mg/ml as is used in fabrication of the platform were collected from the existing literature on vascularized *in vitro* experiments (42, 80, 81).

2. A WAVELET APPROACH FOR THE ESTIMATION OF LEFT VENTRICULAR EARLY FILLING WAVE PROPAGATION VELOCITY FROM COLOR-M-MODE ECHOCARDIOGRAMS

Authors:
Sreyashi Chakraborty[1], Brett A. Meyers[1], Hiroyuki Iwano[2,3], Michael E. Hall, MD[2], Pavlos P. Vlachos[1]

In memoriam, William Campbell Little, M.D. passed away July 9, 2015.

Affiliations:
[1]School of Mechanical Engineering, Purdue University
[2] Division of Cardiology, Department of Medicine, University of Mississippi Medical Center.
[3] Department of Cardiovascular Medicine, Faculty of Medicine and Graduate School of Medicine, Hokkaido University, Sapporo, Japan

Word Count = 5497

This chapter has been accepted for publication in Journal of Ultrasound in Medicine and Biology

2.1 Abstract

We present a new approach for calculating the left-ventricular (LV) early filling propagation velocity (VP) from color M-Mode (CMM) echocardiograms using wavelet analysis. Current methods for measuring VP do not account for the spatiotemporal variation of the VP. They are confined by empirical assumptions and user inputs that hinder the accuracy of VP, limiting its clinical utility.

We evaluated three methods for measuring LV early filling: conventional VP, the strength of propagation (VS), and VP determined from the most energetically significant wave (Peak-VW). We used Group A with 125 patients, n=50 normal filling, n=25 impaired relaxation, n=25 pseudonormal filling and n=25 restrictive filling; and Group B with 69 patients, n=32 normal, n=15 dilated, and n=22 hypertrophic. Peak-VW most accurately distinguished normal from diseased patients. For Group A, the receiver operator characteristics (ROC) area under the curve (AUC) was 0.92 for Peak-VW, versus 0.62 for VP, 0.63 for VS and 0.58 for intraventricular pressure difference (IVPD). These correspond to 50-70% improvement in classification ability. Similar improvements were found for Group B.

Peak-VW may provide a more accurate evaluation of diastolic function than standard methods and enable better diagnostic classification of patients suffering from diastolic dysfunction.

Keywords: left ventricle early diastole, early filling, propagation velocity, wavelets

2.2 Introduction

The diastolic function of the left ventricle (LV) can be evaluated from color M-mode (CMM) Doppler echocardiography, which records a spatiotemporal map of blood velocity along a scan-line from the mitral valve towards the apex (82). One or more combinations of hydrodynamic parameters that characterize ventricle filling are calculated from the CMM scans. Some standard metrics from CMM scans used to assess LV diastolic dysfunction are the propagation velocity (VP) and the intraventricular pressure difference (IVPD) (83-85). In chronic heart failure (HF) patients, early diastolic IVPD during exercise was found to be closely related to the exercise capacity, regardless of LV ejection fraction (86). Apical IVPD (middle of the LV to the apex) was found to reduce total IVPD in HF patients while the basilar IVPD (left atrium to the middle of the LV) was maintained by elevated atrial pressure (87). Previous work from our group provided improvements on the IVPD measurement by calculating it from a representative beat reconstructed by combining multiple heartbeats of the same patient and rectifying the low resolution of CMM scans (88). Calculations of IVPD from magnetic resonance imaging (MRI) was shown to be more accurate than CMM IVPD when both were compared against computational fluid dynamic (CFD) measurements of IVPD as the ground truth (89). IVPD calculations from 2D phase-contrast MRI showed a correlation with vortex ring formation at the mitral valve tips and its subsequent propagation into the ventricle (90).

The VP is conventionally measured as the slope of an iso-velocity contour of the blood velocity map, typically set at 50% of the maximum inflow velocity, from the mitral annulus to a distance of 4 cm into the LV (82). This corresponds to the speed of the diastolic filling impulse, advancing through the mitral valve towards the apex of the LV. It is assumed the filling wave has a constant VP throughout the early diastole when the slope is fit. However, the iso-velocity contour is curvilinear, indicating that the propagation velocity is not constant during early filling (91). In

previous work, we found that describing VP using two slopes, one corresponding to a rapid initial and one a slower terminal VP, provided a more accurate representation of early filling (92).

Furthermore, the strength of propagation (VS) during filling, the product of the initial VP and the distance it travels into the LV, provides a small improvement in assessing diastolic function (92). Although this simple correction improves VP estimation, it does not capture the physical process by which the VP varies smoothly during the early filling process. Moreover, the VP depends on the choice of aliasing boundary, corresponding to different iso-velocity contours (93, 94), indicating that early diastolic LV filling is not a bulk wave moving with a constant velocity but instead is comprised of a range of spatiotemporally varying propagation velocities. CMM scans, although scarcely used for clinical routines, has considerable potential for deciphering flow physics owing to the high temporal resolution. This is untapped until now because only a linear fit on the scan is used to calculate VP instead of utilizing the entire spatiotemporal map recorded by the sonographer.

This work aims to develop a new approach for the calculation of the LV early filling propagation velocity from CMM echocardiograms free of assumptions and heuristics, that can capture the underlying physics with high fidelity. The proposed method uses wavelets to analyze the early diastolic LV filling wave from CMM scans and does not use any of the assumptions inherent in the traditional calculation of VP, such as the subjective selection of iso-velocity contours, or measuring a slope based on an iso-velocity contour. In this work we demonstrate that this automatic, objective, reproducible and user independent approach yields a more accurate, robust, and physically consistent estimation of VP.

2.3 Materials and Methods

2.3.1 CMM Acquisition

The study was conducted according to protocols approved by the Virginia Tech and Wake Forest University Baptist Medical Center Institutional Review Boards (IRB). Patients were all undergoing clinically indicated echocardiography at the Wake Forest University Baptist Medical Center This study involved only retrospective analysis of clinically indicated echocardiograms for de-identified subjects. The study was reviewed by the Purdue IRB and was accepted. Informed consent is not applicable here. Doppler echocardiographic examinations were completed using an

iE33 and a multiple frequency transducer (Model S5-1; Philips Medical Systems, Andover, Massachusetts, USA). CMM echocardiograms were recorded in the apical four-chamber view with a color scale that optimized visualization as judged by the recording sonographers. The velocity map in all CMM scans was reconstructed using a de-aliasing technique (92, 95) before calculating the flow metrics like VP, VS, VW, and IVPD.

Table 2-1: Group A patient characteristics

Diastolic Dysfunction Stage	Number of Patients	Age (years)	E/A	E/E'	Ejection Fraction
N (Normal)	50	38.6±15.1	1.8±.4	6.8±1.9	0.6±0.1
IR (Stage 1 - Impaired relaxation)	25	68.3±9.6	0.8±0.1	13.0±4.2	0.6±0.1
P (Stage 2-Pseudonormal)	25	66.2±12.9	1.6±0.3	16.4±5.3	0.4±0.2
R (Stage 3-Restrictive)	25	59.4±18.5	2.9±1.0	18.8±7.4	0.3±0.1

*Patients are classified based on clinically diagnosed diastolic function stage. Values represent mean±SD (standard deviation).
† E/A= E–wave to A-wave transmitral velocity ratio
‡E/E'= transmitral Doppler E-wave velocity to mitral annular tissue Doppler E-wave velocity ratio.

Patient Cohorts

Two patient groups were used in this analysis: Group A, for comparison of different diastolic function grades (n=125) and Group B, for comparison of different LV geometries (n=69). To evaluate LV diastolic dysfunction, Group A consisted of the following:

- Normal (N) filling, n=50
- Impaired relaxation (IR), n=25
- Pseudonormal (P) filling, n=25
- Restrictive (R) filling, n=25.

Patient characteristics for each group are provided in

Table 2-1. Patients were classified based on clinically diagnosed diastolic function stage according to the guidelines (82). To evaluate heart failure with structural remodeling, Group B is comprised of three patient cohorts (**Table 2-2**) that are classified based on left ventricular geometry:

- Normal (N) cohort (n=32), without any abnormal echocardiographic findings including a normal filling pattern based on peak early filling mitral inflow velocity and normal mitral annular tissue Doppler velocities (Nagueh et al. 2009).
- Severe LV hypertrophy (LVH) cohort (n=22) indicated by an elevated LV mass index (LVMI) with a cutoff value of 115/m^2 for males and 95g/m^2 for females (Feigenbaum 2015; Lang et al. 2005).
- Dilated cardiomyopathy (DCM) cohort (n=15) based on a reduced sphericity index (SI) (SI<1.6) (Madaric et al. 2007) and a reduced ejection fraction (<40%) and based on the clinical diagnosis by the physicians.

Table 2-2: Group B patient characteristics

Subgroup	Number of patients	Age (years)		Ejection Fraction		Geometry Classifier
		Median	IQR	Median	IQR	
N(Normal)	32	30	24	60	8	Normal
D (DCM)	15	58	15	20	10	SI < 1.60
H (LVH)	22	60	9	16	7	LVMI > 175

* Values reported are median and interquartile range, IQR (75% value - 25%value)
† LVMI-Left Ventricular Mass Index
‡ SI-Sphericity Index

2.3.2 Continuous Wavelet Transform Applied on Wave Propagation Velocity

The propagation velocity is a function of the spatial shift of the velocity signals between two time-points t_1 and t_2. This spatial shift divided by the known time-step ($\Delta t = t_2 - t_1$) provides an estimate of the propagation velocity. A general way to estimate the average spatial lag is by performing a cross-correlation (CC) between the two velocity signals. The peak of the correlation function provides the spatial lag estimation needed herein.

Wavelet decomposition analysis was used to measure each wave component present in the filling wave. Fourier methods are typically used to identify the wavenumbers present in a signal. However, the Fourier transform does not provide space or time localization for each wave component, which is needed here. The short-time Fourier transform (STFT) works well for sinusoidal decompositions while the continuous wavelet transform (CWT) generalizes the concept of decomposition by implementing a variety of basis functions that suits highly non-stationary and non-periodic cardiac signals. Moreover, for the STFT, the window length is set at a fixed temporal

length and number of cycles of the carrier frequency component. In contrast, the wavelet analysis window can be translated as well as stretched and contracted, hence yielding better temporal resolution for the wavelet transform in the high frequency range, at the expense of possibly reduced frequency resolution. These characteristics of the wavelet transform are better suited for the present analysis. As a result, the use of the wavelet transform is best for analyzing these signals, which contain multiple scales, provides spatial and temporal localization of all wavenumbers, and enables us to calculate a new VP independent of iso-velocity assumptions.

The CWT, given in **Eq 2.1**, convolves a signal $f(x)$ with a series of scaled and translated continuous mother wavelet functions, $\psi(\frac{x-b}{a})$, centered at *x*, to calculate the signal energy as a function of space and wavenumber. The scaling parameter, a, stretches or compresses the mother wavelet to capture different wavenumbers and translates it by *b* to provide space localization.

$$\boldsymbol{W_T(a,b) = a^{-1/2} \int f(x) * \psi(\frac{x-b}{a})\, dx} \qquad \textbf{Eq 2.1}$$

A stretched wavelet will capture the energy of low wavenumber components, while a compressed wavelet captures the energy of high wavenumber components. The results of a CWT are dependent on the choice of mother wavelet and scales. The complex Morlet wavelet, **Eq 2.2**, which was chosen for this analysis, is a sine wave modulated by a Gaussian window. Its utility in biological applications is enhanced by its smooth continuous oscillations, as has been previously demonstrated (96).

$$\Psi(x) = \frac{1}{\sqrt{\pi f_b}} e^{i2\pi f_o x} e^{\frac{-x^2}{f_b}} \qquad \textbf{Eq 2.2}$$

The frequency parameter, f_o, defines the frequency of the sine wave component and the bandwidth parameter, f_b, defines the bandwidth of the Gaussian modulating window. By controlling these two parameters, the mother wavelet can be optimized for the given input, with the stipulation that the mother wavelet must have near zero mean and have endpoints with zero magnitudes. According to previous studies, the near zero mean is possible only for 5-7 oscillations (97, 98). So, we optimized the frequency parameter ($\boldsymbol{f_o}$) and then solved for a bandwidth parameter ($\boldsymbol{f_b}$) to maintain six (6) oscillations in the wavelet function. The Nyquist criterion is considered to calculate $\boldsymbol{f_o}$ as twice the cutoff frequency required to achieve an optimum signal to noise ratio for the velocity map. The relationship of the input parameters can be expressed by:

$$f_b = \frac{n_{cycles}}{2\pi f_o} \qquad \text{Eq 2.3}$$

The minimum wavenumber of interest is set to the minimum resolvable wavenumber from the CMM echocardiogram, or the inverse of the physical length of the CMM image. The maximum wavenumber to scale the mother wavelet is set to the wavenumber representing an estimated signal-to-noise ratio cut-off. One hundred equally spaced scaling factors were generated to scale the mother wavelet from the minimum wavenumber to the maximum wavenumber.

2.3.3 Calculating Wave Component Propagation Velocity

The result of the CWT applied to a spatiotemporal map of velocity values is a three-dimensional CWT power spectrum, localized in space (x), time (t), and wavenumber (k) as shown in **Figure 2-1.**

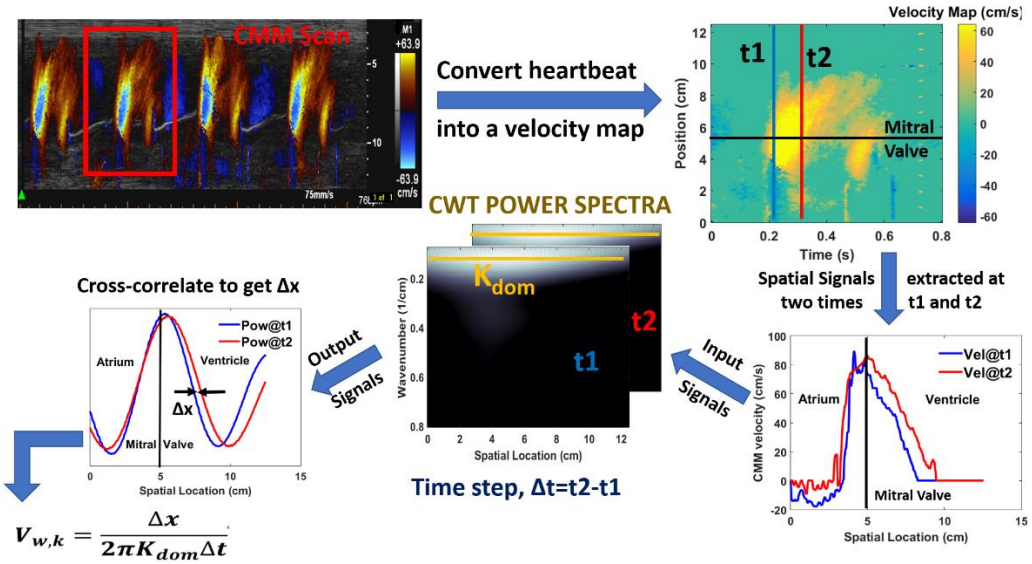

Figure 2-1: On the top left a heartbeat from a CMM scan is selected and two spatially varying signals corresponding to times t1 and t2 are extracted from it on top right. The CWT transform for each time signal (on bottom left) provides the power spectra shown in the bottom middle figure, from which the dominant wavenumber is determined. The bottom right figure shows a schematic of a representative spatial variation of power for each time signal at its dominant wavenumber. The spatial lag, Δx, shown in the figure, the known time difference, Δt, and the dominant wavenumber, K_{dom} combine to give the peak propagation velocity, $V_{W,k}$.

The phase lag of each wavenumber between two time steps is performed using a phase-only cross-correlation (99) . This phase lag, Δx, and the known time difference between the two time-steps, Δt, was used to calculate a propagation velocity corresponding to each wavenumber, $V_{w,k} =$

$\Delta x/(2\pi k\Delta t)$. The time step Δt was manually chosen to be different for different disease stages and was set to 0.02 sec for normal subjects and 0.04 for the diseased ones.

As a byproduct of the CWT, all orthogonal waves whose linear superposition comprises the entire filling wave are obtained. This allows for any wave component of physical interest or any combination of those waves to be directly extracted, and the wave-specific VP be estimated. This capability provides the means to eliminate heuristic selections of filling velocity iso-contours and calculate VP for each wavenumber. We used the VP of the most energetically dominant wavenumber (Peak-VW) to characterize early diastolic filling (**Figure 2-2**). For the remainder of this paper, we refer to this parameter as 'Peak-VW'.

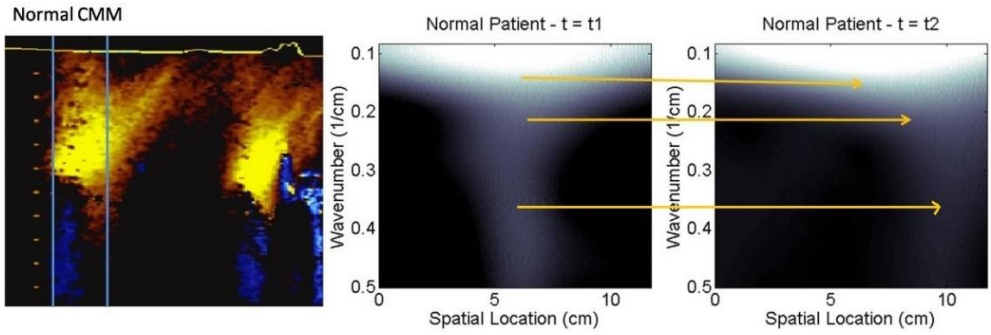

Figure 2-2: Representative wavelet analysis. The first column shows the CMM echocardiogram for a normal filling representative patient with t1 and t2 indicated by the vertical blue lines. The next two columns show the CWT power spectra at t1 and at t2. The yellow lines show the motion of the peaks at different wavenumbers. The CWT is applied to each temporal velocity signal on the CMM echocardiogram resulting in a CWT power spectrum localized in space, time and wavenumber. The spatial lag of the peak on the CWT power spectra is calculated between two time steps, for each wavenumber (horizontal location). The spatial lag and the time between the two time signals are used to calculate a propagation velocity for each wavenumber. As evident from the CWT images, higher wavenumbers have higher displacements than lower wave numbers. The range of dominant wavenumbers is specific to each patient. The minimum wave number considered is the inverse of the physical length of the LV. The maximum wavenumber is also specific to each patient and is dependent on the most energetic wave components in each signal.

2.3.4 Conventional Propagation Velocity (V_p) and Filling Strength (V_s)

The conventional VP parameter (82) was calculated as previously described in (92). The filling strength parameter, VS, was calculated as the product of the initial VP and the distance it extended into the LV (92). These calculations are performed using automated computer programs, increasing objectivity and reducing variability (92).

2.3.5 CMM Derived IVPD

A Doppler-derived IVPD was computed using the CMM echocardiogram velocity data and the Euler equation (84, 85), given in **Eq 2.4**.

$$\frac{\partial P}{\partial x} = -\rho\left[\frac{\partial U}{\partial t} + U\frac{\partial U}{\partial x}\right] \qquad \textbf{Eq 2.4}$$

where U is velocity, P is pressure and ρ is the density of blood. Spatial and temporal derivatives are calculated and used to solve for $\frac{\partial P}{\partial x}$. The line integral along the ventricle length is calculated at each time step, yielding a spatiotemporal profile of pressure values, $P(x,t)$. A temporal profile of IVPD is calculated by subtracting the pressure at the mitral valve from the pressure at the apex. The peak IVPD during early filling is then identified. This method has been validated with direct invasive pressure measurements by micro manometers (85, 95, 100).

2.3.6 Intra-Operator and Inter-Operator Variability Analysis

Three different observers analyzed a random set of 15 beats for the inter-operator variability analysis and one observer analyzed 3 beats 15 times for intra-operator variability analysis. **Table 2-3** displays the results of this analysis for each observer. The median coefficients of variation are calculated according to the following equation and reported as a variability metric:

$$Coefficient\ of\ Variation\ (\%) = \frac{100}{N}\sum_{i=1}^{N}\frac{standard\ deviation}{median}$$

Table 2-3: Results of intra-observer variability and inter-observer variability for each parameter. Peak-Vw reports the smallest variability when compared to conventional parameters.

Coefficient of variation (%)	VS	VP	Peak-VW	IVPD
Median Intra-observer	12	10.5	3.7	5.8
Median Inter-observer	19.6	17.2	10.1	14.5

2.3.7 Statistical analysis

All patient cohort data are expressed as mean ± standard deviation. Medians and interquartile ranges (IQR) were also analyzed. We analyzed differences among groups using the Tukey-Kramer Honestly Significant Difference (HSD) test, which compared the means of each pair of patient subgroups. The ability of the metrics to distinguish between patient sub-groups was analyzed using

receiver-operator characteristic curves (ROC), specifically by comparing the area under the ROC curves (AUC). All data analyses were performed using Matlab (The Mathworks, Natick, Massachusetts, USA).

2.4 Results

2.4.1 Intra-Operator and Inter-Operator Variability Analysis

Peak-VW had the smallest variability of 3.67 % intra-operator and 10.1% inter-operator, a 60-200% improvement compared to the conventional parameters VP, VS, and IVPD.

Table 2-4: Summary of results for Group A.

	IVPD (mmHg)		VP (cm/s)		VS (cm^2/s)		Peak-VW (cm/s)	
	Median	IQR	Median	IQR	Median	IQR	Median	IQR
N	2.7	1.9	50.7	26.9	167.1	148.7	55.4	12.4
IR	1.8	1.5	37.9	39.9	123.73	163.7	44.3	10.2
P	2.5	1.9	46.2	31.4	140.3	138.8	33.7	11.7
R	2.9	1.9	36.7	17.9	76.7	87.4	19.6	19.0

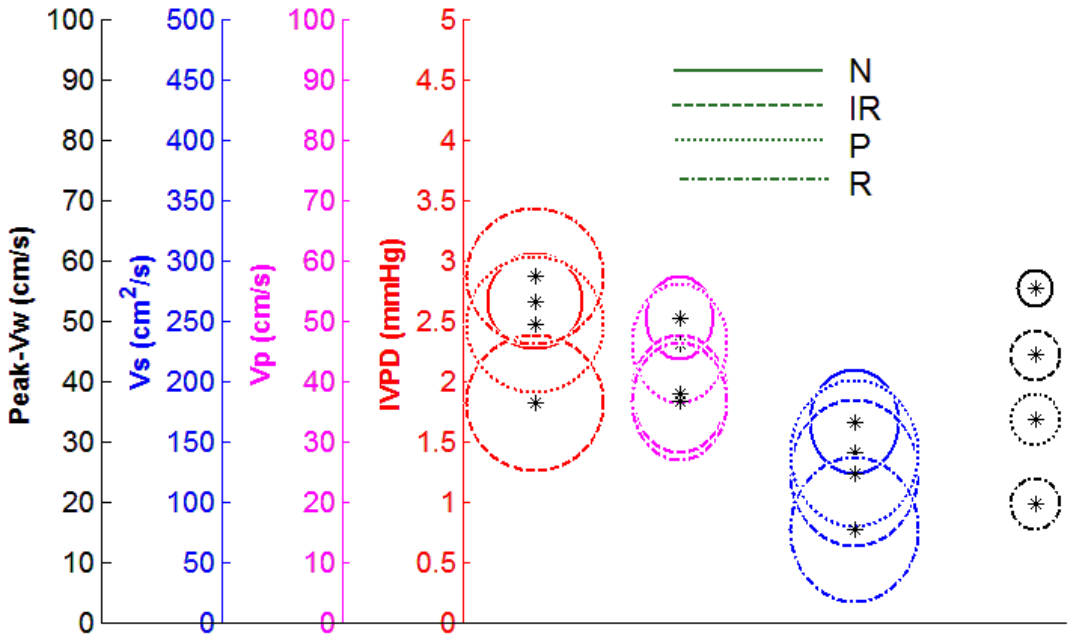

Figure 2-3: Color-M-Mode based parameters for each patient cohort for group A. The black star at the circle center denotes the median value of each parameter in each cohort. The radius of the circle denotes the deviation in each parameter. Color of the deviation circles denotes methodology and corresponds to axis colors.

Moreover, it should be noted that the VP, VS, and IVPD are also calculated with our automated software and have higher repeatability than traditional manual calculations.

2.4.2 Group A: Diastolic Dysfunction

Peak IVPD, VP, VS, and Peak-V_W values for the cohort are plotted in **Figure 2-3**. **Table 2-4** shows the medians and the IQRs for each group. IVPD was reduced in the IR group compared to the N group (1.81 +/- 1.5 mmHg versus 2.66 +/- 1.97 mmHg, respectively). There was a progressive increase in IVPD as the diastolic dysfunction stage worsened from IR to P to R (Table 4). VP, VS, and Peak-VW were all lower in groups with diastolic dysfunction compared to normal patients.

Table 2-5: p-values from Tukey-Kramer HSD test for Group A. The shaded values signify statistical significance. The wavelet based peak propagation velocity has highest statistical significance.

Parameter	Filling Pairs		p-value
IVPD (mmHg)	N	IR	0.0024*
	N	P	0.8887
	N	R	0.9975
	IR	P	0.0628
	IR	R	0.0185*
	P	R	0.9681
VP (cm/s)	N	IR	0.2111
	N	P	0.9558
	N	R	0.1008
	IR	P	0.5975
	IR	R	0.9896
	P	R	0.4064
VS (cm^2/s)	N	IR	0.9986
	N	P	0.7375
	N	R	0.0644
	IR	P	0.7387
	IR	R	0.1816
	P	R	0.0146*
Peak-VW (cm/s)	N	IR	<0.0001*
	N	P	<0.0001*
	N	R	<0.0001*
	IR	P	0.006*
	IR	R	<0.0001*
	P	R	0.0015*

However, as shown in both **Figure 2-3** and **Table 2-4**, only Peak-VW showed a consistent decrease with worsening diastolic dysfunction stage.

Table 2-5 quantifies the ability of each method to distinguish between diastolic function groups. Peak-VW was able to differentiate all the disease subgroups (6 out of 6 pairs) ($p<0.0001$ for N vs P, N vs IR and N vs R, $p=0.006$ for P vs IR, $p<0.0001$ for IR vs R and $p=0.0015$ for R vs P). VP did not differentiate any pair of disease stages. IVPD differentiated 2 pairs ($p=0.0024$* for N vs IR and $p=0.0185$* for IR vs R) while VS differentiated 1 out of 6 pairs of disease stage combinations ($p=0.0146$ for P vs R). The AUCs on the ROC curves are plotted in **Figure 2-4**. In this plot, the diseased state includes all patients with diastolic dysfunction of IR, P, and R. The Peak-VW (AUC=0.92) showed significantly improved classification ability over the Doppler-derived IVPD (AUC=0.58), VP (AUC=0.62), and VS (AUC=0.63).

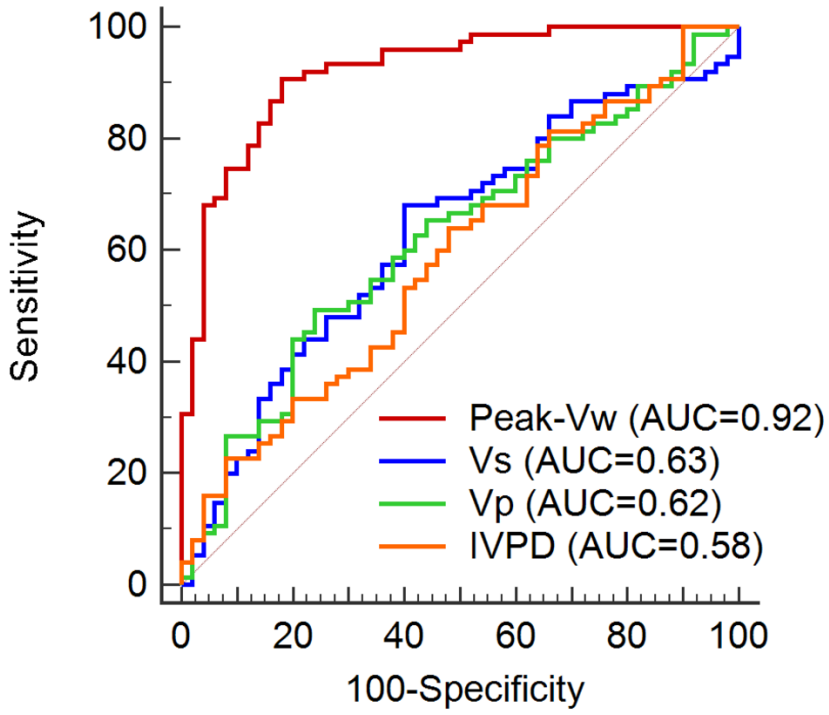

Figure 2-4: Receiver Operator Characteristic (ROC) curves for three conventional parameters and for the proposed wavelet parameter of Group A. The area under the curve (AUC) is noted in the legend for each parameter. The plot differentiates the normal filling cases from diseased filling ones. The maximum wave component peak-VW displays the highest AUC.

2.4.3 Group B: Dependence on Left Ventricle Geometry

Peak IVPD, VP, VS, and Peak-VW values for patient cohorts corresponding to Normal, DCM and LVH groups are shown in **Figure 2-5**. The group median and the IQRs are reported in **Table 2-6**. Both diseased patient cohorts displaying LV remodeling (DCM and LVH) showed decreased

values for all methods than the Normal patient cohort. Furthermore, all methods could classify the normal group against each of the diseased groups with statistical significance.

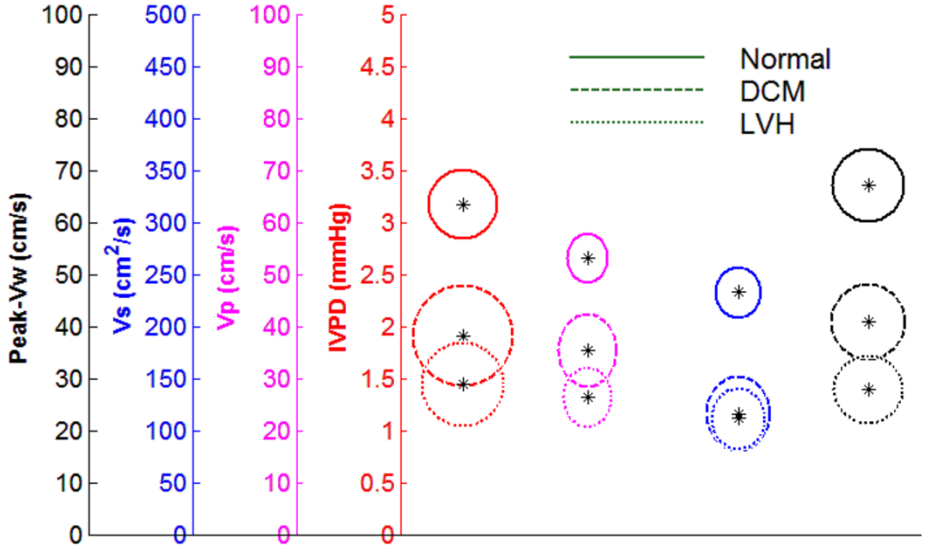

Figure 2-5: CMM based parameters for each patient cohort in group B. The black star at the circle center denotes the median value of each parameter in each cohort. The radius of the circle denotes the deviation in each parameter. Color of the deviation circles denotes methodology and corresponds to axis colors.

Table 2-6: Summary of results for Group B.

	IVPD (mmHg)		VP (cm/s)		VS (cm^2/s)		Peak-VW (cm/s)	
	Median	IQR	Median	IQR	Median	IQR	Median	IQR
N	3.2	2.0	53.1	24.4	232.8	153.4	67.2	23.2
LVH	1.4	1.3	26.4	13.8	111.4	89.2	27.8	14.1
DCM	1.9	0.9	35.3	23.8	116	132.6	40.8	5.9

IVPD (p = <0.0001 for N vs LVH, and p = 0.0015 for N vs DCM), VP (p = <0.0001 for N vs LVH, and p = 0.0011 for N vs DCM), VS (p = <0.0001 for N vs LVH, and p = 0.0002 for N vs DCM), Peak-VW (p = <0.0001 for N vs LVH, and p < 0.0001 for N vs DCM). However, Peak-VW was able to delineate the diseased groups from the normal group more clearly. Furthermore, it was the only metric that better classified between DCM v LVH (p= 0.2171, **Figure 2-5**). In addition, the improved clinical utility of Peak-VW over IVPD, VP, and VS was further supported by the increased AUC (**Figure 2-6**). In **Figure 2-6(a),** both remodeling geometries are treated as diseased and compared with the normal filling cohort. The Peak-VW (AUC=0.994) shows the highest AUC, followed by VS (AUC=0.886), VP (AUC=0.864), and IVPD (AUC=0.851). The AUCs for all methods are statistically significant (p<0.0001). More importantly, the second ROC curve in

Figure 2-6(b) differentiates the dilated ventricles from the hypertrophied ones. For this case as well, the highest AUC is obtained by the wavelet-based Peak-Vw (AUC=0.864) and it is the most statistically significant prediction (p=0.0004) as compared to VS (AUC=0.655), VP (AUC=0.685), and IVPD (AUC=0.697). The p-values for all cases were reported with a confidence level of 95%.

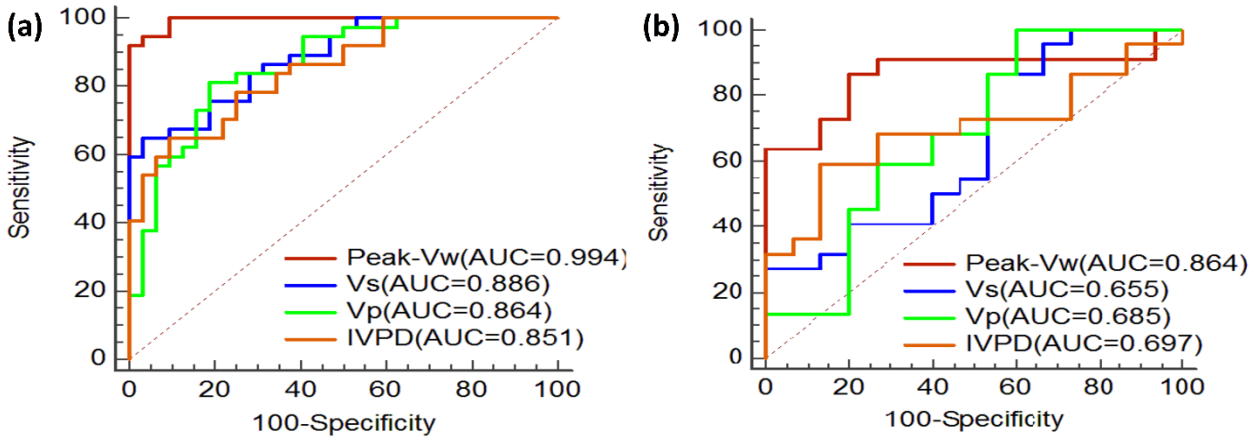

Figure 2-6: Operator Characteristic (ROC) curves for all methods of the Group B. The area under the curve (AUC) is noted in the legend for each parameter. (a) The classification is based on normal ventricle geometry versus remodeled ones. (b) The classification is based on LVH ventricle geometry versus DCM ones for the plot on right.

2.5 Discussion

We developed a new method based on wavelet analysis to calculate the LV filling wave propagation velocity. This new parameter, termed Peak-VW, identifies the most energetic and dominant filling wave during diastolic flow and directly measures its propagation speed. Physically it captures the combined effect of the strength and energy of the LV suction and the effect of the shape of the LV. For example, the shape of the LV, a dilated versus a hypertrophic LV would exhibit different filling wave propagation velocities even under the same IVPD since the distribution of momentum for the filling flow is shape dependent. Although Peak-VW is conceptually parallel to the traditional VP, we found that it can better capture the physics and provide a more accurate and clinically useful evaluation of LV diastolic function. Peak-VW is an indirect measure of the left ventricle's filling efficiency in the initial phase of the diastole. Moreover, this method is objective, free of heuristics, and as a result has significantly lower inter- and intra-operator variability.

VP is conventionally measured as the slope of an iso-velocity contour of the blood velocity map, set at 50% of the maximum inflow velocity from the mitral plane to a distance of 4 cm into the LV (82). Done in this manner, VP provides a useful measure of LV relaxation. Furthermore, the ratio of the peak mitral valve inflow velocity (E) to VP (E /VP) can be used to estimate the LV filling pressure. This is based on the assumption that the filling wave has a constant VP throughout early diastole. However, the iso-velocity contour is curvilinear, indicating that the VP is not constant during early filling (91). Moreover, the VP depends on the choice of aliasing boundary, corresponding to different iso-velocity contours (93, 94), suggesting that early diastolic LV filling is not a bulk wave moving with a constant velocity but instead is comprised of a range of spatiotemporally varying propagation velocities. Hence, there are several potential limitations to using VP as a measure of LV diastolic function. In addition, VP is subject to variability based on how the isovelocity contour is determined (82, 101, 102). Finally, VP is normal in patients with hypertrophic cardiomyopathy (HCM) who have diastolic dysfunction apparent by other methods (102). We previously attempted to address these limitations by describing VP by two slopes, corresponding to a rapid initial and a slower terminal VP, which provided a more accurate representation of early filling (92). As a result, the product of the initial VP and the distance it travelled into the LV (VS) provided a small improvement in assessing diastolic function. To better account for these potential limitations to the conventional method of determining VP, we developed a more physiologically robust approach. We used a continuous wavelet transform with varying time-step sizes for each disease stage to analyze the CMM LV filling wave without making other assumptions concerning the bulk transfer of blood into the LV. This enables the calculation of the propagation velocity for the most energetic wave, VW. Our new measure when calculated at the correct time-step provided better recognition of diastolic function than VP, VS, or IVPD. This improvement was apparent with both cohorts evaluated herein, namely in patients with diastolic dysfunction (Group A) and LV dilatation and LVH (Group B).

In **Figure 2-7** we plot the peak-VW calculated using a spatial cross-correlation (without using wavelets) for a series of time-steps (dt). The Normals and LVH peak-VW variation shows a rise-decay trend while the Restrictives and DCM patients show a plateau trend (Normals, dt=0.012 Restrictives and LVH, dt=0.06; DCM, dt=0.04). The presence of spurious noise in the CMM scans causes a false peak-VW in the diseased stages at a lower time-step but they plateau to a constant peak-VW for a higher time step. The physical significance of the “peak” and “plateau” trends is

not fully understood yet. Ongoing work involves automating the algorithm to determine the time-step for each scan before choosing the peak-VW.

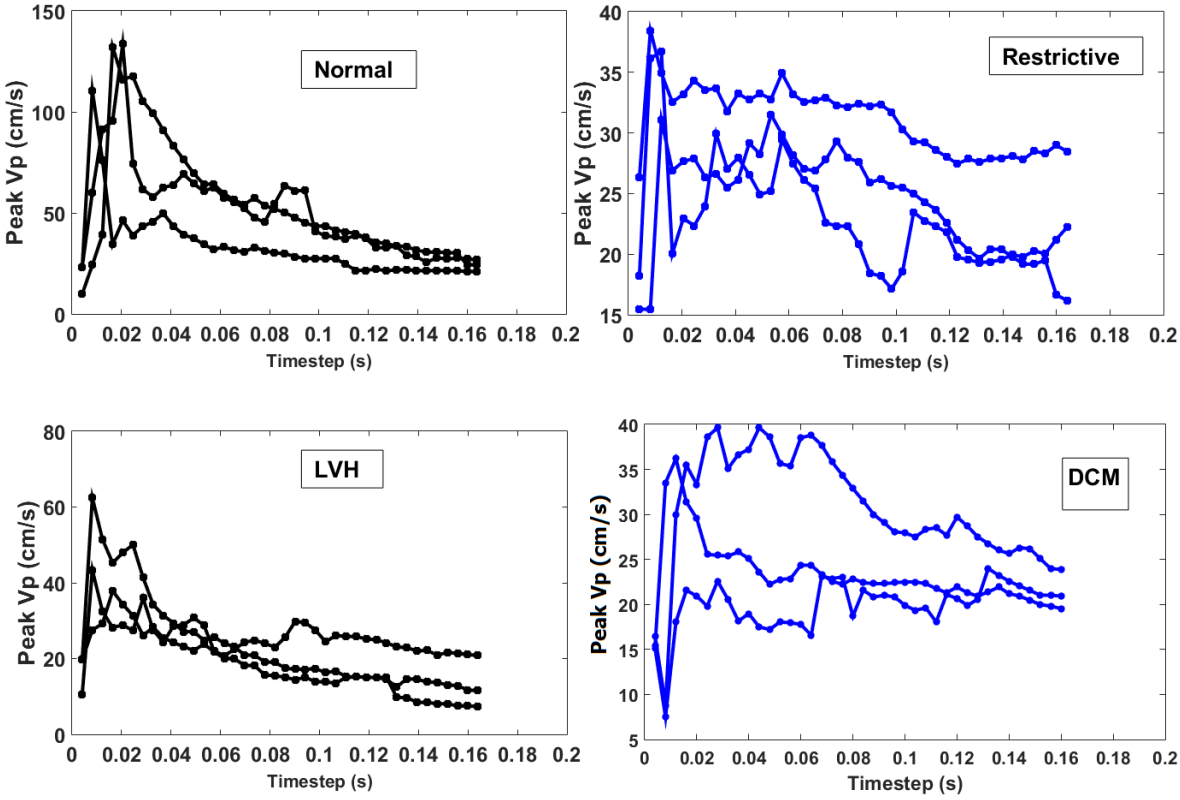

Figure 2-7: Variation of peak-VW (labelled as peak VP for this demonstration) with changing time step size shown for 3 sample patients in each of the Normal, Restrictive, LVH and DCM cohorts.

VP and IVPD have been developed as indices of LV suction, however, their limitation under conditions of pseudo-normalization caused by elevated left atrial pressure has been documented (103). This is also supported by our results, in which VP and IVPD are higher in P than in IR. The newer index, VS, also could not overcome this limitation in the present analysis. In contrast, Peak-VW measurements were significantly reduced in P compared to IR and N, indicating that this new approach to calculating propagation velocity could discriminate P from N, and that Peak-VW would be a robust marker of LV suction.

Moreover, Peak-VW could also differentiate LVH and DCM. In a hypertrophied heart, the suction is reduced due to impaired longitudinal LV function (104). On the other hand, in a dilated heart, LV suction decreases due to the flow disturbance in the enlarged chamber and the reduced recoil caused by systolic dysfunction (105). These differences in the upstream of reduced LV

suction could have resulted in the differences in Peak-VW between LVH and DCM. Although the discrimination between LVH from DCM using Peak-VW may not impact the clinical practice, it could provide new insights for the understanding of complicated pathophysiology in LV diastolic function. Overall, this study suggests that Peak-V_W offers the clinical potential of determining worsened diastolic function with minimal user input. This clinical ability may be more useful when a combination of traditional measures like mitral inflow velocities, tissue Doppler velocities, relaxation time, and ejection fraction are indeterminate due to arrhythmias (103, 106, 107) or regional wall motion variation (108), and when there are segmental differences in tissue Doppler velocities (109). Emerging techniques of speckle tracking echocardiography measuring global strain and strain rate (SR) of the left ventricle provide incremental improvement in the diagnostic capability of patients with normal ejection fraction but suffering from myocardial infarction (110, 111). In the presence of diastolic dysfunction, circumferential SR was influenced by changes in IVPD, but longitudinal SR remained unaffected by IVPD variations with an abnormal temporal non-uniformity causing a delay of longitudinal relative to circumferential expansion (112, 113). Left atrium strain has recently shown a superior diagnostic capability to differentiate between all stages of diastolic dysfunction (114-116). However, all strain measurements have an inherent variability where the manual choice of segments on the chamber at which the strain-time history is extracted may vary from person to person. However, a combination of peak-VW and atrial strain as diagnostic metrics in the future would encompass the cardiac tissue-flow physics entirely and eliminate the need for any heuristic measures.

There are several potential limitations to our study. First, there is no ground-truth of diastolic function to use for validation of a new method. Second, we measured Peak-VW from a single beat, which means it does not account for any beat-to-beat variation. Third, the peak-VW calculation is not entirely agnostic yet as the correct time-step must be chosen for each scan before applying the continuous wavelet transform. Finally, we have assessed its clinical utility in a small, single-center cohort. Although our new measurement may appear to involve complex calculations, this was accomplished with a semi-automated algorithm. Thus, it is possible that this algorithm can be implemented online and become publicly available, offering the potential for diagnosing subclinical diastolic dysfunction with increased sensitivity.

2.6 Acknowledgements

This material was initially supported under a National Institutes of Health R21 Grant No. HL106276-01A1. The authors have no conflicts of interest to report. Dr Sayantan Bhattacharya is gratefully acknowledged for his help.

2.7 Appendix

Pseudo-Code

```
%%%%%%%%%%%%%%%%%%%%%%%%%%%%%%%%%%%%%%%%%%%%%%%%%%%%%%%%%%%%%%
%%%%%%%%%%%%%%%%%%%%%%%%%%%
% Matlab macro for computation of Wavelet propagation velocity from CMM   %
%   recordings                                                            %
% Authors: S. Chakraborty, P. Vlachos, Purdue University                 %
% Date: 10-October-2020                                                   %
%%%%%%%%%%%%%%%%%%%%%%%%%%%%%%%%%%%%%%%%%%%%%%%%%%%%%%%%%%%%%%
%%%%%%%%%%%%%%%%%%%%%%%%%%%
%
% This macro estimates the wavelet-based propagation velocity of the early
% diastolic filling wave. An input velocity field is analyzed, line by line
% between two time points by undergoing wavelet decomposition and cross
% spectrum evaluation. For each line pair, a group propagation velocity is
% obtain; the maximum propogation velocity during diastole is output.
%
% Pseudo Code
%   Input the CMM recording velocity "V"
%   Input the early diastole temporal index range "trng"
%   Input the full spatial index range "xrng"
%   Input the spatial resolution "dx" and temporal resolution "dt"
%   Input the wavelet cross spectrum threshold "thresh" (commonly 0.5)
%   Input the temporal step size "step"
%   Input the cutoff frequency "Fc"
%   Input the mother wavelet name "wname (user-specified; a suitable input
%       is the complex Morlet with an F-center of 2 and F-band of 0.5)
%
%   Construct the mother wavelet frequency range (length is commonly 100)
%   Compute the wavelet scales proportional to the inverse frequencies
%
%   Loop over all temporal indices
%       Compute the wavelet cross spectrum "WCS" from the current velocity
%           temporal index and an index advanced by the time step "step"
%       Construct the wavelet cross spectrum mask "wcs_mask" from the
%           normalized WCS "wcs_normalized" and threshold "wcs_threshold"
%       Evaluate the continuous wavelet transform energy spectrum "nrg"
%       Evaluate the median phase shift from the WCS "phase_shift"
%       Compute the wavespeed "computed_wavespeed" based on "phase_shift",
%           the 5 most dominant wavenumbers, and the temporal step size
%   End of loop
%
%   Truncate the wavespeed to keep early diastole measurements using "trng"
%   Retain the maximum wavespeed to obtain the Wavelet Propagation Velocity
%       estimate "Vw", the function output

function Vw = Wavelet_Vp(V,trng,xrng,dx,dt,thresh,step,Fc,wname)
[nX,nT] = size(V);                          % velocity map dimensions
freqRng = linspace(1/max(xrng),Fc/2,100)';  % wavelet frequency range
scales  = repmat(Fc./freqRng./dx,1,nX);     % wavelet scale range
computed_wavespeed =   zeros(nT,1); % Pre-allocate wavespeed storage
% Loop over each temporal index relative to step size
for k = 1:(nT-step)
    current_ind    = k + floor(step/2); % Current index plus half step size
```

```
    % Run wavelet cohorence to compute the Wavelet Cross Spectrum WCS
    % (wcoher is depreciated but still supported Matlab function)
    [~,WCS,CWT,~]  = wcoher(V(:,k),V(:,k+step),scales(:,1),wname);
    wcs_normalize  = WCS./(scales.^0.5);          % Normalize WCS
    wcs_threshold  = thresh*max(wcs_normalize(:)); % Estimate WCS threshold
    wcs_mask    = ones(size(WCS)); % Construct Wavelet Cross Spectrum mask
    wcs_mask(wcs_normalize <= wcs_threshold) = 0;
    nrg = trapz(xrng,abs(CWT.*wcs_mask).^2,2)./scales(:,1); % CWT energy
    phase_shift = -median(angle(WCS(wcs_mask == 1).^2)); % WCS phase shift
    [nrg,ind]   = sort(nrg,'descend'); % Sort CWT energy
    % Compute the wavespeed
    computed_wavespeed(current_ind) = phase_shift/...
        (2*pi*sum(nrg(1:5)/sum(nrg(1:5)).*freqRng(ind(1:5)))*(dt*step));
end
wavespeed_crop  = computed_wavespeed(trng); % Truncate wavespeed
% Cutoff to 2/3 early diastole duration
cutoff_time     =   floor(2/3*(trng(end)-trng(1)+1));
[Vw, ~]         =   max(wavespeed_crop(1:cutoff_time)); % Compute Vw
end
```

3. HEMODYNAMIC DEPENDENCE OF MECHANO-GENETIC EVOLUTION OF THE CARDIOVASCULAR SYSTEM IN JAPANESE MEDAKA

Authors: Sreyashi Chakraborty[1], Elizabeth Allmon[2], Maria S. Sepúlveda[3], Pavlos P. Vlachos[4]
1,4: Dept. of Mechanical Engineering, Purdue University
2,3: Dept. of Forestry & Natural Resources, Purdue University

3.1 Abstract

The progression of the cardiac gene expression-wall shear stress (WSS) interplay is critical to identify developmental defects during cardiovascular morphogenesis. However, mechano-genetics from the embryonic to larval stages are poorly understood in vertebrates. We quantify peak WSS in the heart and tail vessels of Japanese medaka from 3 days post fertilization (dpf) to 14 dpf using in-vivo micro particle image velocimetry (μPIV) flow measurements, and in parallel analyzed the expression of five cardiac genes (*fgf8, hoxb6b, bmp4, nkx2.5, smyd1*). Here, we report that WSS in the atrioventricular canal (AVC), ventricle outflow tract (OFT), and the caudal vessels in medaka peak with inflection points at 6 dpf and 10-11 dpf instead of a monotonic trend. Retrograde flows are captured at the AVC and OFT of the medaka heart for the first time. In addition, all genes were upregulated at 3 dpf and 7 dpf indicating a possible correlation between the two, with the cardiac gene upregulation preceding WSS increase in order to facilitate cardiac wall remodeling.

3.2 Introduction

Wall shear stress (WSS) fluctuations experienced by vascular endothelial cells and endocardial cells are linked with changes in cardiac specific gene expression and changes in cellular phenotypes (117-120) that modulate cardiovascular morphogenesis (121-124). The flow mechanics of the embryonic heart strongly influence the pulsatility and the topology of the peripheral vascular network (125-127). Chicken embryos (128-133) and small teleost models such as zebrafish (*Danio rerio*) and the Japanese medaka (*Oryzias latipes*) have been extensively imaged to capture non-intrusive, accurate flow velocity and WSS measurements at varying stages of cardiovascular development (134-141). The modulation of key genes responsible for cardiac anomalies in these species have previously been investigated by mutating genes, surgical

intervention or introducing perturbation in the blood circulation (129, 142-150). However, baseline longitudinal studies tracking the evolution of cardiovascular flow metrics and cardiovascular specific gene expressions at a 1dpf interval are scarce in the vertebrate embryogenesis literature (128, 129, 151, 152).

Cardiac valves located in the atrioventricular canal (AVC) and the outflow tract (OFT) of the ventricle experience the highest flow velocity and WSS (132-134, 153-155). The dynamic WSS variation in these regions control developmental landmarks like valve cushion formation, valve leaflet formation and direction during age progression (123, 133, 156-160). However, in two separate studies with zebrafish, peak WSS is shown to increase from 72 hours post fertilization (hpf) to 6 days post fertilization (dpf) at the AVC (155, 161) while the reverse trend is seen at the OFT (153, 162). Since both regions morphologically expand during chamber formation and subsequently undergo an area reduction after valve cushions form (163), opposite peak WSS trends in the AVC and OFT seem counterintuitive. Imaging intervals of 12 h or 24 h are too large for zebrafish which grow very fast with its ventricle length increasing at a rate of 125 µm/day during the first 60 dpf (164). Consequently, possible inflection points in peak WSS progression with age may have been missed in previous studies. Previous studies investigating aortic arch and cardiac outflow tract morphogenesis in chicken embryos have shown an inflection point in peak WSS progression (128, 129) with age that correlated with the expression of some developmental genes (129). Hence, in order to capture the cardiac developmental landmarks in more detail, we chose the Japanese medaka as the vertebrate model in the current study. Japanese medaka grows faster compared to higher mammalian vertebrate models (like mice, rabbits, pigs, humans) but is two times slower compared to zebrafish (164, 165). Additionally, the larger size and lack of pigmentation in medaka embryos until 14 dpf (165) when compared to zebrafish allows for better optical imaging. A comparison of the cardiac ontogeny in zebrafish and Japanese medaka can be found in the literature (164-166).

Multiple measurements of vascular WSS along caudal and dorsal vessels of larval teleosts have shown that arteries have higher pulsatility and flow velocities than veins. Owing to low velocity (~0.3-2 mm/s) of the cardiovascular flow in teleosts (127, 135, 167), the vascular WSS reported is low (5-30 dyne/cm^2) compared to humans and other vertebrates (140, 168-170). However, little attention has been given to the cross-sectional variation of these vessels from embryonic to larval stages that eventually separates them into arteries and veins (127, 171). The

vessel cross-section is critical in regulating flow velocities (127) which can subsequently lower the WSS below the critical value required for cell proliferation in vessels (172-175).

Calculation of WSS is non-trivial due to the difficulty in measuring spatially resolved velocity gradients near the cardiac wall. Velocity field in the fish heart can be measured non-invasively by using micro Particle Image Velocimetry (μPIV) that cross-correlates red blood cell (RBC) patterns in successive time-lapse images separated by a known time interval (161, 176-178). Velocity gradients of higher accuracy are then calculated from the spatially and temporally resolved velocity field instead of assuming a linear/parabolic velocity profile near the cardiac wall as done in previous studies (122, 124, 179).

Variations in blood viscosity with increasing shear rate and varying hematocrit in developing teleost embryos have rarely been accounted for (161, 180). Previous studies have assumed blood dynamic viscosity to be constant at all fish ages and used values ranging from 3cP to 8cP to calculate WSS in zebrafish heart (153, 155, 161, 181). A recent experimental investigation has shown the blood viscosity in embryonic zebrafish changes with time and hence should not be assumed to be fixed (180).

WSS induced mechano-transduction is known to influence embryonic cardiovascular development through the induction of late-onset genes (182-184). Molecular genetic approaches, such as qPCR, have been used with teleost embryos to identify molecular pathways and to study the functions of specific genes related to cardiovascular abnormalities/development. One well established genetic pathway in the growing zebrafish heart is activated in the AVC to control the atrio-ventricular (AV) valve morphogenesis. The Kruppel-like factor 2a (*klf2a*) gene responsible for this phenomenon is known to be expressed strongly in regions of high shear that impacts endocardial cushion differentiation leading to AV valve formation (121, 123, 126, 156). Fibroblast growth factor 8 (*fgf8*) and bone morphogenetic factor (*bmp4*) are cardiac genes required for development of teleost heart precursors (185, 186) and contribute to anterior heart field development in mouse (187). Homeobox B6b (*hoxb6b*) gene responsible for anterior/posterior patterning in the medaka was reported to disrupt morphogenesis in a toxic environment exposed to silver nanocolloids (188). NK2 transcription factor related 5 (*nkx2.5*) modulates the formation of the secondary heart field (189, 190) and was reported to peak between 48 hpf and 96 hpf in zebrafish embryos followed by a decrease at 120 hpf (148). Set-mynd-domain-1 (*smyd1*) gene

expression aids in cardiac muscle differentiation (186) and its knockdown in zebrafish results in disrupted myofibril growth and loss of a heartbeat (191).

This overview of the literature highlights the need for a baseline framework for vertebrate embryonic models that investigates variation of cardiovascular WSS with cardiac gene expressions along developmental stages. **In this work, we conducted a series of live experiments to image the Japanese medaka heart and peripheral vessels under a microscope followed by subsequent μPIV analysis for flow quantification along with gene expression profiling across development in embryo/larva in absence of any perturbation**. We report peak WSS measurements in two cardiac valve regions at the AVC and OFT. Concomitantly, we calculated peak WSS values in four vessel locations: dorsal artery (DA), dorsal vein (DV), caudal artery (CA) and caudal vein (CV) along the tail. We also performed qPCR analysis to compare gene expressions of five cardiac genes *fgf8, hoxb6b, nkx2.5, smyd1,* and *bmp4* in relation to peak WSS variation from 3 dpf to 14 dpf. To our knowledge, this is the first study with fish early life-stages that attempts to identify a correlation between the peak cardiac WSS variation and cardiac specific gene expression during development.

3.3 Results and Discussion

3.3.1 Cardiac function and geometry

The variation of cardiac function parameters and end-diastole ventricle area (A) with age progression of medaka is shown in **Figure 3-1**. The fish hatched between 8 dpf and 9 dpf in all cases. The HR increases from a mean value of 78.5 beats per minute (bpm) to 173.6 bpm with age progression and plateaus at 12-14 dpf in the larval stage (**Figure 3-1a**). The trend is similar to other vertebrates in utero (192, 193) but the range is different for each type of adult vertebrate (e.g., zebrafish: 120-180 bpm; human: 60-90 bpm; mouse: 300-600 bpm) (194). Reynolds number (Re) is defined as the ratio of inertial forces and viscous forces (195, 196). Wormersley number (Wo) is defined as the ratio of transient inertial forces and viscous forces (196). Both the Re and Wo are dimensionless, much less than 1 and increase with age within a small range [Re ~ 0.01-0.02; Wo ~ 0.02-0.04] (**Figure 3-1b** and **Figure 3-1c**). For higher vertebrates like humans, pigs and frogs the peak Re and peak Wo are much greater than 1 (195, 197, 198). For embryonic stages of chicks and mice they are in the same range as teleosts (133, 195). The end-diastolic area A in **Figure 3-1d**

increases from a mean value of 1143 μm^2 at 3 dpf to 4884 μm^2 at 14 dpf with age progression. The same trend is seen in all vertebrates but the size is larger for higher vertebrates (195). The ejection fraction (EF) does not show any monotonic trend across age progression (**Figure 3-1e**) but resembles the ventricle ejection fraction of humans (199). The EF spikes at 5 dpf but it goes down again and increases after hatching at 9 dpf and plateaus from 10-14 dpf. T is the time period of a heart cycle while t_{diast} is the time taken for the ventricle filling. The fractional time of ventricle diastole (t_{diast}/T) seen in **Figure 3-1f** initially increases from a mean value of 0.33 at 3 dpf to 0.41 up to 6 dpf and declines to 0.34 until 8 dpf. It remains constant (~ 0.3) until hatching and later declines to 0.21 at 13-14 dpf. In human fetuses the same trend of decreasing ventricle filling time with age is observed as heart rate increases from 90 bpm at 20 weeks to above 120 bpm at 40 weeks with isovolumic contraction time decreasing from 20% to ~0 % respectively (200, 201).

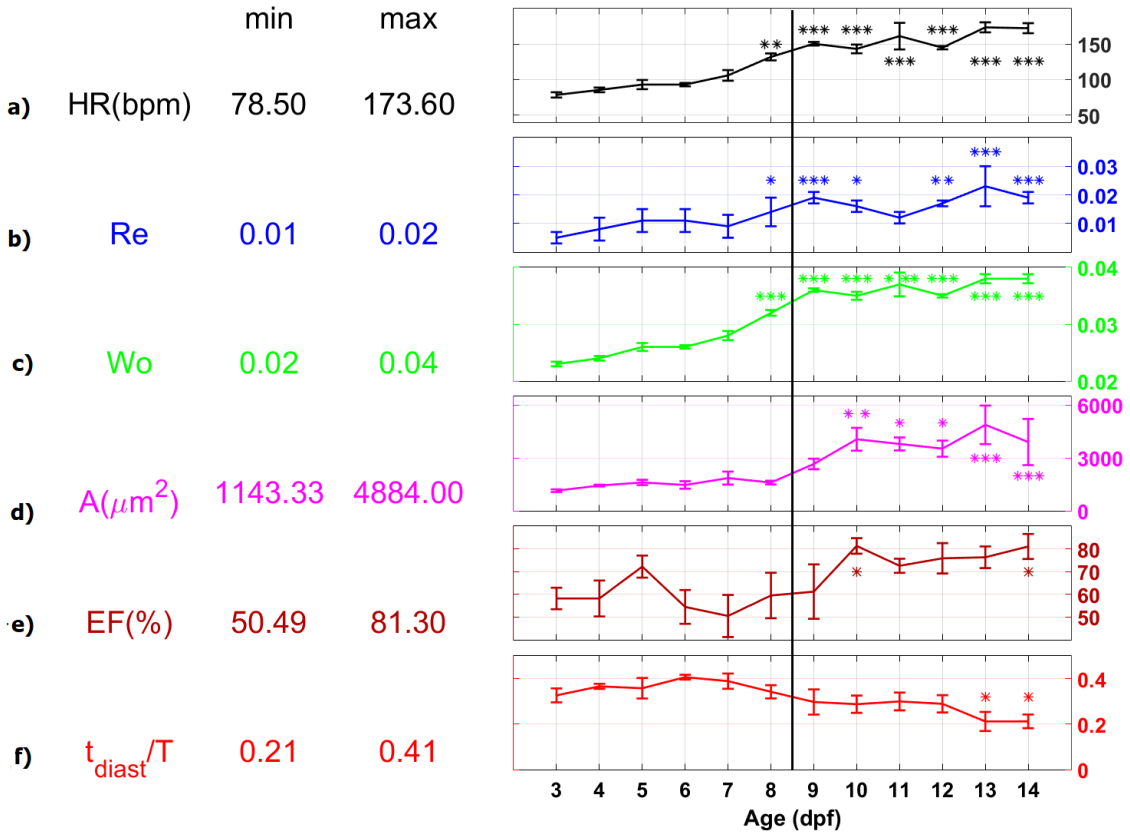

Figure 3-1: Variation of mean a) heart rate (HR), b) Reynolds number (Re) and c) Womersley number (Wo) at atrial inflow, d) end-diastolic ventricle area (A), e) ventricle ejection fraction (EF) and f) fractional ventricle diastolic time (t_{diast}/T) with medaka age progression (dpf). The black vertical line between 8 dpf and 9 dpf denotes hatching. Error bars ± SD. n=5 for each parameter at each dpf. Parameters were compared to 3 dpf values. * denotes $p < 0.0001$; ** denotes $p < 0.001$; * denotes $p < 0.05$.**

3.3.2 Hematocrit, viscosity and shear rate in the ventricle

The viscosity at each dpf is a function of both hematocrit and the shear rate. **Figure 3-2a** shows an initial increase in shear rate from 3 dpf (200 s^{-1}) to 5 dpf (332 s^{-1}) peaking at 6 dpf (1124 s^{-1}). It decreases to 491 s^{-1} at 7 dpf and then stays almost constant with little variations from 8 dpf (553 s^{-1}) to 14 dpf (497 s^{-1}). The hematocrit variation with time shown in **Figure 3-2b** depicts an increase from a mean value of 38.5% at 3 dpf to 48% at 6 dpf followed by a reduction to 35% at 8 dpf,

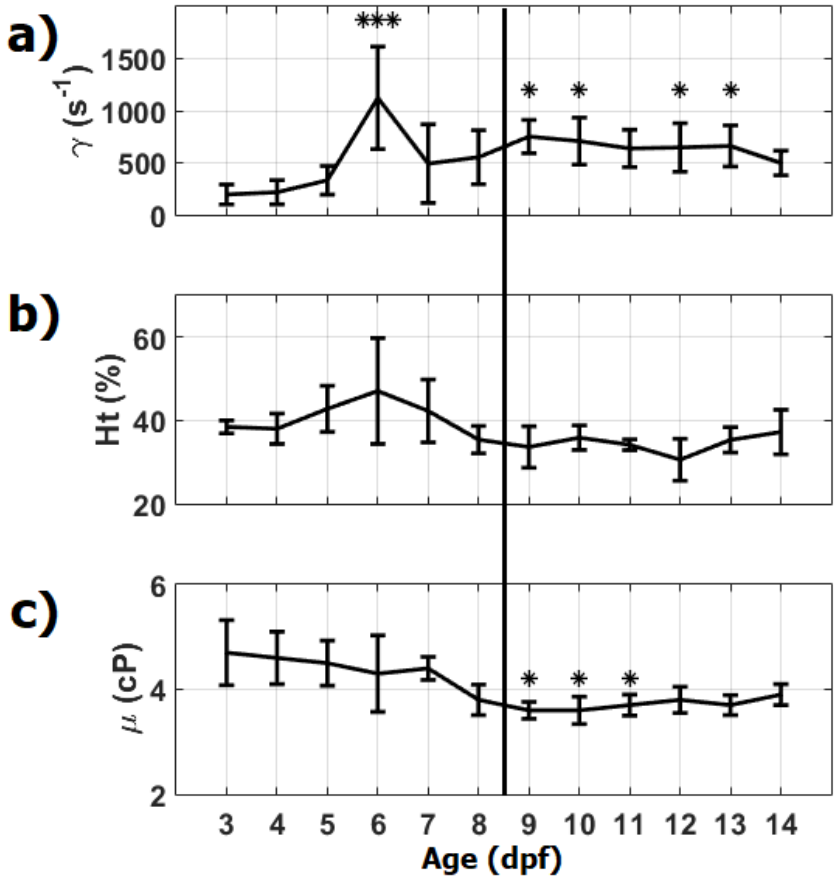

Figure 3-2: Variation of mean a) peak shear rate (γ), b) hematocrit (Ht) and c) blood dynamic viscosity (μ) in ventricle with medaka age progression (dpf). The black vertical line between 8 dpf and 9 dpf denotes hatching. n=5 for each parameter at each dpf. Error bars denote ± SD. Parameters were compared to 3 dpf values. * denotes $p < 0.05$.

remaining fairly constant around that value from 9 dpf (34%) to 14 dpf (37%). But none of these variations are statistically significant. The resultant mean viscosity shown in **Figure 3-2c** stays about the same from 3-7 dpf (4.3±0.2 cP) and then drops before hatching at 8 dpf and stays about the same value of 3.7±0.2 cP from 9-14 dpf. Although there is a statistically significant increase

in shear rate and a non-significant increase in mean hematocrit at 6 dpf, no substantial increase/decrease can be observed for the blood viscosity value at 6 dpf due to relatively low sample size (n=5) and high variability.

3.3.3 Spatial Velocity profile in AVC and OFT

Spatial variation of phase averaged streamwise velocity in the AVC during peak ventricle diastole and in OFT during peak ventricle systole are plotted in **Figure 3-3** at four ages of the growing medaka. The ventricle systole and diastole cover 2/3rd and 1/3rd of the heart cycle respectively. The profile is extracted at three times t1, t2 and t3 separated by 25 ms at 3 dpf, 6 dpf and by 20 ms at 9 dpf, 12 dpf. The velocity profile does not follow the parabolic shape due to low Re of the flow.

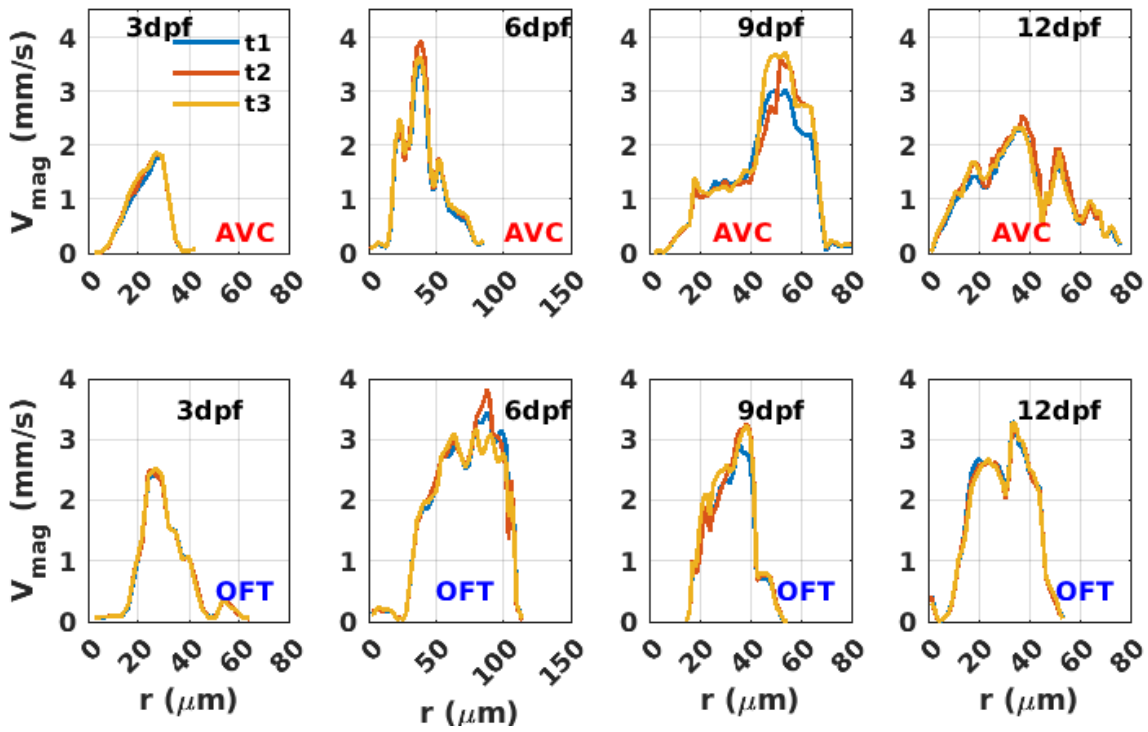

Figure 3-3 : Spatial Variation of phase averaged streamwise velocity in AVC and OFT of the medaka heart at three different times and at 3 dpf, 6 dpf, 9 dpf and 12 dpf. The profiles at each dpf are extracted at times t1, t2 and t3. The times occur during peak ventricle diastole for the top plots while it occurs during peak ventricle systole for the bottom plots. The time interval at 3 dpf and 6 dpf is 25 ms and at 9 dpf and 12 dpf is 20 ms. The x-limits for 6 dpf is different than the others because the measurement was taken from the ventricle side of the AVC and OFT which has a larger diameter. The other measurements were taken at the centre of the AVC and OFT which has a smaller diameter.

Instead, it follows a triangular profile at 3 dpf which changes into a flatter profile by 12 dpf. At 3 dpf, the peak OFT velocity (~2.6 mm/s) is higher than the peak AVC velocity (~1.8 mm/s). In later ages, the peak velocities in both regions fluctuate around 3 mm/s.

3.3.4 Velocity and WSS measurement in AVC and OFT

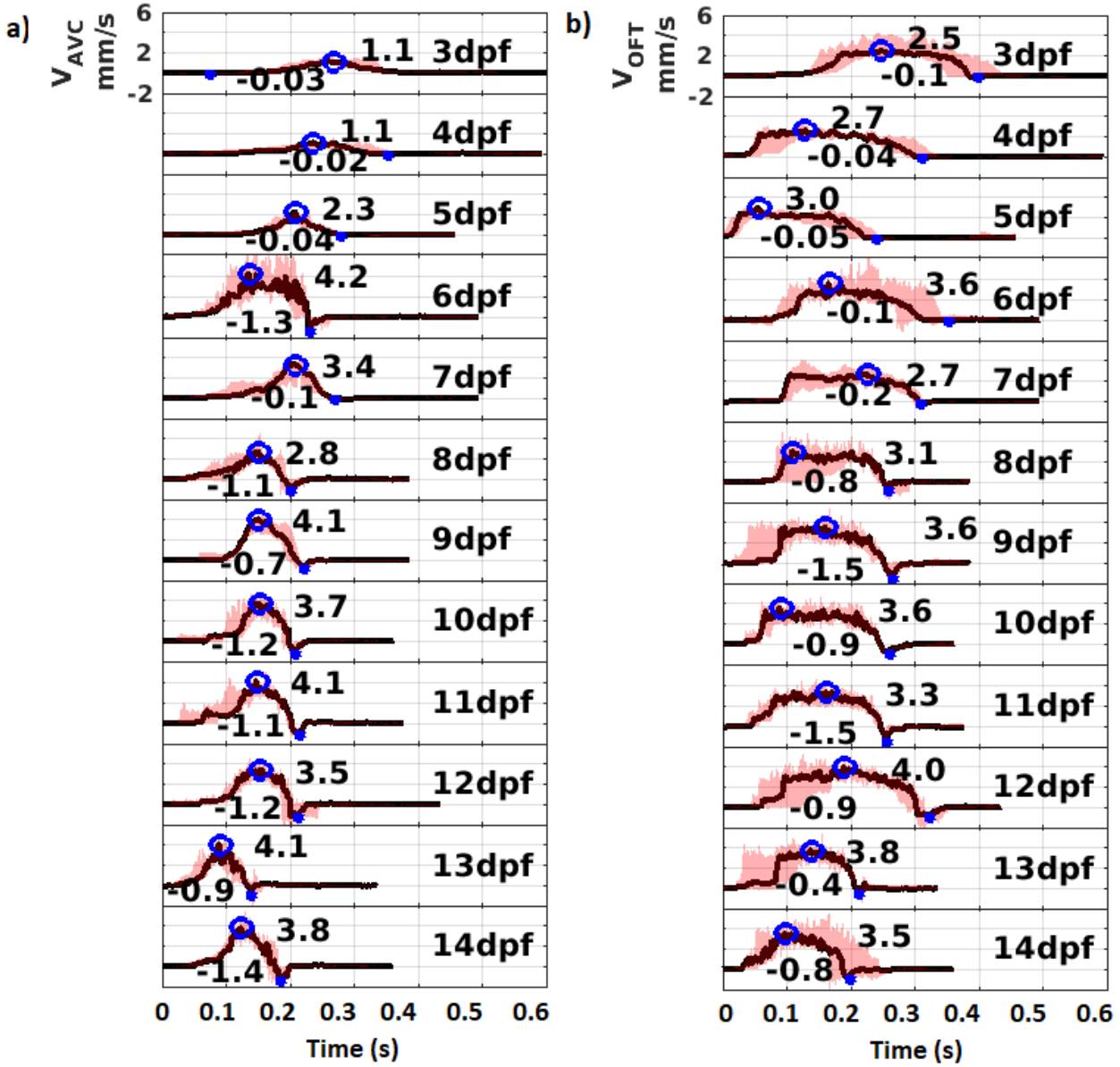

Figure 3-4: Time variation of velocity profiles in the a) atrioventricular canal (AVC) and b) ventricle outflow tract (OFT). Black lines denote the median profiles while the pink shade denotes the region between maximum and minimum profiles. The peak values of the median profile are marked on each plot by a blue circle and the minimum values on the median profile are marked by a blue star. n=5 for each dpf.

Velocity variation with an entire heart cycle in each dpf is plotted at the AVC and the OFT in **Figure 3-4**. The pink shaded region between the minimum and maximum time variations in each dpf depicts the bounds within which the profiles fluctuate. The median profile for each dpf is shown by the black line. The median peak velocity after the onset of circulation during 3 dpf at the OFT (**Figure 3-4b**: 2.5 mm/s) is substantially higher than that at the AVC (**Figure 3-4a**: 1.1 mm/s). The AVC peak stays the same at 4 dpf and increases at 5 dpf but the OFT (2.7-3.0 mm/s) still reports higher peak velocity magnitude than the AVC (1.1-2.3 mm/s). The median peak velocity values increase substantially at 6 dpf (AVC: 4.2 mm/s; OFT: 3.6 mm/s) and decrease progressively at 7 dpf (AVC: 3.4 mm/s; OFT: 2.7 mm/s). At 8 dpf peak AVC velocity decreases while the OFT peak velocity increases (AVC: 2.8 mm/s; OFT: 3.1 mm/s). After hatching, the median peak velocity values remain fairly constant from 9 dpf (AVC: 4.1 mm/s; OFT: 3.6 mm/s) to 14 dpf (AVC: 3.8 mm/s; OFT: 3.5 mm/s). At AVC, high median negative velocities observed from 6 dpf (-1.3 mm/s) till 14 dpf (-1.4 mm/s) denote presence of retrograde flow back into atrium at the end of ventricle diastole. After ventricular systole, initially a small negative velocity is observed at OFT during 3 dpf (-0.1 mm/s) which reduces considerably at 4dpf (-0.04 mm/s) and 5 dpf (-0.05 mm/s). It increases gradually at 6 dpf (-0.1 mm/s) and 7dpf (-0.2 mm/s). The negative velocity increases considerably at 8dpf (-0.8 mm/s). Post-hatch it fluctuates between -0.4 mm/s (13 dpf) to -1.5 mm/s (11 dpf) till 14 dpf (-0.8 mm/s).

WSS variation with an entire heart cycle in each dpf is plotted at the AVC and the OFT in **Figure 3-5**. The median peak WSS values (**Figure 3-5a** and Figure 3-5**b)** reflect the combined effect of changing blood viscosity and shear rate at each time point. Similar to the peak velocity variation with time, the median peak WSS peaks at 6 dpf (AVC: 47 dyne/cm^2; OFT: 34.4 dyne/cm^2), declines at 7 dpf (AVC: 17 dyne/cm^2; OFT: 19.8 dyne/cm^2) and increases again at 8 dpf (AVC: 23.8 dyne/cm^2; OFT: 24.4 dyne/cm^2), continues increasing after hatching and fluctuates around a small range of values from 9 dpf (AVC: 33.6 dyne/cm^2; OFT: 30.4 dyne/cm^2) to 14 dpf (AVC: 26.7 dyne/cm^2; OFT: 22 dyne/cm^2). Retrograde flow at AVC and OFT is evident from high median negative WSS magnitudes from 6dpf (AVC: -17.5 dyne/cm^2; OFT: -1.9 dyne/cm^2) till 14 dpf (AVC: -4.3 dyne/cm^2; OFT: -2.7 dyne/cm^2).

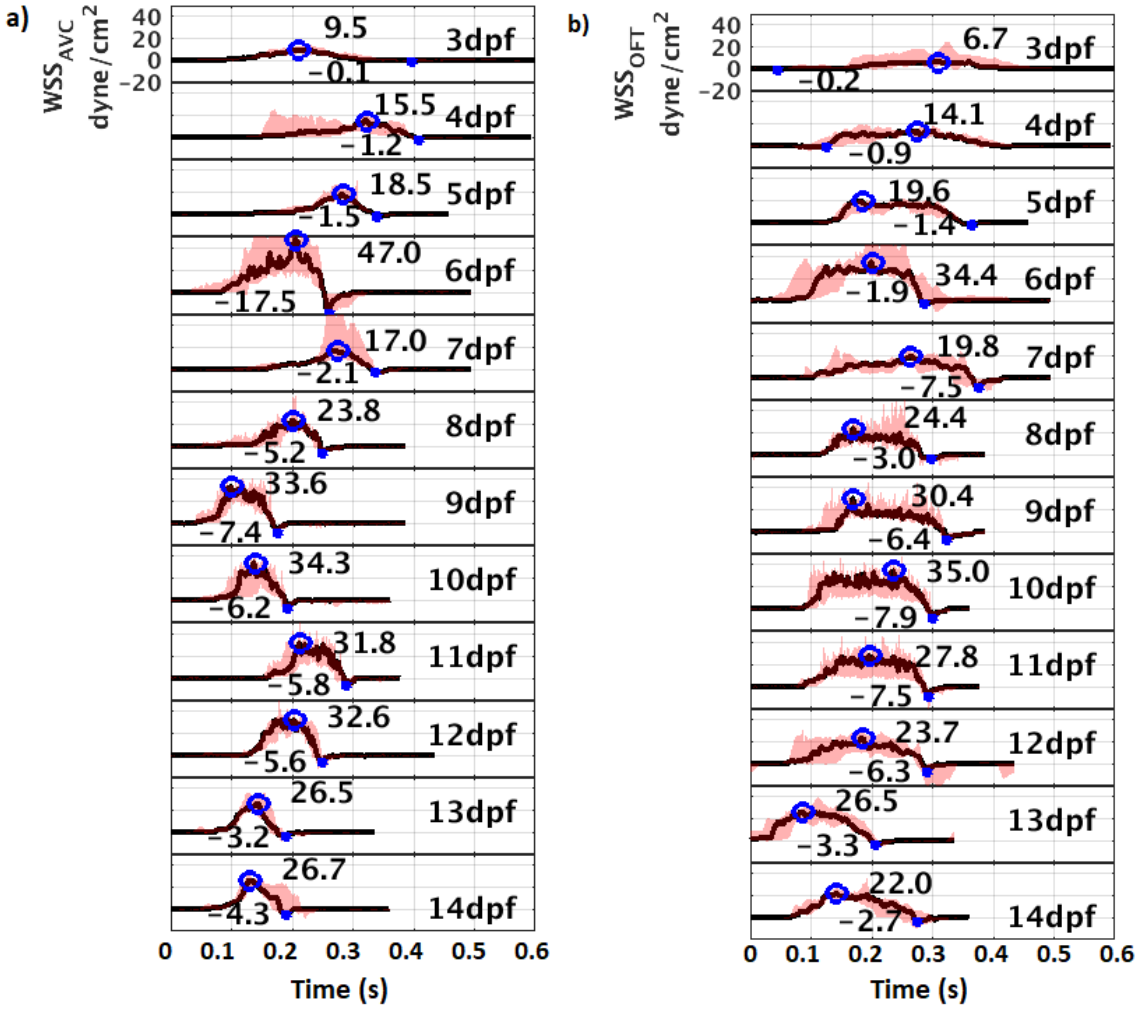

Figure 3-5: Time variation of WSS profiles in the a) atrioventricular canal (AVC) and b) ventricle outflow tract (OFT). Black lines denote the median profiles while the pink shade denotes region between maximum and minimum profiles. The peak values of the median profile are marked on each plot by a blue circle and the minimum values on the median profile are marked by a blue star. n=5 for each dpf.

3.3.5 Area, velocity and WSS measurement in tail vessels

The caudal vessels and dorsal vessels undergo reduction in their cross-sectional areas as fish develop (**Figure 3-6**). In the embryonic stage (3-8 dpf), the dorsal vessels could not be imaged and hence **Figure 3-6a** shows the area reduction of the caudal vessels from 3 dpf to 7 dpf. The veins and arteries are not differentiated at 3 dpf (633.1 μm^2) and 4 dpf (459.7 μm^2) as evident from the similar mean cross-sectional areas. From 5 dpf (CV: 411.7 μm^2; CA: 213.7 μm^2) to 7 dpf (CV: 373.1 μm^2; CA: 145.2 μm^2) the caudal artery reduces faster in area than the caudal vein. At 8 dpf, as the embryo prepares to hatch by decompressing, the areas increase slightly (CV: 475.1 μm^2;

CA: 169.6 μm^2). In **Figure 3-6b** the caudal vessels continue to decrease in cross-section from 9 dpf (CV: 452.2 μm^2; CA: 169.6 μm^2) to 14 dpf (CV: 248.7 μm^2; CA: 80.1 μm^2). The DA and DV that are located upstream of the CA and CV respectively depict the same trend of area variation with cross-section but interestingly at each time point the dorsal vessel areas are larger than the caudal vessel areas (**Figure 3-6b**).

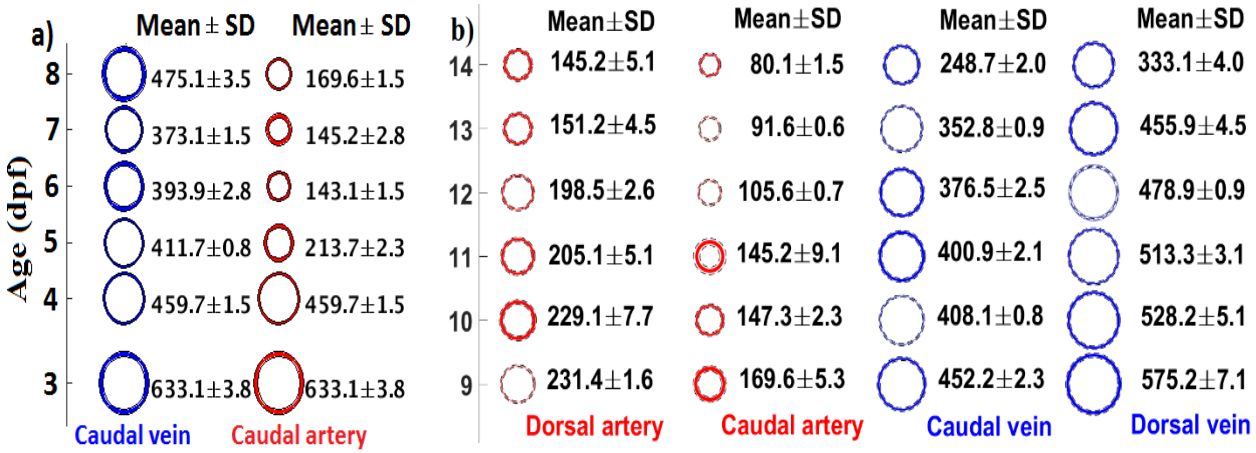

Figure 3-6: Variation of tail vessel cross-sectional area (μm2) with fish age progression (dpf). a) Caudal vein and caudal artery variation are captured from 3 dpf to 8 dpf. b) Dorsal artery (DA), caudal artery (CA), caudal vein (CV), and dorsal vein (DV) area variation is captured from 9 dpf to 14 dpf. n=5 for each dpf.

The velocity and WSS variation in the vessels over time reflects the effect of vessel area variation with time (**Figure 3-7**). The pulsatility in the veins are dampened faster over time than the arteries. After hatching, a time-dependent flow continues in the CA while the CV exhibits steady flow. The peak velocity magnitude remains the similar for both CA and CV from 3-5 dpf (**Figure 3-7a**). The peak WSS at 5 dpf is slightly higher for the CA than the CV but similar at 3 dpf and 4 dpf (**Figure 3-7b**). At 6 dpf, both the peak velocity and peak WSS magnitude of the CA increase considerably declining at 7 dpf and increasing slightly at 8 dpf. This increase in velocity corresponds to the increase in cross-sectional area of the CA. Interestingly, the peak velocity and peak WSS of the CV progressively decreases from 6-8 dpf as it undergoes a less drastic change in cross-section. After hatching the velocity and WSS of the DA and DV are higher than the CA and CV respectively (the difference is greater for the arteries at 9 dpf and 12 dpf). There is no trend in the variation of peak values from 11-14 dpf. It is interesting to note that the arterial flows are subjected to low WSS during most of the cycle from 3-8 dpf even though peak values are higher.

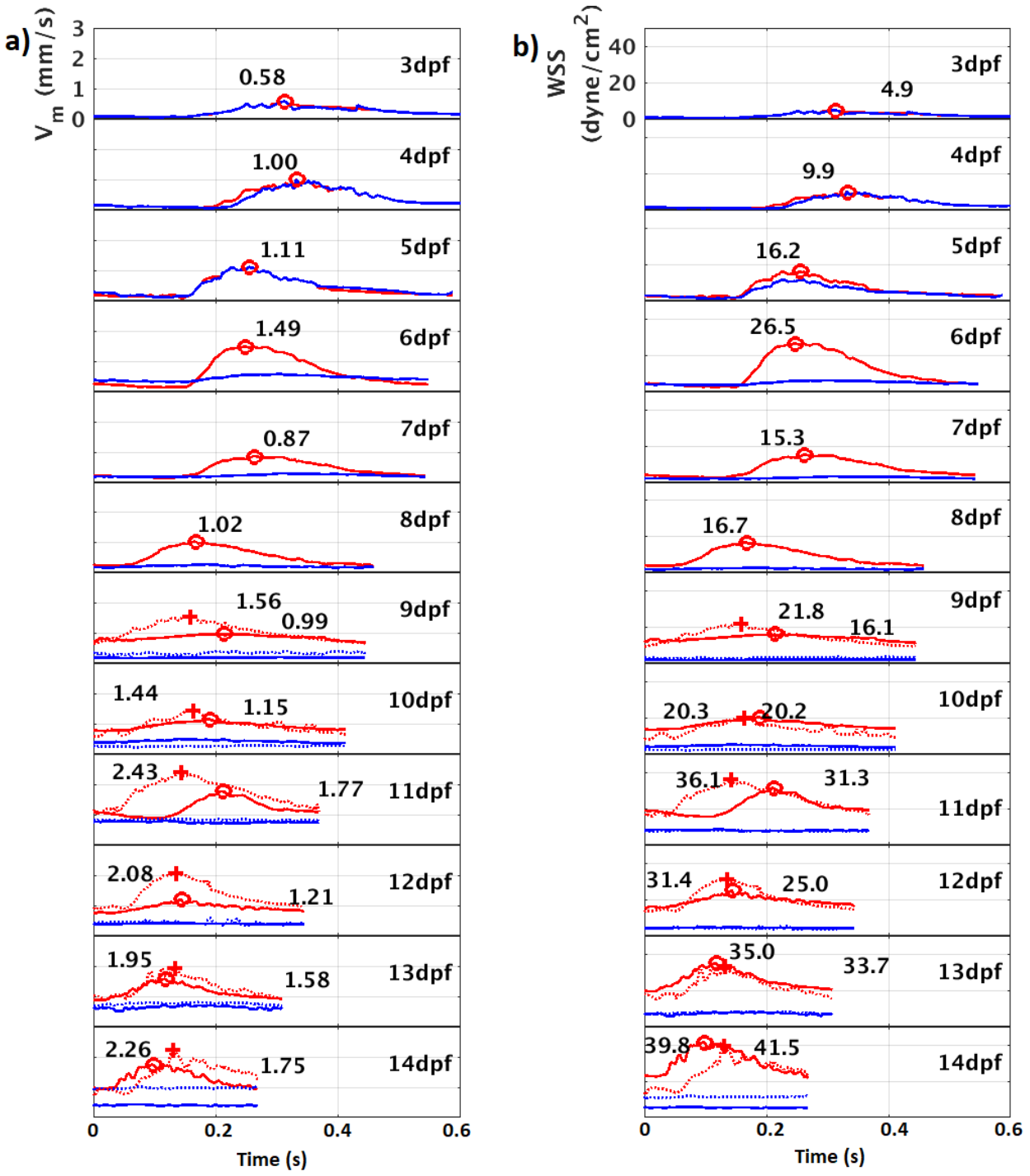

Figure 3-7: Time variation of a) velocity and b) WSS profiles in the tail vessels. Red lines denote arterial profiles while the blue lines denote venous profiles. Dotted curves correspond to dorsal vessels and solid curves correspond to caudal vessels. From 9 dpf to 14 dpf the red '+' markers correspond to the peak magnitude in dorsal artery while the red 'o' markers correspond to the peak magnitude in caudal artery. n=5 for each dpf.

WSS values <10 dynes/cm^2 for unsteady flows and WSS values < 1 dynes/cm^2 for steady flows are known to cause cell proliferation and vascular remodeling along endothelial layers of the vasculature (174). Post-hatch the baseline WSS in the CA and DA at each time point is at least 15 dynes/cm^2 that indicate stable flow-structure dynamics in the tail vessels.

3.3.6 Gene expressions from qRT-PCR analysis

The variation of five cardiac specific genes (*fgf8, hoxb6b, nkx2.5, bmp4, smyd1*) across time are plotted in . Statistical significance between each pair of dpfs was compared for a specific gene (**Table 3-5** in Statistical Analysis). A sequentially varying control was chosen for these tests instead of a fixed control due to absence of a baseline cardiac event occurring at a fixed dpf. For each gene plot, days not connected by the same letter are significantly different. At 0.5 dpf, there is a spike in the expression of *smyd1*, *hoxb6b* and *nkx2.5* that may be attributed to the maternal influences on the embryo (202-204). Expression for all genes spikes at 3 dpf and then again at 7 dpf. This spike is statistically significantly different from the gene expressions in preceding 6 dpf for *smyd1*, *fgf8, hoxb6b* genes and from the following 8 dpf for the *hoxb6b* gene.

3.3.7 Correlation between peak WSS and gene expression along fish age progression

Peak WSS was non-invasively quantified in the heart and tail vessels of the embryonic and larval medaka and compared with the expressions of five cardiac genes (**Figure 3-8**). **Figure 3-8a** shows the expressions of five cardiac genes. The *smyd1, hoxb6b, nkx2.5* genes spike at 0.5 dpf. *Smyd1* has only one sample at 0.5 dpf. All of them increase significantly at 3 dpf and 7 dpf. At 0.5 dpf upregulation of three genes can likely be attributed to maternal influences (202-205). Both the WSS-AVC and WSS-OFT increase significantly at 6 dpf compared to 3 dpf (**Figure 3-8b**). They exhibit an inflection trend around 6dpf-7dpf and ultimately plateaus from 9 dpf to 14 dpf.

Figure 3-8c compares the peak WSS in tail vessels (CA, DA, CV and DV) varying with time. The CV peak WSS follows the trend in CA until 5 dpf, before decreasing and eventually plateauing between 7 dpf and 14 dpf. The peak WSS is similar in magnitude at both DV and CV after hatching. The peak WSS in CA displays the same trend as that in AVC and OFT from 3-8 dpf.

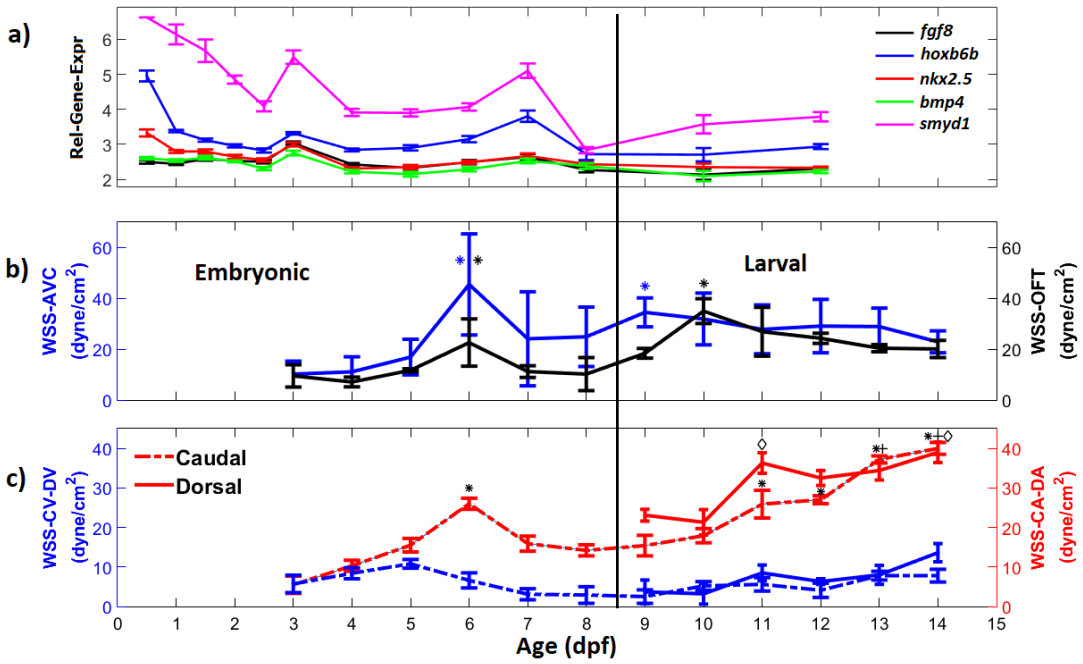

Figure 3-8: Correlation of relative gene expressions and peak WSS variation in heart and tail vessels with fish age progression (dpf). The * in the middle and bottom plots denote statistical significance compared to the control values in 3 dpf. In the bottom plot, the diamond denotes statistical significance compared to control values in 9 dpf for Dorsal Aorta (DA) and the + denotes statistical significance compared to control values in 9 dpf for Caudal Aorta (CA). $p<0.05$ was considered statistically significant.

Post-hatch, the peak WSS continues to increase (owing to the progressive reduction in vessel cross-section with time) in both DA and CA. The WSS is higher in DA than in CA from 9-12 dpf but is same at 13-14 dpf. Summarizing the trends in **Figure 3-8**, we observe that gene expression spikes at 3 dpf and 7 dpf are followed by an increase in peak WSS in ventricle inflow (AVC), outflow (OFT) and the tail CA at 6 dpf and 10-11 dpf respectively.

3.3.8 Effect of WSS magnitude and retrograde flow on cardiac landmarks along fish age progression

Previous research in zebrafish have shown the importance of shear forces in cardiac tissue remodeling (122) at each stage of its cardiac development (136, 156, 161, 181, 206, 207). Unfortunately for medaka, there is little in-depth study that clearly demarcates onset of cellular processes like endothelial to mesenchymal transition (EMT), trabeculation formation and valve formation in absence of perturbation. So, we compare cardiac events of medaka with zebrafish in **Table 3-1** and assume similar cellular mechanisms regulate cardiac development in both species.

A linear heart tube is seen from 3 dpf to 5 dpf where low velocity pulsatile flows occur in a single direction. There is no sharp demarcation between atrium and ventricle yet. Lower WSS (133) in these stages (**Figure 3-5**) with concomitant cardiac looping cause formation of trabeculation (126, 208-210) although it is not evident from the images. Large WSS values as observed at 6 dpf are known to promote expansion of extracellular matrix and EMT that leads to invagination of cardiac cells (152). Endocardial cushion formation due to invagination of endocardial cells previously seen in the AVC region of zebrafish (206, 211) narrows the valvular area leading to an increase in the wall velocity gradient and the peak WSS at 6 dpf. A similar trend of inflection for the peak WSS in the OFT and aortic arch was previously reported during cardiac development of chick embryos (128, 129). The AVC formation in zebrafish depends on retrograde flows more than on the magnitude of WSS (121, 123). A weak retrograde flow is observed in the medaka AVC and OFT (**Figure 3-4**) at 3 dpf, 4 dpf and 5 dpf which maybe within measurement error. The retrograde flow WSS increases considerably at AVC during 6 dpf and at OFT during 7dpf. With concentric chamber growth in the following time points (7 dpf-8 dpf), the AVC and OFT regions expand further due to which the peak WSS reduces. After hatching, the pericardium continues to thicken thereby narrowing the AVC and OFT further. There are no valve leaflets formed as evident from the moderate retrograde flows from 9 dpf to 14 dpf (**Figure 3-5, Figure 3-5**).

Table 3-1: Comparison of cardiac development times in zebrafish and japanese medaka

Cardiac Event	Bilateral Heart Formation	Heart Tube Beating	Onset of Chamber Formation	Onset of Cardiac Looping	Cushions start forming	Onset of Concentric Chamber Growth	Pericardial cavity formation	References
Zebrafish	18 hpf	22 hpf	30 hpf	36 hpf	56 hpf	64 hpf	96 hpf	(137, 148, 153, 154, 164, 166, 206, 207)
Medaka	38 hpf	44 hpf	54 hpf	64 hpf	120 hpf	120 hpf	168 hpf	(165, 166, 212)

3.3.9 Relation of gene expression with cardiac landmarks along fish age progression

The embryonic medaka heart dynamically develops from a linear tube to chambered heart with valve cushions at inflow and outflow of chambers. Different feedback loops between flow induced

forces and gene expressions impact cellular rearrangement throughout cardiac morphogenesis. The *fgf8* gene required for signaling the development of cardiac precursors spike at 3 dpf during second phase of cardiomyocyte differentiation that is known to form outflow tract at the arterial pole of the ventricle (186, 213). Both *nkx2.5* and *bmp4* are markers of early heart development (214) and therefore spike at 3 dpf. *Bmp4* strongly influences the cardiac left-right axis alignment leading to early cardiac patterning (215). The *smyd1* peak expression at 3 dpf aids in cardiac muscle differentiation and contraction by regulating the myofibril organization (186, 191). The *hox6b6* gene expresses at 3 dpf during anterior/posterior patterning in early cardiac morphogenesis (188). The extent of flexion in the atrioventricular region is maximum during 6dpf to 7dpf (186). All gene expressions showing a second peak at 7dpf could be a manifestation of this cardiac event.

3.3.10 Relation of Cardiac flow with Vascular flow along fish age progression

Viscous forces and changing wall boundaries are the catalysts for the cardiovascular development in teleost embryos. Unlike cardio vasculature in higher vertebrates, flow rates are so small in growing medaka (Re <<1) that there is no inertial contribution to facilitate morphological changes. The medaka heart starts pulsating at stage 24 (1 day 20 h) and a primitive vascular network is present (165, 171). At 2days 2 hr the valveless heart behaves like an impedance pump (126, 216) and pushes the blood at 78.5±2 beats per minute into the vasculature. The caudal artery and vein have same diameters in this stage and exhibit the same low flow velocities (0.58 mm/s) with high pulsatility. The low vascular WSS values (<10 dynes/cm^2) in conjunction with chemical stimuli are known to cause red blood cell agglomeration and perfusion that leads to self-angiogenesis (217-219). The vascular feedback around 5 dpf causes a prominent cardiac looping in the heart. Due to this, the chambers are separated by well-defined narrow valveless regions that alters the pulsatility rate and mechanism (126). The increased pulsatility drives higher flow velocities into the vasculature from 5 dpf to 8 dpf. The vessel diameters reduce to accommodate the altered flow within a compressed embryo (127). The vessels returning blood to the heart (CV) suffers less diameter reduction than the ones carrying from it (CA). During hatching from 8 dpf to 9 dpf, the caudal vessels mildly increase in cross-section owing to decompression. The vessel cross-section reduction from 9 dpf to 14 dpf is also evident along its axial location on the tail (from DA to CA). At these stages, the heart has well-defined chambers surrounded by a visibly thick pericardium. The OFT and dorsal aorta act as capacitors downstream of the cardiac flow that dampens the flow

pulsatility in vessels that are farthest from the heart (125, 126). The topology of the vasculature like vessel curvature, bifurcations and network organizations dynamically alter mechanical cues that regulate perfusion throughout the cardiovascular system. Investigating all types of stimuli (chemical, electrical, topological, cellular) and their inter-relationships in a developing cardiovascular system is beyond the scope of this study. Instead, it highlights for the first time, the occurrence of peak vascular WSS in CA concomitant to the cardiac AVC and OFT WSS peaks at 6 dpf signaling a major cardiac event when cardiac looping, chamber ballooning and expansion takes place **(Figure 3-8)**

3.4 Conclusion

To our knowledge, this work is the first to report peak WSS values in the AVC and OFT of a developing Japanese medaka from 3 dpf (onset of blood circulation) to 14 dpf. The influence of the cardiac flow on the vascular geometry and WSS downstream were concomitantly explored. Flow reversals are seen for the first time in the valveless narrow cushion regions of the medaka ventricle inflow and outflow. This type of longitudinal study over a significant period of cardiovascular development relating the WSS to gene-expressions is scarce in all vertebrates. Contrary to intuition, the tail vessels experienced a reduction in cross-sectional area with age progression. Caudal vessels that are further away from the heart underwent a greater reduction than the dorsal vessels. The salient feature that stood out from the longitudinal analysis of peak-WSS variation with age is the existence of inflection points instead of a monotonic trend. These inflection points in WSS are preceded by inflection in the expression of cardiac genes at earlier time points. The temporal expressions of these genes correspond with important developmental landmarks in the cardiac morphogenesis like valve area formation, chamber looping, and chamber growth. Thus, identification of these unique trends in the mechano-genetic tapestry of a developing cardiovascular teleost model will provide a baseline framework for future studies that can test causality between gene expression and WSS variations. This baseline framework can be validated by exposing the medaka to cardiotoxic environments. The validated framework can be tested by probing the mechano-genetic evolution in higher vertebrate models. Once the mechano-genetic correlation is established, clinical trials on humans can improve the diagnostic capability and assess the sensitivity of the cardiac tissue damage.

3.5 Author contributions

All authors, SC, EA, MSS and PPV contributed to the conception, and design of the study, SC did all data collection and data analysis, and EA did the gene expression analysis. All authors, SC, EA, MSS and PPV, contributed to the interpretation of the results and the writing of the paper.

3.6 Methods

All methods were carried in accordance with relevant guidelines and regulations and method protocols have been approved by the Purdue Animal Care and Use Committee (PACUC).

3.6.1 Japanese Medaka husbandry and embryo collection

Wild type adult Japanese medaka (20 male-female pairs) obtained from USEPA, Duluth, MN, USA were mated in 2L transparent tanks with continuous oxygen supply under artificial reproductive conditions (14:10; Light:Dark cycle; 26-28^{o}C). The fish spawned eggs every day at 9 am in the morning and eggs were fertilized by 5 pm in the evening. The fertilized eggs were collected, immersed in embryo medium (diluted saline solution containing 2 ppm methylene blue) and stored in an environment chamber at 28^{o}C. Imaging was performed after the onset of blood circulation in the embryos at 3 dpf.

3.6.2 Fish Selection for Imaging and gene expression

A total of 150 fertilized eggs were collected and five embryos/larvae (n=5) were imaged each day starting at 3 dpf until 12 dpf. On average, hatching occurred between 8-9 dpf. Embryos were collected from the population by random sampling. Between 0.5 dpf and 3 dpf ten embryos (n=10) were flash frozen every 12 hours for gene expression. Between 3 dpf and 12 dpf the sampling interval was reduced to once per day. The more frequent sampling interval during early embryonic development was chosen to capture the possible rapid changes in the cardiac development induced gene expression.

3.6.3 Data Acquisition

Images of medaka fish heart and caudal vessels were collected from animals ranging from 3 to 8 dpf (n=5 at all time points). They were visualized through a Nikon-Ti microscope with a 60x objective lens and acquired by a high-speed CMOS camera (Phantom Miro-310, 2500x1600 pixels) which resulted in an effective pixel size of 0.16 µm. Brightfield time-resolved images were captured for 4s at a rate of 400 frames per second. These correspond to 8-10 cycles and around 199 image pairs per cycle.

3.6.4 Flow velocity analysis in heart

Signal amplification of raw images

The raw images (**Figure 3-11a**) were preprocessed by applying a proper orthogonal decomposition (220-223) across time series of images and retaining the non-dominant modes that represent the fluctuations of RBC patterns across time (**Figure 3-11b**). This step substantially removed the background artifacts. The RBC movement patterns across time lapse images were cross-correlated and a phase average of the cross-correlations were used to obtain velocities in the heart and vessels as shown in **Figure 3-11c**.

Heart function measurement

The HR was measured from the Fourier transform of the instantaneous velocity waveforms. The Reynolds number ($Re = \frac{\rho V d}{\mu}$) and Womersley number ($Wo = d\sqrt{\frac{\rho\omega}{\mu}}$) were calculated for each sample and each age based on the atrial inlet diameter (d), blood density (ρ) as 1025 kg/m^3, blood dynamic viscosities (μ) that change with dpf and $\omega = 2\pi HR/60$. The EF is a function of ventricle volumes at diastole and systole. It is defined in Equation 3-1. Lis the length of the ventricle and D_1, D_2 are breadth and depth of the ventricle respectively.

$$A = \pi L D_1;\ Vol = \frac{\pi}{4} L D_1 D_2;\ D_1 = D_2;$$

$$\mathrm{EF} = \frac{End\_diastolic\_Vol - End\_systolic\_Vol}{End\_diastolic\_Vol}$$

Equation 3-1

3.6.5 µPIV analysis

The instantaneous velocity field at a time point in the heart cycle was obtained from the standard cross correlation (SCC) of two successive image pairs as mentioned previously (224). Each image region is subdivided into windows before cross-correlating. Cross-correlation vectors were obtained using an initial window size of 96x96 pixels (window resolution : 48x48 pixels) with a 50% overlap between windows, followed by another pass of window size of 64x64 pixels (window resolution : 32x32 pixels) with 50% overlap and finally followed by another pass of window size of 64x64 pixels (window resolution : 32x32 pixels) with 75% overlap (225). Each window in each image in the first pass, second and third pass has roughly 10-15 RBC patterns, 6-8 RBC patterns, and 5-7 RBC patterns respectively. In each pass there were minimum 3 and maximum 6 iterations of window deformation weighted by a Blackman filter that minimized the loss of information due to in-plane motion of the particles (226, 227). **The correlation planes at each phase of the cycle were averaged across all cycles to get an ensemble correlation plane (228).** The peak location of the correlation plane denotes the displacement between images at that time point. An accurate velocity estimate at each cycle phase is obtained by fitting sub-pixel resolution curves to the correlation peak using a three point Gaussian estimator (224, 229).

The spatial resolution of the final phase averaged velocity map is 1.28 µm for 60x images and 2 µm for 40x images. The temporal resolution is 2ms. No temporal or spatial averaging was done to the velocity measurements since the peak flow in the AVC, OFT and the vessels (specially arteries) were changing very rapidly across time and space. Universal outlier detection was done in between passes to get rid of erroneous velocity vectors (230). An additional median filtering with a window size of 3x3 pixels spatially was done to the vectors in the final pass (117, 231). All the calculation steps are done using the in-house PIV software, PRANA (232).

Velocity measurement location in medaka

Figure 3-9a shows the side view of a larval medaka of age 14 dpf where the location of heart, dorsal vessels and caudal vessels are highlighted. The AVC and OFT regions are represented by a red rectangle and a green rectangle respectively in parts b), c) and d). In **Figure 3-9b**, a schematic of the linear heart tube during 3 dpf to 5 dpf is shown. The AVC region is wider than the OFT region. The atrio-ventricular flexion at the end of cardiac looping has moved atrium and ventricle

in different planes in **Figure 3-9c**. The AVC is narrower than the OFT in this stage from 6 dpf to 8 dpf. In **Figure 3-9d** both AVC and OFT has further reduced in cross-section while the atrium and ventricle have grown in size.

3.6.6 WSS analysis in AVC and OFT

Wall position calculation

Endocardial wall boundaries were detected from the velocity contour maps by identification of edges where the velocity gradient is maximum. **Figure 3-10a** shows a signal amplified image of flow through OFT in a 14 dpf medaka heart. OFT connects the two heart chambers ventricle (V) and bulbus arteriosus (BA) during ventricle systole. A 4-level Otsu thresholding method was initially applied to the velocity map to create a mask around the OFT. The Prewitt edge detection

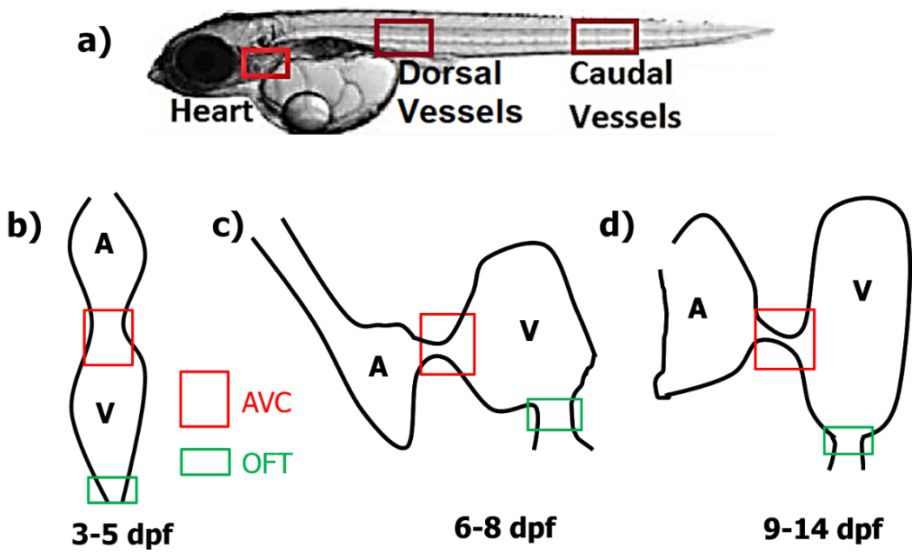

Figure 3-9: Location of heart and vessels in medaka and schematic diagram of medaka heart at different ages. (a) Location of heart, dorsal vessels and caudal vessels when viewed from the side in a larval medaka (age 14 dpf). Location of AVC and OFT in a schematic medaka heart during (b) 3 dpf to 5 dpf, (c) 6 dpf to 8 dpf and (d) 9 dpf to 14 dpf. "A" represents atrium and "V" represents ventricle. Red rectangle represents location of measurement at AVC and green rectangle represents location of measurement at OFT.

algorithm was used to find the wall locations (shown by circles in **Figure 3-10c**) based on the maximum intensity gradient locations of the phase averaged velocity map. Color of velocity vectors near OFT walls (**Figure 3-10b**) display the high positive and negative gradients in those regions. This method is similar to the one applied previously for wall detection in a zebrafish heart

(154). The error is difficult to quantify since there is no gold standard to compare against. A manual identification of wall positions lacks repeatability and do not guarantee accuracy. On the other hand, this signal-based wall location determination assures repeatability.

WSS calculation

WSS is a product of the fluid dynamic viscosity (μ) and the flow shear rate (γ) at the wall location (μ is the flow dynamic viscosity) [Equation 3-2].

$$WSS = [\mu\gamma]_{walllocation}$$ **Equation 3-2**

Blood dynamic viscosity in teleosts is ill-defined. We modelled the medaka heart blood viscosity as a function of both hematocrit (Ht) and wall shear rate (γ) according to the Walburn-Schneck equation as shown in (233). Velocity gradients were calculated using a high accuracy gradient calculation technique namely the Compact-Richardson method (234) in accordance to second

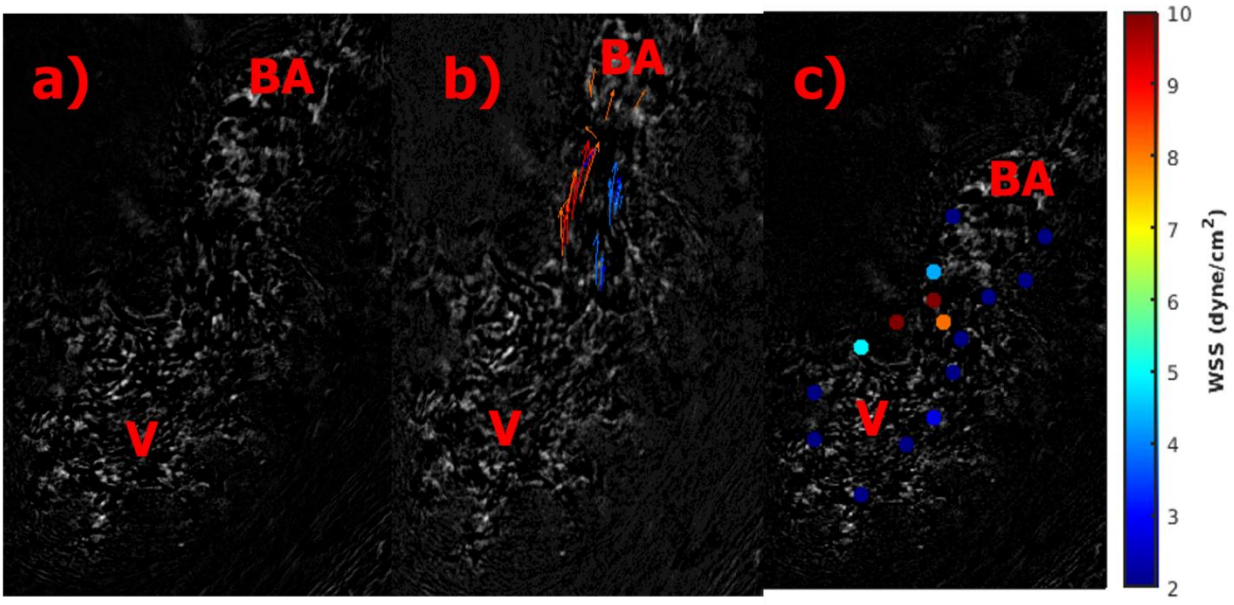

Figure 3-10: Edge detection of the endocardial wall based on intensity gradients. a) Signal amplified image of flow through OFT b) Velocity vectors at the OFT walls with the color displaying high positive and negative intensity gradients c) Endocardial wall positions (circles colored by WSS magnitude) detected by edge detection of high intensity gradients. Images were taken from a 14 dpf medaka heart. V represents ventricle and BA stands for bulbus arteriosus.

order polynomial fitting done in previous studies (154, 161). Shear rate (γ) at the AVC and OFT were derived from the velocity gradient field using the following Equation 3-3.

$$\gamma = \frac{d\vec{V}}{d\vec{n}}$$ **Equation 3-3**

where $\vec{V}$ is the flow velocity vector, $\vec{n}$ is the unit vector normal to the cardiac wall surface and $\frac{d\vec{V}}{d\vec{n}}$ is the directional derivative of the velocity in the direction normal to the cardiac wall surface.

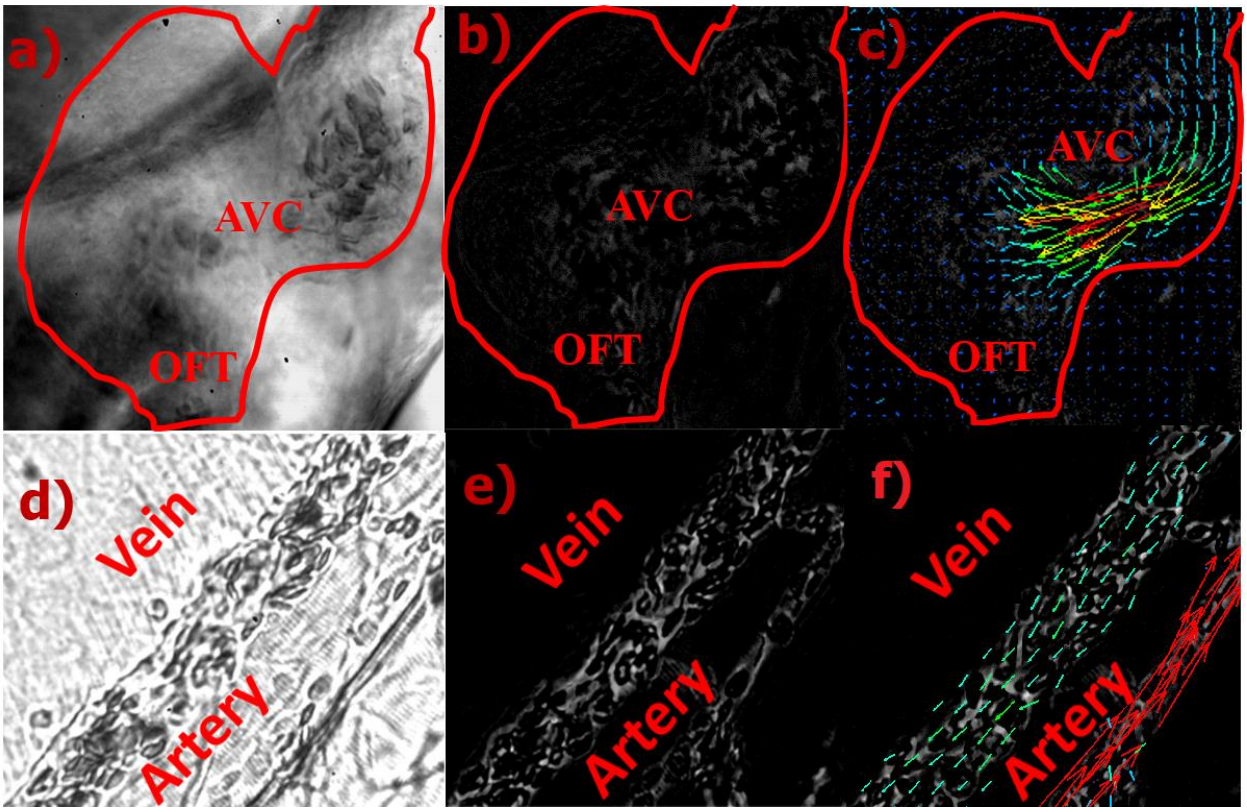

Figure 3-11: Raw images to velocity vector fields. a) raw image b) signal amplified image and c) velocity vectors superimposed on raw image of a 13 dpf medaka heart during ventricle diastole. AVC = Atrioventricular canal; OFT = ventricle outflow tract. d) raw image e) signal amplified image and f) velocity vectors superimposed on raw image of caudal vein and caudal artery. Red vectors denote higher velocity than green vectors.

Hematocrit (Ht) calculation

Ventricles images were cropped to retain a small area around the ventricle center. RBC pattern count (Nrbc) was calculated from the average auto-correlation plane of all the time-lapse ventricle images for each medaka heart as discussed in (235). The ventricle volume (Vvol) was calculated by multiplying the area of the images with the depth of focus. Then the Ht in percentage was calculated using Equation 3-4.

$$Ht = 100 * Volume\ of\ a\ RBC * \frac{Nrbc}{Vvol}$$ **Equation 3-4**

Viscosity (μ) calculation

The Walburn-Schneck model for a non-Newtonian fluid (233, 236) is used to calculate blood viscosity (μ) as a function of hematocrit (Ht) and shear rate (γ). In this work, the peak shear rate recorded in a heart cycle and the Ht in percentage calculated from Equation 3-4 is used in Equation 3-5.

$$\mu = C1\exp(C2 * Ht) * \exp\left(C4\left(\frac{TPMA}{Ht^2}\right)\right) * \gamma^{(-C3*Ht)} \qquad \textbf{Equation 3-5}$$

Here, C1=0.00797; C2=0.0608; C3=0.00499 and C4=14.59 L/g (233).

TPMA=total protein minus albumin=45 mg/mL (237).

WSS measurement

Three maximum values of velocity gradients extracted at three endocardial wall locations of AVC and OFT were spatially averaged at each time point of the heart cycle. Since the AVC and OFT regions are very narrow (15-25 μm diameter during peak filling), there are only 8-10 grid points (vectors) in that region. There is no time averaging involved as the peak flow in each location rapidly changes with time. WSS values are calculated using Equation 3-2.

3.6.7 Flow and WSS analysis in vessels

Vessel diameters were calculated from the images using a combination of thresholding and edge detection techniques. The RBC dimension (w) is of the same order as the vessel diameter (d) through which it flows. So, the flow velocity (V) is calculated assuming time-dependent plug flow. This assumption has been used in previous studies with zebrafish (140, 170). Due to a column of RBC at the center of the vessel, there exists a thin plasma layer devoid of cells near the vascular wall that exerts the WSS. The plasma viscosity of icefish was found to be similar to that in human plasma (238, 239) and in zebrafish tail vessels was assumed to be 1.2 cP in earlier studies (140, 240). Hence the plasma viscosity (μ) of 1.2 cP has been used for vascular WSS calculations as shown in .

$$WSS = \mu\frac{V}{h}, \text{ where } h = \frac{d-w}{2} \qquad \textbf{Equation 3-6}$$

3.6.8 qPCR analysis of gene expression profiles

Real time PCR primers were developed for the genes *fgf8, hoxb6b, nkx2.5, smyd1*, and *bmp4*, and control gene 18S mRNA (specifications in Table 3-2). The identified sequences were verified against the NCBI database using a standard Blast search. Total RNA isolation was performed on whole embryos using Quiagen RNeasy mini kit according to manufacturer protocols and quantified using a NanoDrop 2000C spectrophotometer (Thermo Scientific).

Table 3-2: List of primers used for real time PCR. All sequences are 5′ to 3′ and reverse primers are reverse compliments of the genetic sequence.

Gene	Accession Number	Orientation	Sequence	Product length (base pairs)	Primer Efficiency (%)
18s *mRNA*	AB105163.1	F	ACTCCGGTTCTATTTTGTGGGTTTT	92	119.1
		R	CTAGCGGCACAATACGAATGC		
fgf8	XM_004076908.3	F	GTGGAGACTGACACATTTGGAA	102	96.9
		R	GTTTTTCTTGCCAATGAGCTTC		
hoxb6b	AB208002.1	F	CGACCCGTTAAGACACTACTCC	182	113.6
		R	CCTCTGCGTCCTTGTAAAAAGT		
nkx2.5	EF206723.1	F	AGCTTTACCTCTGCGTTTTACG	91	92.6
		R	CATCTTTTCCTCGTTCATCCTC		
bmp4	DQ915174.1	F	TTTACAGGGATCAGGTGAAAGG	108	88.6
		R	AAGCAGGAAGTCCAAACATCTC		
smyd1	XM_004072212.3	F	GGCTTATGCTATCCTCATGGTC	194	121.8
		R	CTTCTTCCACAGACTTGGGTTC		

Eggs spawned by a medaka female are much less (3 to 4 eggs per day) compared to zebrafish. The size of each embryo is around 1.2 mm in diameter. Due to small size of the heart and low availability of samples per day, extracting only heart tissue would not generate enough RNA volume to run a qPCR analysis. In recent literature, qPCR analysis investigating cardiotoxicity have been performed extracting RNA from whole embryos or larvae (186, 241-244). The selected

genes were chosen from the existing literature owing to their well-defined over-expression during cardiac developmental events in vertebrates. The 18s mRNA is chosen as the control gene with 119.1% primer efficiency as included in Table 3-2**.**

Total RNA was treated for potential DNA contamination by incubating with DNase 1 (Thermo Scientific), according to manufacturer protocols. cDNA synthesis was performed on 50 ng of total RNA using SuperScript III reverse transcriptase (Invitrogen), according to manufacturer protocols. Samples were stored at -20ºC until qPCR analysis. qPCR analysis was performed using the iQ SYBR Green Supermix (Bio-Rad) and reactions were prepared according to the manufacturer's protocols. All reactions were processed using a CFX Connect qPCR machine (Bio-Rad) with accompanying software. For all genes, negative and no reverse-transcriptase control reactions were performed. A serial dilution was used for standard curves to determine the reaction efficiency of each primer pair. The Ct values for each sample were used to assess relative abundance of each gene in relation to the control gene 18S mRNA using the delta-delta Ct method (245). PCR efficiencies were $\geq$ 88.6% with an $R^2 \geq 0.86$.

3.7 Statistical Analysis

3.7.1 Cardiac Function and geometry

Statistical significance was tested for the cardiac function and geometry parameters by using Tukey-Kramer Honest Significant Difference (HSD) tests. The p-values for the parameters (HR, Re, Wo, A, EF and t_{diast}/T) between a pair of dpf are listed in **Table 3-3**.

Table 3-3: P-values from Tukey Kramer HSD tests comparing heart rate (HR), Reynolds number (Re) and Womersley number (Wo) at the atrial inflow, end-diastolic ventricle area (A), ventricle ejection fraction (EF) and fractional ventricle diastolic time (t_{diast}/T) between each pair of dpfs. n=5 for each dpf. * denotes p<0.0001. ** denotes p<0.001. * denotes p<0.05.**

p-values							
dpf		**HR (bpm)**	**Re**	**Wo**	**A(μm^2)**	**EF (%)**	**t_{diast}/T**
3	4	0.9995	0.9895	0.9597	1.0	1.0	0.9521
3	5	0.6808	0.4186	0.1985	0.9996	0.5024	0.9824
3	6	0.4801	0.2881	0.0821	1.0	0.9999	0.1153
3	7	0.1206	0.8716	0.0109*	0.9758	0.9636	0.5276
3	8	0.0008**	0.0148*	<0.0001***	0.9991	1.0	1.0
3	9	<0.0001***	<0.0001***	<0.0001***	0.1996	1.0	0.9893
3	10	<0.0001***	0.0015*	<0.0001***	0.0004**	0.0097*	0.9586
3	11	<0.0001***	0.1805	<0.0001***	0.0037*	0.4673	0.9957
3	12	<0.0001***	0.0004**	<0.0001***	0.0034*	0.0713	0.9586
3	13	<0.0001***	<0.0001***	<0.0001***	<0.0001***	0.0586	0.0033*
3	14	<0.0001***	<0.0001***	<0.0001***	0.0004**	0.0267*	0.0033*
4	5	0.9939	0.9967	0.9758	1.0	0.5024	1.0
4	6	0.9635	0.9916	0.8693	1.0	0.9999	0.9335
4	7	0.5942	1.0	0..3684	0.9997	0.9636	0.9997
4	8	0.0166*	0.5465	0.0046*	1.0	1.0	0.9997
4	9	<0.0001***	0.0148*	<0.0001***	0.4877	1.0	0.3551
4	10	0.0010**	0.1848	0.0001**	0.0017*	0.0097*	0.242
4	11	<0.0001***	0.9687	<0.0001***	0.0143*	0.4673	0.4666
4	12	<0.0001***	0.0825	<0.0001***	0.0154*	0.0713	0.242
4	13	<0.0001***	0.0003**	<0.0001***	<0.0001***	0.0586	<0.0001***
4	14	<0.0001***	0.0121*	<0.0001***	0.0022*	0.0267*	<0.0001***
5	6	1.0	1.0	1.0	1.0	0.2356	0.7766
5	7	0.9881	0.9994	0.9685	1.0	0.0627	0.9942
5	8	0.1464	0.9797	0.0810	1.0	0.7027	1.0
5	9	0.0008**	0.1158	0.0004**	0.7043	0.8093	0.4264
5	10	0.0132*	0.704	0.0029*	0.0043*	0.9522	0.2929
5	11	<0.0001***	1.0	<0.0001***	0.0310*	1.0	0.552
5	12	<0.0001***	0.4411	0.0002**	0.0363*	1.0	0.2929
5	13	<0.0001***	0.0023*	<0.0001***	<0.0001***	0.9999	<0.0001***
5	14	<0.0001***	0.0966	<0.0001***	0.0056*	0.9757	<0.0001***
6	7	0.9989	0.9976	0.9979	0.9999	0.9999	0.9999
6	8	0.258	0.9804	0.1874	1.0	0.9993	0.4793
6	9	0.0021*	0.0910	0.0016*	0.5285	0.9866	0.0053*
6	10	0.0302*	0.6798	0.0097*	0.0020*	0.003*	0.0026*
6	11	<0.0001***	1.0	<0.0001***	0.0166*	0.2136	0.0126*
6	12	<0.0001***	0.4024	0.0005**	0.0182*	0.0223*	0.0026*
6	13	<0.0001***	0.0013*	<0.0001***	<0.0001***	0.0181*	<0.0001***
6	14	<0.0001***	0.0745	<0.0001***	0.0026*	0.0088*	<0.0001***
7	8	0.8502	0.5391	0.8002	1.0	0.9267	0.9144

Table 3-3 continued

7	9	0.0551	0.0068*	0.0509	0.88	0.754	0.0653
7	10	0.3422	0.146	0.1874	0.0061*	0.0004**	0.0376*
7	11	0.0016*	0.9849	0.0012*	0.0497*	0.0554	0.1104
7	12	0.0024*	0.0546	0.0171*	0.0572	0.0031*	0.0376*
7	13	<0.0001***	<0.0001***	<0.0001***	<0.0001***	0.0025*	<0.0001***
7	14	0.0009**	0.0053*	0.0011*	0.0079*	0.0015*	<0.0001***
8	9	0.9003	0.7279	0.923	0.4966	1.0	0.8595
8	10	0.9998	0.9998	0.9979	0.0007**	0.0308*	0.7425
8	11	0.1607	0.9966	0.1592	0.0096*	0.6696	0.9144
8	12	0.2571	0.9879	0.6626	0.0081*	0.1797	0.7425
8	13	0.0012*	0.0481*	0.002*	<0.0001***	0.1534	0.0011*
8	14	0.1363	0.6743	0.1874	0.0008**	0.0667	0.0011*
9	10	0.9985	0.9879	1.0	0.1905	0.0396*	1.0
9	11	0.9312	0.1569	0.907	0.5988	0.7797	1.0
9	12	0.9884	0.9998	1.0	0.7535	0.2354	1.0
9	13	0.0652	0.9272	0.0821	0.0013*	0.2012	0.0807
9	14	0.9299	1.0	0.9526	0.262	0.0881	0.0807
10	11	0.4443	0.8238	0.5892	1.0	0.963	1.0
10	12	0.6288	1.0	0.9865	0.9931	0.9976	1.0
10	13	0.0053*	0.2589	0.0172*	0.8657	0.9989	0.1367
10	14	0.4086	0.9794	0.6709	1.0	1.0	0.1367
11	12	1.0	0.5618	0.9987	1.0	1.0	1.0
11	13	0.8821	0.0027*	0.937	0.6596	1.0	0.1093
11	14	1.0	0.1309	1.0	1.0	0.9817	0.1093
12	13	0.58	0.5053	0.4021	0.1694	1.0	0.1367
12	14	1.0	0.9993	0.9999	0.9995	0.9993	0.1367
13	14	0.7917	0.9498	0.794	0.6080	0.9997	1.0

3.7.2 Hematocrit, viscosity and shear rate in the ventricle

Statistical significance was tested for all the cardiac function and geometry parameters by using Tukey-Kramer Honest Significant Difference (HSD) test. The p-values that denote difference of mean values of the shear-dependent parameters (hematocrit, viscosity, peak shear rate at AVC, peak WSS at AVC and OFT) between a pair of dpf are listed in **Table 3-4**.

Table 3-4: P-values from Tukey Kramer HSD tests comparing hematocrit (Ht), viscosity (μ), peak shear rate (γ) and peak wall shear stress (WSS) at the atrioventricular canal (AVC), peak WSS at ventricle outflow tract (OFT) between each pair of dpfs. n=5 at each dpf. * denotes p<0.0001. ** denotes p<0.001. * denotes p<0.05.**

p-values						
dpf		**Ht (%)**	**μ (cp)**	**Peak_γ**	**Peak_WSS_AVC**	**Peak_WSS_OFT**
3	4	1.0	1.0	1.0	1.0	0.9994
3	5	0.9901	0.9999	0.9955	0.9911	0.9996
3	6	0.1915	0.875	<0.0001***	<0.0001***	0.0001**
3	7	0.9974	0.9457	0.5091	0.4055	0.9999
3	8	0.9996	0.0884	0.2372	0.4788	1.0
3	9	0.9992	0.0115*	0.0052*	0.0327*	0.2965
3	10	1.0	0.0069*	0.0136*	0.0951	<0.0001***
3	11	0.9955	0.0350*	0.0913	0.3378	0.0001**
3	12	0.7238	0.1370	0.0481*	0.1835	0.0009**
3	13	0.9996	0.0536	0.0360*	0.1949	0.0425*
3	14	1.0	0.2783	0.4792	0.6320	0.0220*
4	5	0.9705	1.0	0.9994	0.9987	0.8894
4	6	0.1625	0.9838	<0.0001***	<0.0001***	<0.0001***
4	7	0.9894	0.9963	0.6985	0.6051	0.9288
4	8	1.0	0.2955	0.4045	0.6771	0.9985
4	9	1.0	0.0607	0.0163*	0.0830	0.0480*
4	10	1.0	0.0354*	0.0382*	0.2008	<0.0001***
4	11	0.9998	0.1351	0.1803	0.5334	<0.0001***
4	12	0.8936	0.3474	0.1121	0.3378	<0.0001***
4	13	1.0	0.1889	0.0879	0.3537	0.0040*
4	14	1.0	0.5986	0.6710	0.8066	0.0019*
5	6	0.8513	0.9936	0.0002**	<0.0001***	0.0012*
5	7	1.0	0.9990	0.9837	0.975	1.0
5	8	0.7301	0.3273	0.8574	0.9877	0.9999
5	9	0.6835	0.0629	0.0866	0.3799	0.7915
5	10	0.8545	0.0365*	0.1806	0.6604	<0.0001***
5	11	0.6083	0.148	0.5488	0.9455	0.0015*
5	12	0.1355	0.3904	0.4161	0.8377	0.0096*
5	13	0.7203	0.2091	0.3491	0.8520	0.2518
5	14	0.964	0.6592	0.9785	0.998	0.1535
6	7	0.8481	1.0	0.0063*	0.0027*	0.0008*
6	8	0.0304*	0.9899	0.0204*	0.0020*	0.000
6	9	0.0250*	0.7804	0.3824	0.0487*	0.1376
6	10	0.0693	0.6027	0.2312	0.0182*	0.6160
6	11	0.0239*	0.8977	0.1177	0.0089*	1.0
6	12	0.0018*	0.9820	0.0979	0.0086*	0.9984
6	13	0.0292*	0.9450	0.1219	0.0080*	0.5695
6	14	0.1503	0.9997	0.0071*	0.0011*	0.7233
7	8	0.8481	0.9640	1.0	1.0	1.0
7	9	0.8133	0.6502	0.6933	0.9880	0.7245

Table 3-4 continued

7	10	0.9262	0.4695	0.8755	0.9998	<0.0001***
7	11	0.7422	0.8053	0.9951	1.0	0.0011*
7	12	0.2273	0.9504	0.9870	1.0	0.0069*
7	13	0.8410	0.8777	0.9743	1.0	0.2024
7	14	0.9865	0.9976	1.0	1.0	0.1198
8	9	1.0	0.9995	0.9267	0.9756	0.3419
8	10	1.0	0.9874	0.9875	0.9992	<0.0001***
8	11	1.0	1.0	1.0	1.0	0.0001**
8	12	0.9857	1.0	0.9999	1.0	0.0011*
8	13	1.0	1.0	0.9994	1.0	0.0526
8	14	1.0	1.0	1.0	1.0	0.0275*
9	10	1.0	1.0	1.0	1.0	0.0002**
9	11	1.0	1.0	0.9995	0.9756	0.1635
9	12	0.9911	1.0	0.9996	0.9998	0.5471
9	13	1.0	1.0	0.9999	0.9997	0.9990
9	14	1.0	0.99	0.7219	0.9257	0.9914
10	11	1.0	1.0	1.0	1.0	0.5644
10	12	0.9805	0.9995	1.0	1.0	0.1009
10	13	1.0	0.9998	1.0	1.0	0.0033*
10	14	1.0	0.9362	0.8938	0.9935	0.0066*
11	12	0.9992	1.0	1.0	1.0	0.9993
11	13	1.0	1.0	1.0	1.0	0.6238
11	14	0.9998	0.9986	0.9965	1.0	0.7718
12	13	0.9871	1.0	1.0	1.0	0.9699
12	14	0.9067	1.0	0.9905	0.9996	0.9939
13	14	1.0	0.9998	0.9803	0.9997	1.0

3.7.3 Cardiac gene expression

Statistical tests of the relative gene expression across developmental stages were performed using commercial software JMP. Tukey-Kramer HSD test examined statistical differences with p value <0.05 considered significant. The number of samples for each gene in each dpf was 8-10 except for one sample expressing *smyd1* at 0.5 dpf. The p-values that denote difference of mean values of the relative cardiac gene expressions (*fgf8, hoxb6b, nkx2.5, bmp4* and *smyd1*) between a pair of dpf are listed in **Table 3-5**.

Table 3-5: p-values from Tukey Kramer HSD test comparing relative gene expressions of *fgf8, hoxb6b, nkx2.5, bmp4* and *smyd1* between each pair of dpfs. n=8-10 at each dpf. * denotes p<0.0001. ** denotes p<0.001. * denotes p<0.05.**

p-values						
dpf		***fgf8***	***hoxb6b***	***nkx2.5***	***bmp4***	***smyd1***
0.5	1	1.0	<0.0001***	<0.0001***	0.9998	x
0.5	1.5	0.9965	<0.0001***	<0.0001***	1.0	x
0.5	2	1.0	<0.0001***	<0.0001***	0.9998	x
0.5	2.5	1.0	<0.0001***	<0.0001***	0.0244*	x
0.5	3	<0.0001***	<0.0001***	0.0312*	0.8455	x
0.5	4	0.9998	<0.0001***	<0.0001***	0.0005**	x
0.5	5	0.6993	<0.0001***	<0.0001***	<0.0001***	x
0.5	6	1.0	<0.0001***	<0.0001***	0.0110*	x
0.5	7	0.8466	<0.0001***	<0.0001***	0.9993	x
0.5	8	0.2383	<0.0001***	<0.0001***	0.3335	x
0.5	10	0.2017	<0.0001***	<0.0001***	0.0008**	x
0.5	12	0.5509	<0.0001***	<0.0001***	0.0019*	x
1	1.5	0.8966	0.4922	1.0	0.9989	0.8504
1	2	0.9984	0.0220*	0.8931	1.0	0.0002**
1	2.5	1.0	0.0003**	0.0689	0.2065	<0.0001***
1	3	<0.0001***	1.0	0.5068	0.3217	0.3380
1	4	1.0	0.0021*	<0.0001***	0.0096*	<0.0001***
1	5	0.9612	0.0155*	0.0002**	0.0004**	<0.0001***
1	6	1.0	0.8180	0.0476*	0.1164	<0.0001***
1	7	0.4636	0.3238	0.9696	1.0	0.0020*
1	8	0.6142	<0.0001***	0.0011*	0.8322	<0.0001***
1	10	0.5471	0.0819	0.0003**	0.0129*	<0.0001***
1	12	0.9006	0.0524	<0.0001***	0.0251*	<0.0001***
1.5	2	1.0	0.9825	0.8825	0.9881	0.0534
1.5	2.5	0.9985	0.3572	0.0642	0.0142*	<0.0001***
1.5	3	<0.0001***	0.6833	0.5252	0.9165	0.9998
1.5	4	0.7752	0.7250	<0.0001***	0.0002**	<0.0001***
1.5	5	0.0949	0.9547	0.0002**	<0.0001***	<0.0001***
1.5	6	0.9953	1.0	0.0442*	0.0062*	<0.0001***
1.5	7	1.0	0.0003**	0.9651	0.9963	0.2297
1.5	8	0.0115*	0.0036*	0.0010*	0.2449	<0.0001***
1.5	10	0.0097*	0.9985	0.0003**	0.0004**	<0.0001***
1.5	12	0.0534	0.9941	<0.0001***	0.0010*	<0.0001***
2	2.5	1.0	0.9908	0.9342	0.3634	0.0218*
2	3	<0.0001***	0.0495*	0.0066*	0.1777	0.2192
2	4	0.9888	1.0	0.0168*	0.0246*	0.0024*
2	5	0.4023	1.0	0.0763	0.0013*	0.0311*
2	6	1.0	0.8401	0.8884	0.2265	0.0870
2	7	0.9762	<0.0001***	1.0	1.0	1.0

Table 3-5 continued

2	8	0.0874	0.1683	0.2135	0.9400	<0.0001***
2	10	0.0730	1.0	0.0889	0.0316*	0.0019*
2	12	0.2746	1.0	0.0378*	0.0563	0.0403*
2.5	3	<0.0001***	0.0008**	<0.0001***	<0.0001***	<0.0001***
2.5	4	0.9994	1.0	0.6179	0.9968	0.9999
2.5	5	0.6347	0.9988	0.9074	0.7669	1.0
2.5	6	1.0	0.1279	1.0	1.0	1.0
2.5	7	0.8889	<0.0001***	0.8190	0.2717	0.0100*
2.5	8	0.1950	0.8793	0.9903	0.9998	0.0023*
2.5	10	0.1644	0.9724	0.9129	0.9971	0.9995
2.5	12	0.4842	0.9900	0.7895	0.9991	0.9999
3	4	<0.0001***	0.0055*	<0.0001***	<0.0001***	<0.0001***
3	5	<0.0001***	0.0353*	<0.0001***	<0.0001***	<0.0001***
3	6	<0.0001***	0.9318	<0.0001***	<0.0001***	<0.0001***
3	7	0.0003**	0.1900	0.0169*	0.2488	0.5977
3	8	<0.0001***	<0.0001***	<0.0001***	0.0026*	<0.0001***
3	10	<0.0001***	0.1548	<0.0001***	<0.0001***	<0.0001***
3	12	<0.0001***	0.1042	<0.0001***	<0.0001***	<0.0001***
4	5	0.9911	1.0	1.0	0.9997	1.0
4	6	0.9999	0.3866	0.7084	0.9997	0.9987
4	7	0.3073	<0.0001***	0.0066*	0.0149*	0.0011*
4	8	0.7760	0.5590	0.9993	0.8131	0.0161*
4	10	0.7126	0.9995	1.0	1.0	1.0
4	12	0.9671	0.9999	1.0	1.0	1.0
5	6	0.7226	0.7499	0.9473	0.8455	1.0
5	7	0.0118*	<0.0001***	0.0346*	0.0007**	0.0146*
5	8	1.0	0.2993	1.0	0.2848	0.0300*
5	10	0.9998	1.0	1.0	0.9998	1.0
5	12	1.0	1.0	1.0	0.9996	1.0
6	7	0.8287	0.0017*	0.7416	0.1602	0.0417*
6	8	0.2560	0.0006**	0.9964	0.9973	0.0019*
6	10	0.2171	0.9611	0.9503	0.9998	0.9955
6	12	0.5760	0.9180	0.8587	0.9999	0.9992
7	8	0.0009**	<0.0001***	0.1119	0.8901	<0.0001***
7	10	0.0008**	<0.0001***	0.0420*	0.0197*	0.0009**
7	12	0.0057*	<0.0001***	0.0159*	0.0367*	0.0199*
8	10	1.0	0.1397	1.0	0.8291	0.0319*
8	12	1.0	0.2006	1.0	0.8911	0.1834
10	12	1.0	1.0	1.0	1.0	1.0

4. EVOLUTION OF CARDIAC TISSUE AND FLOW MECHANICS IN DEVELOPING JAPANESE MEDAKA

Authors: Sreyashi Chakraborty[1], Maria S. Sepulveda[2], Pavlos Vlachos[3]*
1,3: Dept. of Mechanical Engineering, Purdue University
2: Dept. of Forestry & Natural Resources, Purdue University

4.1 Abstract

The effects of pressure drop across cardiac valve cushion regions and endocardial wall strain triggering cardiac morphogenesis in a teleost species heart are poorly understood. In the presented work, we utilize microscale particle image velocimetry (μPIV) flow measurements of developing medaka hearts from 3 to 14 dpf (n=4-5 at each dpf) to quantify the pressure field and endocardial wall strain. Peak pressure drop at the atrioventricular canal (ΔP_{AVC}) and outflow tract (ΔP_{OFT}) show a steady increase with fish age progression. Pressure drops when non-dimensionalized with blood viscosity and heart rate at each dpf are comparable with measurements in zebrafish hearts. Retrograde flows captured at these regions display a negative pressure drop. A novel metric, Endocardial Work (EW), is introduced by analyzing the ΔP_{AVC}-strain curves, which is a non-invasive measure of work required for ventricle filling. EW is a metric that can differentiate between the linear heart stage (< 100 Pa-%), cardiac looped chamber stage (< 300 Pa-%), and the fully formed chamber stage (> 300 Pa-%).

4.2 Introduction

Cardiac chamber formation and development in teleosts is a dynamic process where mechanical forces generated by the pulsating heart cause endocardial cells to migrate or reorganize, leading to cardiac remodeling. However, past studies investigating biomechanics have mainly probed into the flow wall shear stress (WSS) variation, with little to no attention to the pressure drop (ΔP) that induces the varying WSS profiles or the cardiac wall strain facilitating morphological changes in the endocardium. Pressure and strain data can potentially indicate the amount of endocardial work (EW) required for ventricle filling or ejection (246-251). Standard indices of ventricle function do not measure myocardial work related to the metabolic demand. The EW has been shown in humans and higher vertebrates to directly reflect oxygen demand and metabolic consumption. Hence it is

a comprehensive metric for regional ventricle function that can be developed to distinguish between healthy and diseased ventricles (246, 247). To our knowledge, no studies have evaluated in vivo EW in teleost ventricles. Owing to the small size of the teleosts and limited spatial resolution of images it is challenging to accurately calculate velocity gradients that contribute to calculations of pressure and strain.

Pressure measurements in previous studies were time-consuming. They were done with cannulae at a single point, with intrusive probes that provided limited information about the spatiotemporal pressure variation (137, 252). Pressure gradients in the zebrafish (*Danio rerio*) heart were calculated using Laplace law (216) or from the knowledge of circumferential stress (156). However, the accuracy of these measurements is limited since they neglected viscous forces in the heart. A non-invasive spatially and temporally resolved pressure field in a 48-hour post-fertilization (hpf) zebrafish heart was first calculated using micro-Particle Image Velocimetry (μPIV) analysis by Dasi et al. (161). The imaging was limited to the atrium only because the fish's eyes and head blocked a part of the ventricle.

Cardiac wall strain measurements of teleosts are affected by spatially under-resolved images that cannot accurately capture the wall motion. The recent introduction of high-frequency ultrasound probes designed for small animals enabled Hein et al. (253) to measure strain rate and strain (%) measurements of adult zebrafish suffering a myocardial injury. However, echocardiographic measurements are impossible to acquire from embryonic and larval fish due to the small size and difficulty of introducing a contrast agent. Lee et al. utilized the optical transparency of 48 hpf, 75 hpf and 100 hpf zebrafish (both control and mutants) and used selective plane illumination microscopic imaging technique to report strain measurements (181).

Thus, an overview of the literature highlights the need to measure pressure and strain in teleost hearts accurately. To our knowledge, there is no baseline framework for embryonic vertebrate animal models that investigates the variation of EW along the developmental stages. In the current work, we selected Japanese Medaka (*Oryzias latipes*) as our teleost model because it is larger than zebrafish in both embryonic and larval stages. Additionally, medaka grows two times slower than zebrafish (164, 165), allowing to capture developmental landmarks during cardiac morphogenesis from embryonic to larval stages.

The objective of this work is to conduct a series of live experiments to image the Japanese medaka heart under a microscope followed by a subsequent μPIV analysis and quantify the ΔP

across the atrioventricular canal (AVC) and outflow tract (OFT), endocardial wall strain of the ventricle and consequently the EW required for ventricle filling across development in embryo/larva.

4.3 Results

4.3.1 Cardiac function and geometry

The progression of cardiac function and geometry parameters for this dataset have been described in detail in our previous analysis of wall shear stress (WSS) measurements done with this data (254). The mean value of each parameter is presented in **Table 4-1**. HR represents heart rate in beats per minute (bpm), Re and Wo represent Reynolds number and Womersley number respectively and both are non-dimensional. "A" represents the ventricle area during peak diastole. EF represents the ejection fraction of the ventricle.

4.3.2 Pressure contours across the AVC and the OFT

Pressure field variation across the atrium and ventricle along three phases of the ventricle filling cycle is plotted in **Figure 4-1** for a medaka heart at 3 dpf, 8 dpf and 13 dpf.

Table 4-1 : Cardiac function and geometry parameters

dpf	HR (bpm)	Re	Wo	A (μm^2)	EF (%)
3	78.5 ± 3.7	0.02 ± 0.003	0.021 ± 0.005	1143.3 ± 75.9	58.2 ± 4.7
4	85.5 ± 3.3	0.03 ± 0.007	0.022 ± 0.004	1433.3 ± 49.9	58.2 ± 7.9
5	93 ± 6.5	0.03 ± 0.008	0.023 ± 0.006	1610 ± 151.2	72.2 ± 4.8
6	93 ± 2.4	0.04 ± 0.005	0.023 ± 0.004	1466.7 ± 212.5	54.5 ± 7.4
7	106 ± 7.5	0.04 ± 0.008	0.024 ± 0.006	1857.5 ± 369.3	50.5 ± 9.3
8	132 ± 4.9	0.04 ± 0.003	0.027 ± 0.005	1604 ± 104.8	59.5 ± 10
9	150.5 ± 2.5	0.06 ± 0.011	0.029 ± 0.004	2660 ± 298.5	61.2 ± 11.9
10	143.3 ± 6.2	0.07 ± 0.009	0.028 ± 0.006	4065 ± 648.5	81.3 ± 3.4
11	161.3 ± 18.7	0.08 ± 0.027	0.029 ± 0.010	3796.7 ± 369.2	72.6 ± 3.1
12	145 ± 2.4	0.07 ± 0.007	0.028 ± 0.004	3531.2 ± 457.5	75.9 ± 6.7
13	173.6 ± 7.1	0.1 ± 0.034	0.031 ± 0.006	4884 ± 1095.5	76.3 ± 4.8
14	172.4 ± 7.1	0.1 ± 0.008	0.031 ± 0.006	3906 ± 1312.3	81 ± 5.5

A zero-pressure boundary condition is applied at the ventricle outflow. Both the atrial inflow and the ventricle outflow remain closed throughout $T_{dias,}$ which is the period of the ventricle filling

cycle. At $0.3T_{dias}$ the peak pressure drop across the AVC is 800*(HR*μ) at 3dpf, 1200*(HR*μ) at 8 dpf and 2000*(HR*μ) at 13dpf. The atrium experiences the highest pressure and blood flows through the AVC from the atrium to the ventricle. At $0.6T_{dias}$ the AVC pressure drop reduces in magnitude while blood continues to flow in the same direction [500*(HR*μ) at 3dpf, 900*(HR*μ) at 8 dpf and 1200*(HR*μ) at 13dpf]. At $0.9T_{dias}$ the ventricle filling has almost ended with blood flowing from atrium to ventricle at 0.2 mm/s at 3dpf suffering a pressure drop of 200*(HR*μ) at the AVC region. However, due to the absence of the valves in the AVC, there is a negative pressure drop across the AVC that causes retrograde flow with a velocity of approximately 1 mm/s from the ventricle to atrium [-200*(HR*μ) at 8 dpf and -500*(HR*μ) at 13dpf] (**Figure 4-1**).

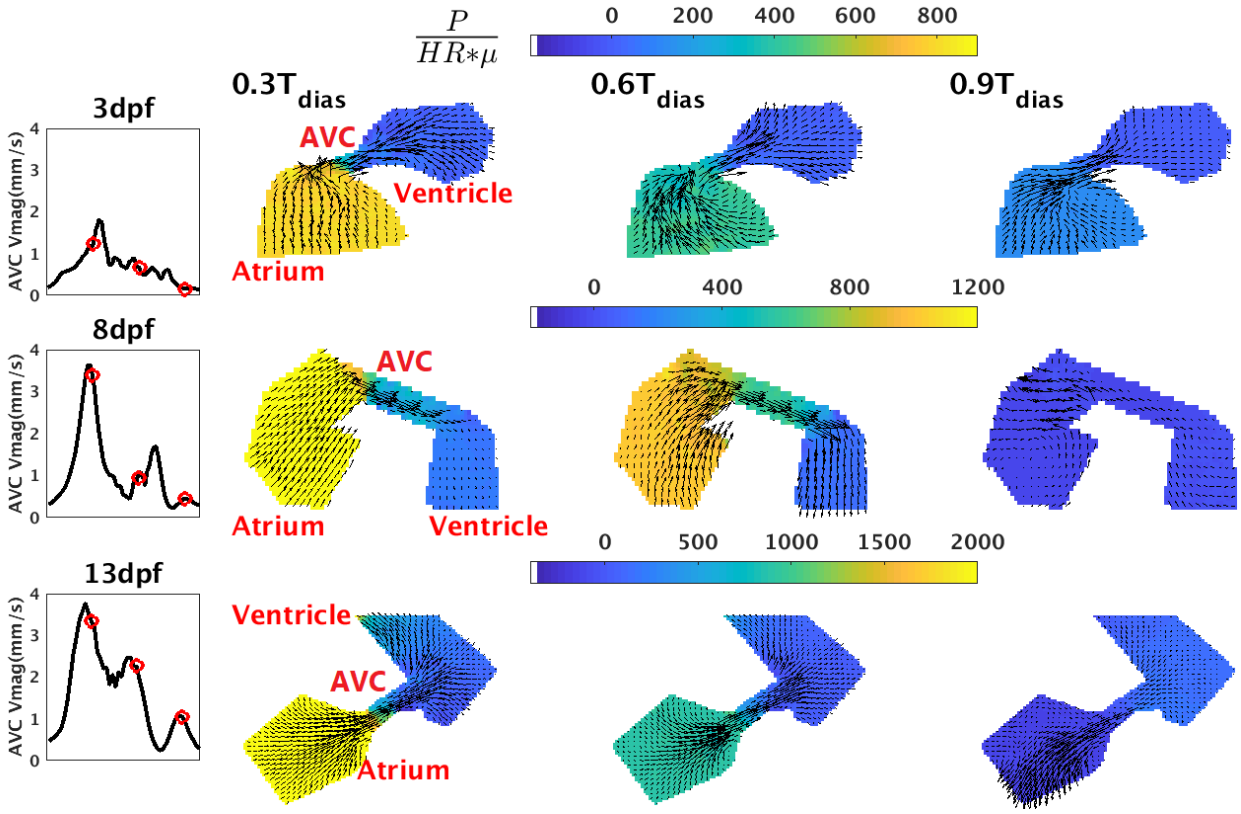

Figure 4-1: Pressure field across ventricle, atrium and AVC during ventricle diastole at 3 dpf, 8dpf and 13 dpf.

The pressure field variation across the ventricle and the bulbus arteriosus (BA) along three phases of the ventricle systolic cycle is plotted in **Figure 4-2** for a medaka heart at 3 dpf, 8 dpf and 13 dpf. A zero-pressure boundary condition is applied at the BA outflow. The narrow region joining the ventricle and the BA is referred to as the outflow tract (OFT). Both the atrial inflow and the AVC

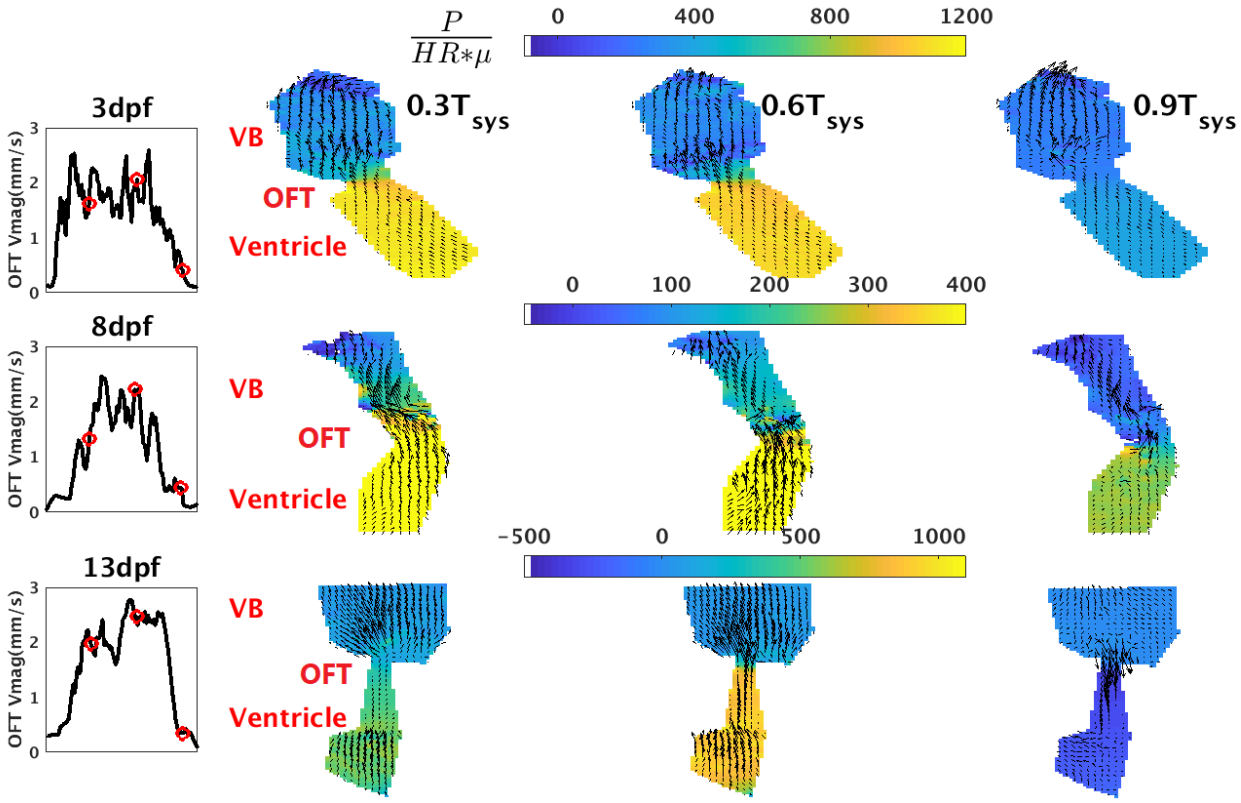

Figure 4-2: Pressure field across ventricle, VB and OFT during ventricle diastole at 3 dpf, 8dpf and 13 dpf.

inflow to the ventricle remain closed throughout T_{sys}, which is the period of the ventricle systolic cycle. At $0.3T_{sys}$ the peak pressure drop across the OFT is 1200*(HR*μ) at 3dpf, 550*(HR*μ) at 8 dpf and 700*(HR*μ) at 13dpf. The ventricle experiences higher pressure, and blood flows through the OFT from the ventricle to the BA. At $0.6T_{sys}$, the OFT pressure drop almost stays constant in magnitude during 3 dpf and 8dpf. [3dpf : 1150*(HR*μ), 8dpf : 500*(HR*μ)]. Interestingly for the 13 dpf heart the OFT pressure drop increases substantially at $0.6T_{sys}$ to 1100*(HR*μ). At $0.9T_{sys}$ the ventricle outflow has almost ended with blood flowing from ventricle to BA at 0.1 mm/s at 3dpf and 8dpf suffering a pressure drop of 300*(HR*μ) at the OFT region. But due to absence of the valves in the narrow OFT there is a negative pressure drop of -300*(HR*μ) at 13dpf that causes retrograde flow with velocity 0.3 mm/s from the BA to the ventricle (**Figure 4-2**).

4.3.3 Time variation of pressure drop across AVC and OFT

Time variations of velocity magnitude and pressure drop across AVC (dimensional and non-dimensional) are plotted for a ventricle diastolic cycle in **Figure 4-3**. Similar variations of velocity magnitude and pressure drop across OFT are plotted for a ventricle systolic cycle in **Figure 4-4**.

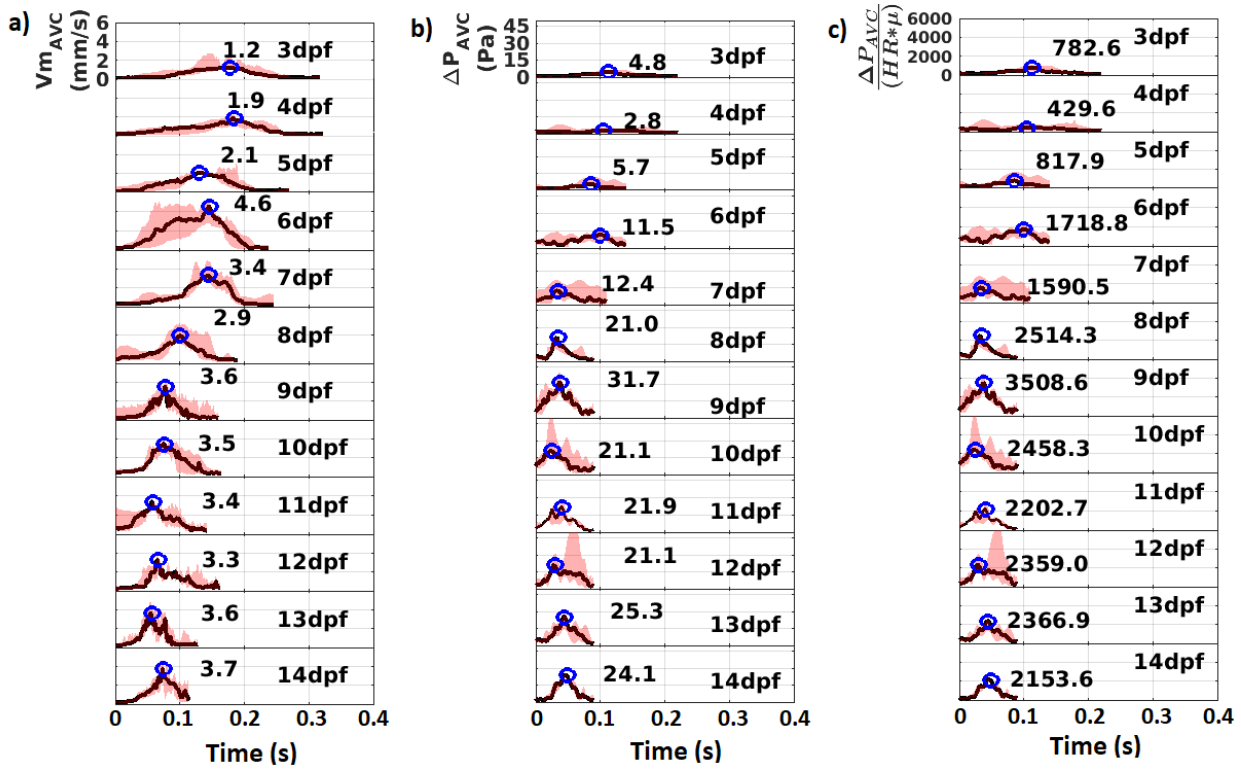

Figure 4-3: Time variation profiles in the atrioventricular canal (AVC) for the flow parameters a) Velocity Magnitude (Vm_{AVC}) b) Pressure drop (ΔP_{AVC}) and c) Non-dimensionalized pressure drop $\frac{\Delta P_{AVC}}{HR*\mu}$. Black lines denote the median profiles while the pink shade denotes region between maximum and minimum profiles. The peak values of the median profile are marked on each plot by a blue circle. n=3-5 for each dpf.

The pink shaded region between the minimum and maximum time variations in each dpf depicts the bounds within which the profiles across 4-5 samples fluctuate. The black line shows the median profile for each dpf. The peak values of the median profile are marked on each plot by a blue circle. A small pressure drop between 3dpf and 5dpf drives the low velocity flow into the ventricle when the AVC is not clearly defined. At 6dpf peak values of both Vm_{AVC} and ΔP_{AVC} increase considerably owing to narrowing of the AVC region after cardiac looping. At 7dpf, the peak median Vm_{AVC} and the peak median $\frac{\Delta P_{AVC}}{HR*\mu}$ reduce a little. As the fish prepares to hatch between 8

dpf and 9 dpf, there is a rise in peak flow velocity and pressure drop. After hatching, they eventually plateau from 10 dpf to 14 dpf.

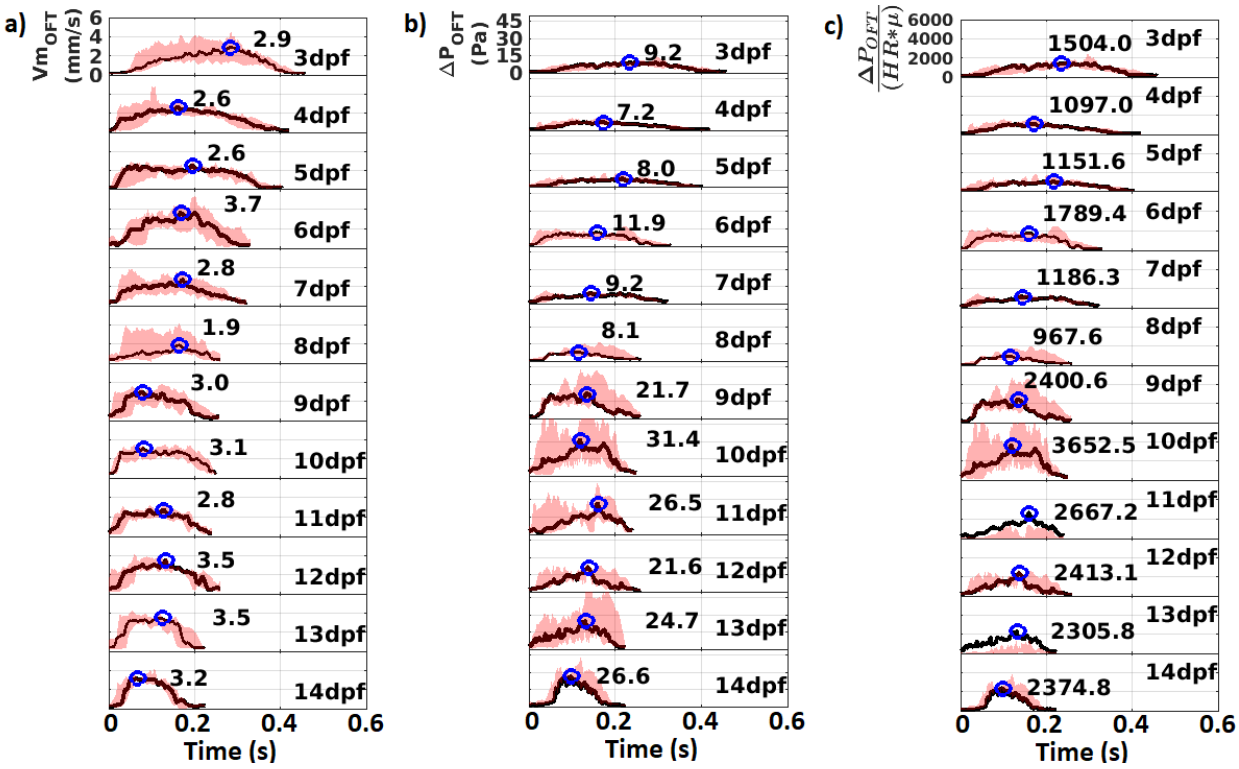

Figure 4-4: Time variation profiles in the atrioventricular canal (OFT) for the flow parameters a) Velocity Magnitude (Vm_{OFT}) b) Pressure drop (ΔP_{OFT}) and c) Non-dimensionalized pressure drop $\frac{\Delta P_{OFT}}{HR*\mu}$. Black lines denote the median profiles while the pink shade denotes region between maximum and minimum profiles. The peak values of the median profile are marked on each plot by a blue circle. n=3-5 for each dpf.

At 3 dpf, unlike the AVC, the peak flow velocity and pressure drop through OFT is high which reduces at 4 dpf and 5 dpf. At 6dpf, there is a substantial rise in the peak median Vm_{OFT}. Moreover, the peak median $\frac{\Delta P_{OFT}}{HR*\mu}$ that can be attributed to the narrowing of OFT after cardiac looping. These parameters decrease subsequently at 7 dpf and 8 dpf. After hatching, the peak median Vm_{AVC} and the peak median $\frac{\Delta P_{AVC}}{HR*\mu}$ increase at 9 dpf and fluctuates within a small range from 9 dpf to 14 dpf.

4.3.4 Strain measurements of the ventricle wall

Endocardial wall strain (%) is extracted during a heart cycle for each sample at each dpf. **Figure 4-5a** shows the 13 dpf ventricle during peak diastole. The red boundary has been drawn manually

to outline the ventricle. The wall locations on the pericardium and the endocardium are colored by the % strain experienced at each location. **Figure 4-5b** shows the time variation of endocardial

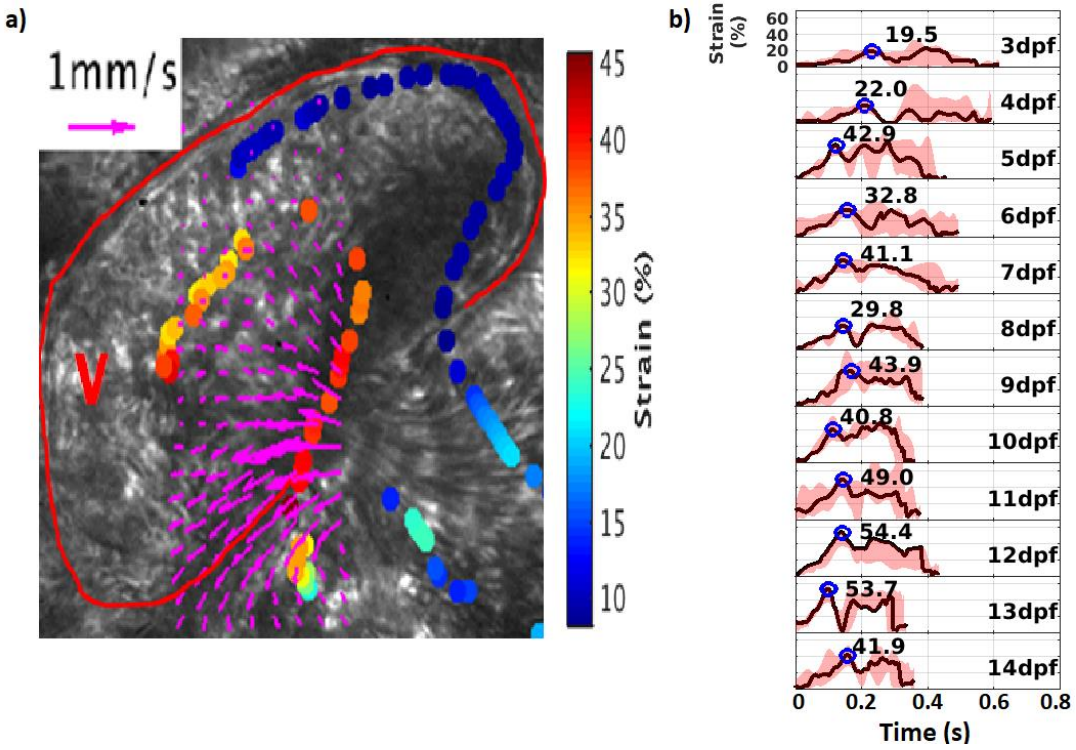

Figure 4-5: Strain measurement of the ventricle wall along a heart cycle. a) Pericardial and endocardial strain overlapped with velocity vectors on raw image of a 13 dpf medaka heart at peak diastole. V stands for ventricle. b)Variation of strain time history across medaka age progression.

strain along a heart cycle. A black line represents the median profile across 5 samples at each dpf. The pink shaded region between the minimum and maximum time variations in each dpf depicts the bounds within which the profiles across 5 samples fluctuate. The peak strain during ventricle diastole of the median profile is marked on each plot by a blue circle. The peak diastolic strain evolution with age progression is low at 3 dpf (19.5%) and 4 dpf (22%). But 5 dpf onwards, the median peak does not follow a specific trend with age progression. It fluctuates between 29% and 55%.

4.3.5 EW measurement from ΔPAVC-strain loop

Pressure drop across AVC (ΔP_{AVC}) is plotted across endocardial wall strain for a ventricle diastolic cycle in a medaka heart at each dpf in **Figure 4-6**. The endocardial work (EW) represents the area

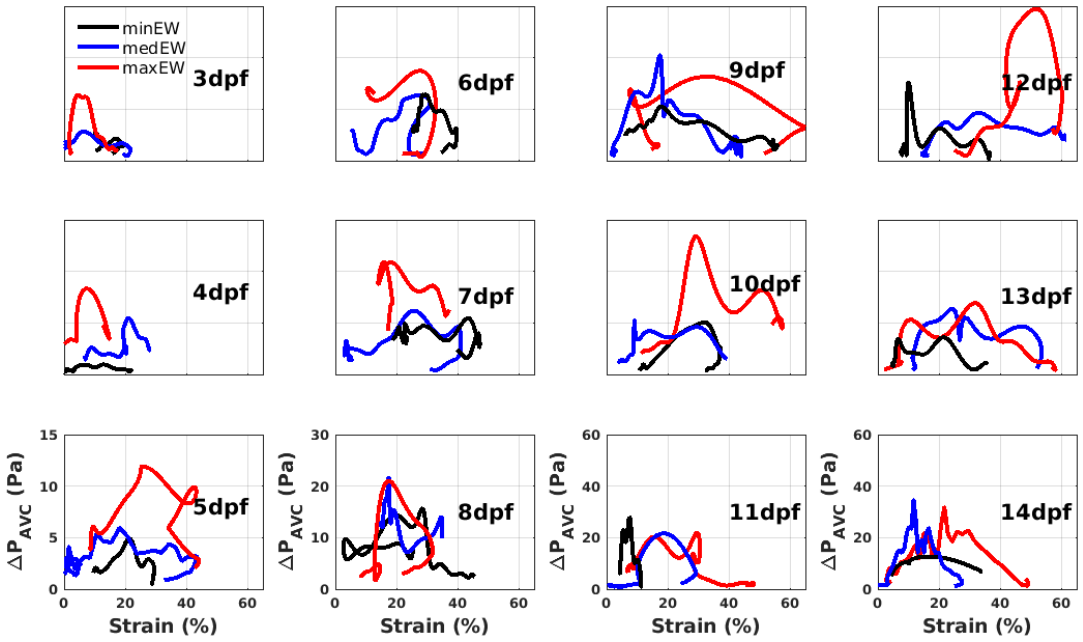

Figure 4-6: Pressure drop (ΔP_{AVC}) vs endocardial wall strain plots from 3 dpf to 14 dpf. Three curves in each dpf denote minimum EW (black curve), median EW (blue curve) and maximum EW (red curve). The y-axis limits for subplots in each column is same. The x-axis limits for all subplots are same.

under this ΔP_{AVC}-strain curve. EW obtained from this will have the unit Pa-% instead of the conventional unit of N-m. The three curves in a subplot are selected according to a minimum (black curve), maximum (red curve) and median EW (blue curve) measured at each dpf. The y-axis limits for the subplots in each column are identical. As seen in 3 dpf to 5 dpf, a smaller area curve denotes that the contractility of the endocardial wall is lower than the larger area curves (6 dpf to 14 dpf). The curve shapes are noisy and inconsistent owing to two reasons: a) the reference (end of ventricle systole) time may have been slightly different in each sample. b) the velocity gradients calculated from the vectors of µPIV analysis are susceptible to 10% error for 1% error in velocity measurements. These errors may show up as "noisy" plots. The maximum strain occurs when the ventricle expansion is the largest while the maximum pressure drop occurs after the peak flow velocity crosses the AVC.

4.3.6 Peak EW, peak ΔP at AVC, OFT and peak diastolic strain measurement

The peak values of EW, ΔP_{AVC}, ΔP_{OFT} and diastolic strain have been plotted against developing medaka age progression in **Figure 4-7**. The mean across 4-5 samples in each dpf is plotted with the standard deviation being displayed by the error bars. The (***) over each dpf shows that the

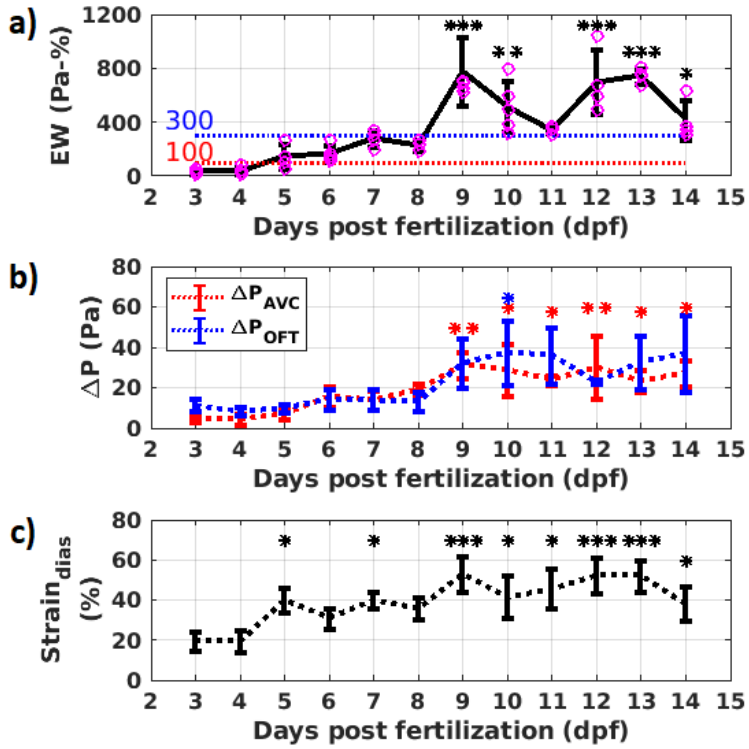

Figure 4-7: Variation of a) Peak EW, b) peak ΔP at AVC and OFT and c) peak diastolic ventricle strain with medaka age progression. The * in the plots denote statistical significance compared to the control values in 3 dpf. * denote p<0.0001, ** denote p<0.001, and * denote p < 0.05.**

mean is statistically significantly different when compared to the mean value at 3 dpf. In **Figure 4-7c**, the peak strain during ventricle diastole ($Strain_{dias}$) is low at 3dpf and 4 dpf. It fluctuates within a broad range from 5 dpf and 14 dpf with high variability in each dpf. So, it is not a metric that can accurately distinguish ventricle wall remodeling stag tes. In **Figure 4-7b**, peak values of ΔP_{AVC} and ΔP_{OFT} show a well-defined increase from pre-hatch (3dpf - 8 dpf) to post-hatch stages (9 dpf – 14 dpf). The variability across the samples is high in the post-hatch stages. **Figure 4-7a** shows a well-defined progression of EW with developing fish age. EW at 3 dpf and 4 dpf are below 100 Pa-%. EW at 5 dpf and 6 dpf are below 300 Pa-% while the EW at 9 dpf, 10 dpf, 12 dpf and 13 dpf are above 300 Pa-%. The sudden reduction of EW and ΔP_{AVC} at 11 dpf with little variability can be attributed to unknown developmental changes occurring at AVC. A larger sample size is required to substantiate this observation. Overall, EW is the metric that best demarcates between the linear heart stage (< 100 Pa-%) , cardiac looped chamber stage (< 300 Pa-%), and the fully formed chamber stage (> 300 Pa-%).

4.4 Discussion

Non-invasive pressure drop measurements are reported for the first time across the AVC and OFT regions of a developing medaka during the linear heart tube stages, cardiac looping end stages and fully developed chamber stages. Retrograde flows were observed in pressure contour and velocity vector plots at AVC during 8 dpf and 13 dpf and at OFT during 13 dpf (**Figure 4-1, Figure 4-2**) . The pumping mechanics at the AVC and OFT during 3dpf are significantly different as observed from the pressure contours. The AVC is not much narrow at 3dpf due to which the pressure drop across the chambers are small. With age progression the AVC starts narrowing and the ΔP_{AVC} increases. The OFT is initially positioned such that during ventricle systole a strong suction force draws blood directly from the atrial inlet. Due to this large ΔP_{OFT} , a high flow velocity is observed at 3dpf. At 6dpf, the appreciable increase in both ΔP_{AVC} and ΔP_{OFT} can be attributed to similar filling mechanics of flow into a compressed closed vessel, like a balloon. This increase was observed in peak-WSS values shown in the previous work with this data (254). The balloon-filling mechanics continues in the successive embryonic ages. After hatching, ΔP_{AVC} and ΔP_{OFT} are appreciable higher than their pre-hatch measures. Due to decompression of the organs, the ventricle rapidly increases in size after hatching. This leads to a stronger pressure drop when the ventricle expands (ΔP_{AVC}) or contracts (ΔP_{OFT}). The non-dimensional pressure drop is useful to compare across stages within the same species and with other species where the length and time scales are different (161). The pressure measurement technique can also be used for three-dimensional images. When combined with physical pressure readings, this can predict the absolute pressure distribution in the medaka heart in future studies.

Strain measurements have not been explored earlier in medaka heart. Our measurement technique avoids the lack of repeatability associated with manual segmentation of cardiac walls. Instead, using velocity gradients to detect wall edges circumvents the expertise required to differentiate between pericardium and endocardium in strain calculated from ultrasound scans. The results show that the ventricle deformation is much less in the linear heart tube stage at 3 dpf and 4 dpf. This is attributed to the lack of cardiomyocytes that start populating significantly after 5 dpf (166). The peak diastolic strain measured earlier in the normal zebrafish heart was around 40% at 50 hpf, 75 hpf and 100 hpf (181) which could not differentiate between the three developmental stages. The %-strain is still a useful metric to compare the contractility in different segments of the cardiac wall and can identify disease regions on the cardiac wall.

The EW is a metric that we have introduced through this work in the teleost cardiac mechanics literature. The EW has shown sufficient demarcation (denoted by the p-values in **Table** 4-2) between the three main developmental stages of the medaka heart but needs to be validated with a higher number of samples at each dpf. A lower EW suggests a stiffer ventricle with low flowrates through the AVC. The shape of the ΔP_{AVC}-strain curve at different stages offers insight into the pumping mechanism and time scales of ventricle expansion, relaxation, and contraction. These can be quantified in future studies with more samples. A flat-topped curve (**Figure 4-6**) indicates that the ΔP_{AVC} is caused by the positive pressure in the atrium only with no contribution from the ventricle expansion. A bell-shaped curve, on the other hand, includes the contribution of ventricle expansion to the ΔP_{AVC}. The EW calculated from these curves is indirectly related to the metabolic demand of the heart and can be further developed into a diagnostic tool that can differentiate normal hearts from diseased hearts in humans.

4.5 Limitations

The main limitation of this study is that there are only four/five samples per dpf. Including more samples would require the investment of sufficient time and resources but would increase accuracy. The limited spatial resolution near the endocardial wall introduced errors in the velocity gradient measurements that propagated in both pressure and strain calculations. The orientation of the heart during imaging can be different for different samples at each dpf. In some orientations, the out-of-plane velocity vectors are larger in number at the AVC. This may again bias the final pressure and strain calculations. The EW is calculated from an open ΔP_{AVC}-strain loop because the pressure cannot be calculated when the AVC is closed. Despite these limitations, both the pressure drop at AVC, OFT and the EW show a gradual increase with developing medaka age progression that has not been reported yet.

4.6 Conclusion

To our knowledge, this study is the first to report peak pressure drop values in the AVC and OFT of a developing Japanese medaka from 3 dpf (onset of blood circulation) to 14 dpf. The viscosity used in the pressure calculations was calculated at each dpf instead of assuming a constant value. Flow reversals observed for the first time in the valveless narrow cushion regions of the medaka

ventricle inflow and outflow are validated by negative pressure drop towards the end of ventricle diastole during 8 dpf and 13 dpf. A non-intrusive metric EW is introduced to differentiate between the linear heart tube stages, end of cardiac looping stages and the fully developed chambers in the post-hatch stages.

Longitudinal studies of cardiovascular development relating the pressure drop to cardiac developmental landmarks are scarce in all vertebrates. An important insight gained from this longitudinal analysis of flow and tissue mechanics variation with age is the different pumping mechanisms of the heart at different dpf. At 3dpf, the pumping mechanics at the AVC was different from that of the OFT. This baseline framework can be further tested by probing the flow-tissue mechanics evolution in higher vertebrate models.

4.7 Methods

Details about the Japanese Medaka Husbandry, Data Acquisition and μPIV analysis in the medaka heart have already been discussed in the previous work using this data (254).

4.7.1 Velocity reconstruction across the AVC and the OFT

The medaka heart has two small connector regions that reduce in area as the fish ages from 3 dpf to 14 dpf. One is the AVC [diameter: 6-10 μm] joining the atrium and ventricle and the other is the OFT [diameter : 10-14 μm] connecting the ventricle and the BA. The high velocities at AVC and OFT at certain heart cycle phases could not be accurately captured due to increased noise or signal dropout in those frames. So, using the velocity information of a neighboring region in the ventricle/atrium and applying the conservation of mass principle as shown in Equation 4-1, the velocity vectors were reconstructed in these areas.

$$\nabla . \mathbf{u} = 0 \qquad \textbf{Equation 4-1}$$

4.7.2 Pressure analysis of the cardiac chambers

The pressure field in the cardiac chambers for a heart cycle was obtained by integrating Equation 4-2 for the known phase averaged velocity field. Velocity gradients were calculated using a high accuracy gradient calculation technique namely the Compact-Richardson method (234) in accordance with second-order polynomial fitting done in previous studies (154, 161).

$$\nabla P = -\rho(\frac{\partial \mathbf{u}}{\partial t} + \mathbf{u}.\nabla \mathbf{u}) + \mu(\nabla^2 \mathbf{u}) \qquad \textbf{Equation 4-2}$$

The pressure was then integrated along multiple line paths in the cardiac field assuming a zero value at a fixed node on the boundary. Integration paths were averaged to smooth out uncertainties in the velocity field. The average value was updated in successive iterations until the pressure residual converges to a value of 1x 10^{-3}. A second-order trapezoidal rule was used for spatial integration. The dependence of this omni-directional method on grid resolution, sampling rate, velocity field error levels, and off axis recording was explored extensively for PIV measured velocity fields in previous work from our lab (255). Blood dynamic viscosity (μ) was calculated for each sample at each dpf using the hematocrit and shear rate information as described in previous work (254). Owing to small Re (<<1) and Wo (<<1) the first two terms on the right-hand side of equation X are negligible. So pressure (P) is non-dimensionalized by the product of heart rate and blood dynamic viscosity (HR*μ) as shown in (161)

4.7.3 Strain analysis of the ventricle wall

Velocity field measurements are used to calculate the deformation gradient tensor F for the entire ventricle. The end of ventricle systole is used as the reference time (or frame number) against which the deformation of the ventricle at other time points in the heart cycle is calculated. The Strain is then calculated from F according to the equation below

$$\boldsymbol{F} = \begin{bmatrix} \frac{\partial u}{\partial x} & \frac{\partial u}{\partial y} \\ \frac{\partial v}{\partial x} & \frac{\partial v}{\partial y} \end{bmatrix}; \quad Strain = \frac{1}{2}\mathrm{F}^T F - I \qquad \textbf{Equation 4-3}$$

Where T denotes the transpose of a matrix and I is the identity matrix. Endocardial wall locations were detected from the velocity gradient images by using the Canny edge detection scheme to identify the coordinates of peak gradient locations. The lagrangaian strain was extracted at the ventricle wall locations to show the spatial variation of strain along the ventricle wall (**Figure 4-5a**). At each time point, three maximum strain values were further extracted and averaged to generate peak endocardial wall strain variation along a cardiac cycle (**Figure 4-5b**).

4.7.4 EW measurement of the ventricle

The endocardial work (EW) is measured by calculating the area under the curve of a ΔP_{AVC}-strain plot as shown in **Figure 4-6**. The area calculation is performed in Matlab by implementing a numerical trapezoidal integration technique. The ΔP_{AVC}-strain plot is not a closed loop because the ΔP information is available only for the diastolic cycle of the ventricle when the AVC is open. The EW measure reflects the combined effect of changes in ΔP_{AVC} and strain on the effective contractility of the endocardial wall.

4.8 Statistical Analysis

Statistical significance was tested for all the cardiac function and geometry parameters using Tukey-Kramer Honest Significant Difference (HSD) test. The p-values that denote difference of mean values of the parameters (peak strain rate at ventricle diastole, dimensional and non-dimensional peak pressure drop at AVC and OFT, endocardial work) between a pair of dpf are listed in

Table 4-2.

Table 4-2: p-values from Tukey Kramer HSD tests comparing Peak $Strain_{dias}$, peak ΔP_{AVC}, peak ΔP_{OFT}, peak $\Delta P_{AVC}/(HR*\mu)$, Peak $\Delta P_{OFT}/(HR*\mu)$ and EW between each pair of dpfs. n=4-5 at each dpf. * denotes p<0.0001. ** denotes p<0.001. * denotes p<0.05.**

p-values							
dpf		**Peak $Strain_{dias}$**	**Peak ΔP_{AVC}**	**Peak ΔP_{OFT}**	**Peak $\frac{\Delta P_{AVC}}{HR*\mu}$**	**Peak $\frac{\Delta P_{OFT}}{HR*\mu}$**	**EW**
3	4	1.0	1.0	1.0	1.0	1.0	1.0
3	5	0.0303*	1.0	1.0	1.0	1.0	0.9858
3	6	0.5798	0.6091	1.0	0.2685	1.0	0.9258
3	7	0.0168*	0.8229	1.0	0.8459	1.0	0.28
3	8	0.1596	0.3828	1.0	0.4985	1.0	0.7129
3	9	<0.0001***	0.0004**	0.3816	0.0026*	0.9496	<0.0001***
3	10	0.0072*	0.0018*	0.0403*	0.0044*	0.0172*	0.0001**
3	11	0.0016*	0.0458*	0.0633	0.3054	0.3856	0.1152
3	12	<0.0001***	0.0008**	0.9067	0.0041*	0.9946	<0.0001***
3	13	<0.0001***	0.0327*	0.1715	0.4106	0.8427	<0.0001***
3	14	0.0414*	0.0088*	0.141	0.2771	0.8272	0.0077*
4	5	0.0289*	1.0	1.0	1.0	1.0	0.9875
4	6	0.5671	0.5836	0.9999	0.2099	0.9984	0.9321
4	7	0.0159*	0.8028	0.9999	0.7771	1.0	0.29
4	8	0.1538	0.3633	1.0	0.4255	1.0	0.7244
4	9	<0.0001***	0.0004**	0.2725	0.0018*	0.7787	<0.0001***
4	10	0.0069*	0.0016*	0.0275*	0.0029*	0.007*	0.0001**

4	11	0.0015*	0.0418*	0.0427*	0.2447	0.1875	0.12
4	12	<0.0001***	0.0007**	0.7847	0.0027*	0.914	<0.0001***

Table 4-2 continued

4	13	<0.0001***	0.0295*	0.1157	0.3337	0.5699	<0.0001***
4	14	0.0394*	0.008*	0.0955	0.2203	0.5791	0.0082*
5	6	0.9023	0.9352	1.0	0.6741	0.9993	1.0
5	7	1.0	0.9894	1.0	0.9918	1.0	0.9586
5	8	0.9999	0.7437	1.0	0.8364	1.0	0.9994
5	9	0.4924	0.0051*	0.2853	0.0235*	0.7975	<0.0001***
5	10	1.0	0.0176*	0.0239*	0.0358*	0.005*	0.0099*
5	11	0.998	0.2067	0.0384*	0.6919	0.174	0.7383
5	12	0.5874	0.0091*	0.8172	0.0338*	0.9276	<0.0001***
5	13	0.5969	0.1771	0.1116	0.8174	0.5731	<0.0001***
5	14	1.0	0.0573	0.096	0.6579	0.5919	0.2099
6	7	0.8651	1.0	1.0	0.9979	1.0	0.9825
6	8	0.9988	1.0	1.0	1.0	1.0	0.9999
6	9	0.0077*	0.1566	0.7532	0.7971	0.9991	<0.0001***
6	10	0.7039	0.3659	0.2505	0.879	0.1742	0.0099*
6	11	0.3118	0.9367	0.3308	1.0	0.863	0.8092
6	12	0.0118*	0.2377	0.9966	0.8691	1.0	<0.0001***
6	13	0.0124*	0.9339	0.5741	1.0	0.9954	<0.0001***
6	14	0.9669	0.6308	0.44	1.0	0.9884	0.2436
7	8	0.9999	0.9982	1.0	0.9996	1.0	1.0
7	9	0.4004	0.0710	0.7469	0.2249	0.9865	0.0001**
7	10	1.0	0.1948	0.2452	0.3062	0.0806	0.3026
7	11	0.9968	0.8005	0.3244	0.9973	0.6619	1.0
7	12	0.4966	0.1154	0.9963	0.294	0.9994	0.0038*
7	13	0.5066	0.7839	0.5662	0.9999	0.9562	0.0009**
7	14	1.0	0.4136	0.4334	0.9957	0.9347	0.9493
8	9	0.1453	0.7349	0.6883	0.895	0.9481	0.0001**
8	10	0.9978	0.9226	0.2007	0.942	0.0419*	0.1829
8	11	0.8973	0.9999	0.2704	1.0	0.482	0.996
8	12	0.195	0.8357	0.9915	0.9366	0.993	0.0026*
8	13	0.2006	0.9999	0.4962	1.0	0.8683	0.0007**
8	14	1.0	0.9831	0.3761	1.0	0.8414	0.8133
9	10	0.5924	1.0	1.0	1.0	0.7213	0.1144
9	11	0.9755	0.9739	1.0	0.8852	0.9999	0.0036*
9	12	1.0	1.0	0.9919	1.0	1.0	0.9988
9	13	1.0	0.9422	1.0	0.6395	1.0	1.0
9	14	0.2241	0.9999	1.0	0.9062	1.0	0.0110*
10	11	0.9998	0.9991	1.0	0.9388	0.9499	0.8369
10	12	0.6919	1.0	0.6934	1.0	0.205	0.6635
10	13	0.7015	0.9967	0.9999	0.7473	0.5776	0.3483
10	14	1.0	1.0	1.0	0.9524	0.8913	0.9923
11	12	0.9899	0.9927	0.8028	0.9327	0.9537	0.0515
11	13	0.9909	1.0	1.0	1.0	0.9998	0.0168*
11	14	0.9716	1.0	1.0	1.0	1.0	0.9999
12	13	1.0	0.9805	0.9651	0.7332	0.9999	1.0
12	14	0.2957	1.0	0.8737	0.9473	0.9993	0.1496
13	14	0.3036	0.9999	1.0	1.0	1.0	0.0514

REFERENCES

1. Mariotto AB, Yabroff KR, Shao Y, Feuer EJ, Brown ML. Projections of the cost of cancer care in the United States: 2010-2020. Journal of the National Cancer Institute. 2011;103(2):117-28.
2. Nie S, Xing Y, Kim GJ, Simons JW. Nanotechnology applications in cancer. Annual review of biomedical engineering. 2007;9:257-88.
3. Haley B, Frenkel E. Nanoparticles for drug delivery in cancer treatment. Urologic oncology. 2008;26(1):57-64.
4. Arruebo M, Fernández-Pacheco R, Ibarra MR, Santamaría J. Magnetic nanoparticles for drug delivery. Nano today. 2007;2(3):22-32.
5. Wang AZ, Langer R, Farokhzad OC. Nanoparticle delivery of cancer drugs. Annual review of medicine. 2012;63:185-98.
6. Matsumura Y, Maeda H. A new concept for macromolecular therapeutics in cancer chemotherapy: mechanism of tumoritropic accumulation of proteins and the antitumor agent smancs. Cancer research. 1986;46(12 Pt 1):6387-92.
7. Zervantonakis IK, Chung S, Sudo R, Zhang M, Charest JL, Kamm RD. Concentration gradients in microfluidic 3D matrix cell culture systems. International Journal of Micro-Nano Scale Transport. 2010;1(1):27-36.
8. Shipley RJ, Chapman SJ. Multiscale modelling of fluid and drug transport in vascular tumours. Bulletin of mathematical biology. 2010;72(6):1464-91.
9. Baxter LT, Jain RK. Transport of fluid and macromolecules in tumors. I. Role of interstitial pressure and convection. Microvascular research. 1989;37(1):77-104.
10. Pozrikidis C, Farrow DA. A model of fluid flow in solid tumors. Annals of biomedical engineering. 2003;31(2):181-94.
11. Sefidgar M, Soltani M, Raahemifar K, Sadeghi M, Bazmara H, Bazargan M, et al. Numerical modeling of drug delivery in a dynamic solid tumor microvasculature. Microvascular research. 2015;99:43-56.
12. Penta R, Ambrosi D, Quarteroni A. Multiscale homogenization for fluid and drug transport in vascularized malignant tissues. Mathematical Models and Methods in Applied Sciences. 2015;25(01):79-108.
13. Schuff MM, Gore JP, Nauman EA. A mixture theory model of fluid and solute transport in the microvasculature of normal and malignant tissues. I. Theory. Journal of mathematical biology. 2013;66(6):1179-207.
14. Schuff MM, Gore JP, Nauman EA. A mixture theory model of fluid and solute transport in the microvasculature of normal and malignant tissues. II: Factor sensitivity analysis, calibration, and validation. Journal of mathematical biology. 2013;67(6-7):1307-37.
15. Taylor DG, Bert JL, Bowen BD. A mathematical model of interstitial transport. II. Microvascular exchange in mesentery. Microvascular research. 1990;39(3):279-306.
16. Taylor DG, Bert JL, Bowen BD. A mathematical model of interstitial transport. I. Theory. Microvascular research. 1990;39(3):253-78.

17. Victorino GP, Newton CR, Curran B. Effect of hypertonic saline on microvascular permeability in the activated endothelium. The Journal of surgical research. 2003;112(1):79-83.
18. Chou CY, Chang WI, Horng TL, Lin WL. Numerical modeling of nanodrug distribution in tumors with heterogeneous vasculature. PloS one. 2017;12(12):e0189802.
19. Stylianopoulos T, Economides EA, Baish JW, Fukumura D, Jain RK. Towards Optimal Design of Cancer Nanomedicines: Multi-stage Nanoparticles for the Treatment of Solid Tumors. Annals of biomedical engineering. 2015;43(9):2291-300.
20. Goins AB, Sanabria H, Waxham MN. Macromolecular crowding and size effects on probe microviscosity. Biophysical journal. 2008;95(11):5362-73.
21. Armstrong JK, Wenby RB, Meiselman HJ, Fisher TC. The hydrodynamic radii of macromolecules and their effect on red blood cell aggregation. Biophysical journal. 2004;87(6):4259-70.
22. Ekani-Nkodo A, Fygenson DK. Size exclusion and diffusion of fluoresceinated probes within collagen fibrils. Physical review E, Statistical, nonlinear, and soft matter physics. 2003;67(2 Pt 1):021909.
23. Ballard K, Perl W. Osmotic reflection coefficients of canine subcutaneous adipose tissue endothelium. Microvascular research. 1978;16(2):224-36.
24. Michel CC. Filtration coefficients and osmotic reflexion coefficients of the walls of single frog mesenteric capillaries. The Journal of physiology. 1980;309:341-55.
25. Yuan F, Salehi HA, Boucher Y, Vasthare US, Tuma RF, Jain RK. Vascular permeability and microcirculation of gliomas and mammary carcinomas transplanted in rat and mouse cranial windows. Cancer research. 1994;54(17):4564-8.
26. Baxter LT, Jain RK. Vascular permeability and interstitial diffusion in superfused tissues: a two-dimensional model. Microvascular research. 1988;36(1):108-15.
27. Baxter LT, Jain RK, Svensjo E. Vascular permeability and interstitial diffusion of macromolecules in the hamster cheek pouch: effects of vasoactive drugs. Microvascular research. 1987;34(3):336-48.
28. Dreher MR, Liu W, Michelich CR, Dewhirst MW, Yuan F, Chilkoti A. Tumor vascular permeability, accumulation, and penetration of macromolecular drug carriers. Journal of the National Cancer Institute. 2006;98(5):335-44.
29. Nugent LJ, Jain RK. Extravascular diffusion in normal and neoplastic tissues. Cancer research. 1984;44(1):238-44.
30. Maroudas A. Distribution and diffusion of solutes in articular cartilage. Biophysical journal. 1970;10(5):365-79.
31. Fox JR, Wayland H. Interstitial diffusion of macromolecules in the rat mesentery. Microvascular research. 1979;18(2):255-76.
32. Leddy HA, Guilak F. Site-specific molecular diffusion in articular cartilage measured using fluorescence recovery after photobleaching. Annals of biomedical engineering. 2003;31(7):753-60.
33. Nakamura Y, Wayland H. Macromolecular transport in the cat mesentery. Microvascular research. 1975;9(1):1-21.
34. Heldin CH, Rubin K, Pietras K, Ostman A. High interstitial fluid pressure - an obstacle in cancer therapy. Nature reviews Cancer. 2004;4(10):806-13.

35. Lipowsky HH, Zweifach BW. Methods for the simultaneous measurement of pressure differentials and flow in single unbranched vessels of the microcirculation for rheological studies. Microvascular research. 1977;14(3):345-61.
36. Zweifach BW, Lipowsky HH. Quantitative studies of microcirculatory structure and function. III. Microvascular hemodynamics of cat mesentery and rabbit omentum. Circulation research. 1977;41(3):380-90.
37. Asaishi K, Endrich B, Gotz A, Messmer K. Quantitative analysis of microvascular structure and function in the amelanotic melanoma A-Mel-3. Cancer research. 1981;41(5):1898-904.
38. Stohrer M, Boucher Y, Stangassinger M, Jain RK. Oncotic pressure in solid tumors is elevated. Cancer research. 2000;60(15):4251-5.
39. Jain RK. Transport of molecules in the tumor interstitium: a review. Cancer research. 1987;47(12):3039-51.
40. Boucher Y, Kirkwood JM, Opacic D, Desantis M, Jain RK. Interstitial hypertension in superficial metastatic melanomas in humans. Cancer research. 1991;51(24):6691-4.
41. Nathanson SD, Nelson L. Interstitial fluid pressure in breast cancer, benign breast conditions, and breast parenchyma. Annals of surgical oncology. 1994;1(4):333-8.
42. Serpooshan V, Julien M, Nguyen O, Wang H, Li A, Muja N, et al. Reduced hydraulic permeability of three-dimensional collagen scaffolds attenuates gel contraction and promotes the growth and differentiation of mesenchymal stem cells. Acta biomaterialia. 2010;6(10):3978-87.
43. O'Connor SW, Bale WF. Accessibility of circulating immunoglobulin G to the extravascular compartment of solid rat tumors. Cancer research. 1984;44(9):3719-23.
44. Gullino PM, Grantham FH, Smith SH. The Interstitial Water Space of Tumors. Cancer research. 1965;25:727-31.
45. Appelgren L, Peterson HI, Rosengren B. Vascular and extravascular spaces in two transplantable tumors of the rat. Bibliotheca anatomica. 1973;12:504-10.
46. Less JR, Skalak TC, Sevick EM, Jain RK. Microvascular architecture in a mammary carcinoma: branching patterns and vessel dimensions. Cancer research. 1991;51(1):265-73.
47. Smaje L, Zweifach BW, Intaglietta M. Micropressures and capillary filtration coefficients in single vessels of the cremaster muscle of the rat. Microvascular research. 1970;2(1):96-110.
48. Edel MJ, Robbins PD, Papadimitriou JM, D'Antuono MF, Harvey JM, Mitchel CA, et al. Assessment of vascularity in breast carcinoma by computer-assisted video analysis (CAVA) and its association with axillary lymph node status. Breast cancer research and treatment. 1998;47(1):17-27.
49. Hilmas DE, Gillette EL. Morphometric analyses of the microvasculature of tumors during growth and after x-irradiation. Cancer. 1974;33(1):103-10.
50. Gerlowski LE, Jain RK. Microvascular permeability of normal and neoplastic tissues. Microvascular research. 1986;31(3):288-305.
51. Horak ER, Leek R, Klenk N, LeJeune S, Smith K, Stuart N, et al. Angiogenesis, assessed by platelet/endothelial cell adhesion molecule antibodies, as indicator of node metastases and survival in breast cancer. Lancet. 1992;340(8828):1120-4.
52. Yahara T, Koga T, Yoshida S, Nakagawa S, Deguchi H, Shirouzu K. Relationship between microvessel density and thermographic hot areas in breast cancer. Surgery today. 2003;33(4):243-8.
53. Wells WA, Daghlian CP, Tosteson TD, Grove MR, Poplack SP, Knowlton-Soho S, et al. Analysis of the microvasculature and tissue type ratios in normal vs. benign and malignant

breast tissue. Analytical and quantitative cytology and histology / the International Academy of Cytology [and] American Society of Cytology. 2004;26(3):166-74.
54. Fait E, Malkusch W, Gnoth S, Dimitropoulou C, Gaumann A, Kirkpatrick C, et al. Microvascular patterns of the human large intestine: morphometric studies of vascular parameters in corrosion casts. Scanning Microsc. 1998;12(4):641-51.
55. Konerding MA, Fait E, Gaumann A. 3D microvascular architecture of pre-cancerous lesions and invasive carcinomas of the colon. British journal of cancer. 2001;84(10):1354-62.
56. Lu Y, Michel CC, Wang W. Inert gas clearance from tissue by co-currently and counter-currently arranged microvessels. Journal of applied physiology. 2012;113(3):487-97.
57. Malam Y, Loizidou M, Seifalian AM. Liposomes and nanoparticles: nanosized vehicles for drug delivery in cancer. Trends in pharmacological sciences. 2009;30(11):592-9.
58. Yang H-C, Hon M-H. The effect of the molecular weight of chitosan nanoparticles and its application on drug delivery. Microchemical Journal. 2009;92(1):87-91.
59. A. Ozkan NG, P.J. Hoopes, M.N. Rylander. In Vitro Vascularized Liver and Tumor Tissue Microenvironments on a Chip for Dynamic Determination of Nanoparticle Transport and Toxicity. Biotechnology and Bioengineering. 2018.
60. R. Michna MG, A. Ozkan, M.R.Dewitt, M.N. Rylander. Vascularized microfluidic platforms to mimic the tumor microenvironment. Biotechnology and Bioengineering. 2018.
61. Baxter LT, Jain RK. Transport of fluid and macromolecules in tumors. II. Role of heterogeneous perfusion and lymphatics. Microvascular research. 1990;40(2):246-63.
62. Ji RC. Lymphatic endothelial cells, tumor lymphangiogenesis and metastasis: New insights into intratumoral and peritumoral lymphatics. Cancer metastasis reviews. 2006;25(4):677-94.
63. Pisano M, Triacca V, Barbee KA, Swartz MA. An in vitro model of the tumor-lymphatic microenvironment with simultaneous transendothelial and luminal flows reveals mechanisms of flow enhanced invasion. Integrative biology : quantitative biosciences from nano to macro. 2015;7(5):525-33.
64. Swartz MA, Lund AW. Lymphatic and interstitial flow in the tumour microenvironment: linking mechanobiology with immunity. Nature reviews Cancer. 2012;12(3):210-9.
65. Shayan R, Achen MG, Stacker SA. Lymphatic vessels in cancer metastasis: bridging the gaps. Carcinogenesis. 2006;27(9):1729-38.
66. Alimohamadi H, Imani M, Shojaeizadeh M. Numerical Simulation Of Porosity Effect On Blood Flow Pattern And Atherosclerotic Plaques Temperature. 2014.
67. Cheema TA, Kim GM, Lee CY, Hong JG, Kwak MK, Park CW. Characteristics of blood vessel wall deformation with porous wall conditions in an aortic arch. Applied Rheology. 2014;24(24590):1-8.
68. McGeown JG. Passing on the legacy: teaching capillary filtration and developing presentation skills using classic papers. Advances in physiology education. 2006;30(3):108-12.
69. Chen J-S, Liu C-W. Generalized analytical solution for advection-dispersion equation in finite spatial domain with arbitrary time-dependent inlet boundary condition. Hydrology and Earth System Sciences. 2011;15(8):2471.
70. Van Genuchten MT, Alves W. Analytical solutions of the one-dimensional convective-dispersive solute transport equation. United States Department of Agriculture, Economic Research Service; 1982.

71. Chapman SJ, Shipley RJ, Jawad R. Multiscale modeling of fluid transport in tumors. Bulletin of mathematical biology. 2008;70(8):2334-57.
72. Cheng MJ, Prabakaran P, Kumar R, Sridhar S, Ebong EE. Synthesis of Functionalized 10-nm Polymer-coated Gold Particles for Endothelium Targeting and Drug Delivery. Journal of visualized experiments : JoVE. 2018(131).
73. Lu J, Yang S, Ng KM, Su C-H, Yeh C-S, Wu Y-N, et al. Solid-state synthesis of monocrystalline iron oxide nanoparticle based ferrofluid suitable for magnetic resonance imaging contrast application. Nanotechnology. 2006;17(23):5812.
74. Wu W, Wu Z, Yu T, Jiang C, Kim WS. Recent progress on magnetic iron oxide nanoparticles: synthesis, surface functional strategies and biomedical applications. Science and technology of advanced materials. 2015;16(2):023501.
75. Antoine E, Buchanan C, Fezzaa K, Lee WK, Rylander MN, Vlachos P. Flow measurements in a blood-perfused collagen vessel using x-ray micro-particle image velocimetry. PloS one. 2013;8(11):e81198.
76. Buchanan CF, Voigt EE, Szot CS, Freeman JW, Vlachos PP, Rylander MN. Three-dimensional microfluidic collagen hydrogels for investigating flow-mediated tumor-endothelial signaling and vascular organization. Tissue engineering Part C, Methods. 2014;20(1):64-75.
77. Buchanan CF, Verbridge SS, Vlachos PP, Rylander MN. Flow shear stress regulates endothelial barrier function and expression of angiogenic factors in a 3D microfluidic tumor vascular model. Cell adhesion & migration. 2014;8(5):517-24.
78. Antoine EE, Vlachos PP, Rylander MN. Tunable collagen I hydrogels for engineered physiological tissue micro-environments. PloS one. 2015;10(3):e0122500.
79. Antoine EE. Mechanics and transport characterization of bioengineered tissue microenvironment platforms: Virginia Tech; 2014.
80. Cross VL, Zheng Y, Won Choi N, Verbridge SS, Sutermaster BA, Bonassar LJ, et al. Dense type I collagen matrices that support cellular remodeling and microfabrication for studies of tumor angiogenesis and vasculogenesis in vitro. Biomaterials. 2010;31(33):8596-607.
81. Moreno-Arotzena O, Meier JG, Del Amo C, Garcia-Aznar JM. Characterization of Fibrin and Collagen Gels for Engineering Wound Healing Models. Materials. 2015;8(4):1636-51.
82. Nagueh SF, Appleton CP, Gillebert TC, Marino PN, Oh JK, Smiseth OA, et al. Recommendations for the evaluation of left ventricular diastolic function by echocardiography. Journal of the American Society of Echocardiography. 2009;22(2):107-33.
83. Claessens TE, De Sutter J, Vanhercke D, Segers P, Verdonck PR. New echocardiographic applications for assessing global left ventricular diastolic function. Ultrasound in medicine & biology. 2007;33(6):823-41.
84. Greenberg NL, Vandervoort PM, Thomas JD. Instantaneous diastolic transmitral pressure differences from color Doppler M mode echocardiography. Am J Physiol-Heart Circul Physiol. 1996;271(4):H1267-H76.
85. Yotti R, Bermejo J, Desco MM, Antoranz JC, Rojo-Alvarez JL, Cortina C, et al. Doppler-derived ejection intraventricular pressure gradients provide a reliable assessment of left ventricular systolic chamber function. Circulation. 2005;112(12):1771-9.
86. Tsujinaga S, Iwano H, Sarashina M, Hayashi T, Murayama M, Ichikawa A, et al. Diastolic Intra-Left Ventricular Pressure Difference During Exercise: Strong Determinant and

Predictor of Exercise Capacity in Patients With Heart Failure. Journal of cardiac failure. 2019;25(4):268-77.
87. Iwano H, Kamimura D, Fox E, Hall M, Vlachos P, Little WC. Altered spatial distribution of the diastolic left ventricular pressure difference in heart failure. Journal of the American Society of Echocardiography : official publication of the American Society of Echocardiography. 2015;28(5):597-605 e1.
88. Vlachos PP, Niebel CL, Chakraborty S, Pu M, Little WC. Calculating intraventricular pressure difference using a multi-beat spatiotemporal reconstruction of color m-mode echocardiography. Annals of biomedical engineering. 2014;42(12):2466-79.
89. Londono-Hoyos FJ, Swillens A, Van Cauwenberge J, Meyers B, Koppula MR, Vlachos P, et al. Assessment of methodologies to calculate intraventricular pressure differences in computational models and patients. Medical & biological engineering & computing. 2018;56(3):469-81.
90. Charonko JJ, Kumar R, Stewart K, Little WC, Vlachos PP. Vortices formed on the mitral valve tips aid normal left ventricular filling. Annals of biomedical engineering. 2013;41(5):1049-61.
91. Sessoms MW, Lisauskas J, Kovacs SJ. The left ventricular color M-mode Doppler flow propagation velocity V(p): in vivo comparison of alternative methods including physiologic implications. Journal of the American Society of Echocardiography : official publication of the American Society of Echocardiography. 2002;15(4):339-48.
92. Stewart KC, Kumar R, Charonko JJ, Ohara T, Vlachos PP, Little WC. Evaluation of LV Diastolic Function From Color M-Mode Echocardiography. JACC: Cardiovascular Imaging. 2011;4(1):37-46.
93. Brun P, Tribouilloy C, Duval AM, Iserin L, Meguira A, Pelle G, et al. LEFT-VENTRICULAR FLOW PROPAGATION DURING EARLY FILLING IS RELATED TO WALL RELAXATION - A COLOR M-MODE DOPPLER ANALYSIS. J Am Coll Cardiol. 1992;20(2):420-32.
94. Stugaard M, Risoe C, Ihlen H, Smiseth OA. INTRACAVITARY FILLING PATTERN IN THE FAILING LEFT-VENTRICLE ASSESSED BY COLOR M-MODE DOPPLER-ECHOCARDIOGRAPHY. J Am Coll Cardiol. 1994;24(3):663-70.
95. Rovner A, Smith R, Greenberg NL, Tuzcu EM, Smedira N, Lever HM, et al. Improvement in diastolic intraventricular pressure gradients in patients with HOCM after ethanol septal reduction. American Journal of Physiology - Heart and Circulatory Physiology. 2003;285(6):H2492-H9.
96. Aldroubi A, Unser M. Wavelets in medicine and biology: Routledge; 2017.
97. Addison PS. The illustrated wavelet transform handbook: introductory theory and applications in science, engineering, medicine and finance: CRC press; 2017.
98. Lin J, Qu L. FEATURE EXTRACTION BASED ON MORLET WAVELET AND ITS APPLICATION FOR MECHANICAL FAULT DIAGNOSIS. Journal of sound and vibration. 2000;234(1):135-48.
99. Knapp C, Carter G. The Generalized Correlation Method for Estimation of Time Delay. IEEE Trans Acous Speech Sig Proc. 1976;24(4):320-7.
100. Greenberg NL, Vandervoort PM, Firstenberg MS, Garcia MJ, Thomas JD. Estimation of diastolic intraventricular pressure gradients by Doppler M-mode echocardiography. Am J Physiol-Heart Circul Physiol. 2001;280(6):H2507-H15.

101. Feigenbaum H. Echocardiographic Chamber Quantification in the Era of Multimodality Imaging: Beware of Unintended Consequences. Journal of the American Society of Echocardiography : official publication of the American Society of Echocardiography. 2015;28(7):847-50.
102. Lang RM, Bierig M, Devereux RB, Flachskampf FA, Foster E, Pellikka PA, et al. Recommendations for Chamber Quantification: A Report from the American Society of Echocardiography's Guidelines and Standards Committee and the Chamber Quantification Writing Group, Developed in Conjunction with the European Association of Echocardiography, a Branch of the European Society of Cardiology. Journal of the American Society of Echocardiography. 2005;18(12):1440-63.
103. Rivas-Gotz C, Manolios M, Thohan V, Nagueh SF. Impact of left ventricular ejection fraction on estimation of left ventricular filling pressures using tissue Doppler and flow propagation velocity. American Journal of Cardiology. 2003;91(6):780-4.
104. Ohara T, Niebel CL, Stewart KC, Charonko JJ, Pu M, Vlachos PP, et al. Loss of adrenergic augmentation of diastolic intra-LV pressure difference in patients with diastolic dysfunction: evaluation by color M-mode echocardiography. JACC Cardiovascular imaging. 2012;5(9):861-70.
105. Little WC. Diastolic dysfunction beyond distensibility: adverse effects of ventricular dilatation. Circulation. 2005;112(19):2888-90.
106. Kane GC, Karon BL, Mahoney DW, Redfield MM, Roger VL, Burnett JC, Jr., et al. Progression of left ventricular diastolic dysfunction and risk of heart failure. Jama. 2011;306(8):856-63.
107. Smiseth OA. Evaluation of left ventricular diastolic function: state of the art after 35 years with Doppler assessment. Journal of echocardiography. 2018;16(2):55-64.
108. Mitter SS, Shah SJ, Thomas JD. A Test in Context: E/A and E/e' to Assess Diastolic Dysfunction and LV Filling Pressure. J Am Coll Cardiol. 2017;69(11):1451-64.
109. Pavlopoulos H, Nihoyannopoulos P. Abnormal segmental relaxation patterns in hypertensive disease and symptomatic diastolic dysfunction detected by strain echocardiography. Journal of the American Society of Echocardiography : official publication of the American Society of Echocardiography. 2008;21(8):899-906.
110. Kasner M, Gaub R, Sinning D, Westermann D, Steendijk P, Hoffmann W, et al. Global strain rate imaging for the estimation of diastolic function in HFNEF compared with pressure-volume loop analysis. European journal of echocardiography : the journal of the Working Group on Echocardiography of the European Society of Cardiology. 2010;11(9):743-51.
111. Wang J, Khoury DS, Thohan V, Torre-Amione G, Nagueh SF. Global diastolic strain rate for the assessment of left ventricular relaxation and filling pressures. Circulation. 2007;115(11):1376-83.
112. Iwano H, Kamimura D, Fox ER, Hall ME, Vlachos P, Little WC. Presence and Implication of Temporal Nonuniformity of Early Diastolic Left Ventricular Wall Expansion in Patients With Heart Failure. Journal of cardiac failure. 2016;22(12):945-53.
113. Iwano H, Pu M, Upadhya B, Meyers B, Vlachos P, Little WC. Delay of left ventricular longitudinal expansion with diastolic dysfunction: impact on load dependence of e' and longitudinal strain rate. Physiological reports. 2014;2(7).

114. Fernandes RM, Le Bihan D, Vilela AA, Barretto RBM, Santos ES, Assef JE, et al. Association between left atrial strain and left ventricular diastolic function in patients with acute coronary syndrome. Journal of echocardiography. 2019;17(3):138-46.
115. Singh A, Addetia K, Maffessanti F, Mor-Avi V, Lang RM. LA Strain for Categorization of LV Diastolic Dysfunction. JACC Cardiovasc Imaging. 2017;10(7):735-43.
116. Thomas L, Marwick TH, Popescu BA, Donal E, Badano LP. Left Atrial Structure and Function, and Left Ventricular Diastolic Dysfunction: JACC State-of-the-Art Review. J Am Coll Cardiol. 2019;73(15):1961-77.
117. Davies PF, Civelek M, Fang Y, Fleming I. The atherosusceptible endothelium: endothelial phenotypes in complex haemodynamic shear stress regions in vivo. Cardiovascular research. 2013;99(2):315-27.
118. Conway DE, Breckenridge MT, Hinde E, Gratton E, Chen CS, Schwartz MA. Fluid shear stress on endothelial cells modulates mechanical tension across VE-cadherin and PECAM-1. Current biology : CB. 2013;23(11):1024-30.
119. Tzima E, Irani-Tehrani M, Kiosses WB, Dejana E, Schultz DA, Engelhardt B, et al. A mechanosensory complex that mediates the endothelial cell response to fluid shear stress. Nature. 2005;437(7057):426-31.
120. Mahler GJ, Frendl CM, Cao Q, Butcher JT. Effects of shear stress pattern and magnitude on mesenchymal transformation and invasion of aortic valve endothelial cells. Biotechnol Bioeng. 2014;111(11):2326-37.
121. Heckel E, Boselli F, Roth S, Krudewig A, Belting HG, Charvin G, et al. Oscillatory Flow Modulates Mechanosensitive klf2a Expression through trpv4 and trpp2 during Heart Valve Development. Current biology : CB. 2015;25(10):1354-61.
122. Hove JR, Koster RW, Forouhar AS, Acevedo-Bolton G, Fraser SE, Gharib M. Intracardiac fluid forces are an essential epigenetic factor for embryonic cardiogenesis. Nature. 2003;421(6919):172-7.
123. Vermot J, Forouhar AS, Liebling M, Wu D, Plummer D, Gharib M, et al. Reversing blood flows act through klf2a to ensure normal valvulogenesis in the developing heart. PLoS biology. 2009;7(11):e1000246.
124. Hierck BP, Van der Heiden K, Poelma C, Westerweel J, Poelmann RE. Fluid shear stress and inner curvature remodeling of the embryonic heart. Choosing the right lane! TheScientificWorldJournal. 2008;8:212-22.
125. Anton H, Harlepp S, Ramspacher C, Wu D, Monduc F, Bhat S, et al. Pulse propagation by a capacitive mechanism drives embryonic blood flow. Development. 2013;140(21):4426-34.
126. Boselli F, Freund JB, Vermot J. Blood flow mechanics in cardiovascular development. Cellular and molecular life sciences : CMLS. 2015;72(13):2545-59.
127. Bagatto B, Burggren W. A three-dimensional functional assessment of heart and vessel development in the larva of the zebrafish (*danio rerio*). Physiological and biochemical zoology : PBZ. 2006;79(1):194-201.
128. Midgett M, Chivukula VK, Dorn C, Wallace S, Rugonyi S. Blood flow through the embryonic heart outflow tract during cardiac looping in HH13–HH18 chicken embryos. Journal of The Royal Society Interface. 2015;12(111):20150652.
129. Karakaya C, Goktas S, Celik M, Kowalski WJ, Keller BB, Pekkan K. Asymmetry in Mechanosensitive Gene Expression during Aortic Arch Morphogenesis. Scientific reports. 2018;8(1):16948.

130. Wang Y, Dur O, Patrick MJ, Tinney JP, Tobita K, Keller BB, et al. Aortic arch morphogenesis and flow modeling in the chick embryo. Annals of biomedical engineering. 2009;37(6):1069-81.
131. Midgett M, Goenezen S, Rugonyi S. Blood flow dynamics reflect degree of outflow tract banding in Hamburger–Hamilton stage 18 chicken embryos. Journal of The Royal Society Interface. 2014;11(100):20140643.
132. Poelma C, Van der Heiden K, Hierck B, Poelmann R, Westerweel J. Measurements of the wall shear stress distribution in the outflow tract of an embryonic chicken heart. Journal of the Royal Society Interface. 2010;7(42):91-103.
133. Yalcin HC, Shekhar A, McQuinn TC, Butcher JT. Hemodynamic patterning of the avian atrioventricular valve. Developmental dynamics : an official publication of the American Association of Anatomists. 2011;240(1):23-35.
134. Baek KI, Ding Y, Chang CC, Chang M, Sevag Packard RR, Hsu JJ, et al. Advanced microscopy to elucidate cardiovascular injury and regeneration: 4D light-sheet imaging. Progress in biophysics and molecular biology. 2018.
135. Fieramonti L, Foglia EA, Malavasi S, D'Andrea C, Valentini G, Cotelli F, et al. Quantitative measurement of blood velocity in zebrafish with optical vector field tomography. Journal of biophotonics. 2015;8(1-2):52-9.
136. Garita B, Jenkins MW, Han M, Zhou C, Vanauker M, Rollins AM, et al. Blood flow dynamics of one cardiac cycle and relationship to mechanotransduction and trabeculation during heart looping. American journal of physiology Heart and circulatory physiology. 2011;300(3):H879-91.
137. Hu N, Sedmera D, Yost HJ, Clark EB. Structure and function of the developing zebrafish heart. The Anatomical record. 2000;260(2):148-57.
138. Schwerte T, Fritsche R. Understanding cardiovascular physiology in zebrafish and xenopus larvae: the use of microtechniques. Comparative biochemistry and physiology Part A, Molecular & integrative physiology. 2003;135(1):131-45.
139. Taylor JM, Girkin JM, Love GD. High-resolution 3D optical microscopy inside the beating zebrafish heart using prospective optical gating. Biomedical optics express. 2012;3(12):3043-53.
140. Choi W, Kim HM, Park S, Yeom E, Doh J, Lee SJ. Variation in wall shear stress in channel networks of zebrafish models. Journal of the Royal Society, Interface. 2017;14(127).
141. Donnarumma D, Brodoline A, Alexandre D, Gross M. 4D holographic microscopy of zebrafish larvae microcirculation. Optics express. 2016;24(23):26887-900.
142. Brette F, Shiels HA, Galli GL, Cros C, Incardona JP, Scholz NL, et al. A Novel Cardiotoxic Mechanism for a Pervasive Global Pollutant. Scientific reports. 2017;7:41476.
143. Huang L, Xi Z, Wang C, Zhang Y, Yang Z, Zhang S, et al. Phenanthrene exposure induces cardiac hypertrophy via reducing miR-133a expression by DNA methylation. Scientific reports. 2016;6:20105.
144. Mu J, Wang J, Jin F, Wang X, Hong H. Comparative embryotoxicity of phenanthrene and alkyl-phenanthrene to marine medaka (*oryzias melastigma*). Marine pollution bulletin. 2014;85(2):505-15.
145. Zhang Y, Huang L, Wang C, Gao D, Zuo Z. Phenanthrene exposure produces cardiac defects during embryo development of zebrafish (*danio rerio*) through activation of MMP-9. Chemosphere. 2013;93(6):1168-75.

146. Zhang Z, Yan Q. Comparative toxicity of different crude oils on the cardiac function of marine medaka (*oryzias melastigma*) embryo. International Journal Bioautomation. 2014;18(4):389-96.
147. Padmanabhan A, Lee JS, Ismat FA, Lu MM, Lawson ND, Kanki JP, et al. Cardiac and vascular functions of the zebrafish orthologues of the type I neurofibromatosis gene NFI. Proceedings of the National Academy of Sciences of the United States of America. 2009;106(52):22305-10.
148. Matrone G, Wilson KS, Mullins JJ, Tucker CS, Denvir MA. Temporal cohesion of the structural, functional and molecular characteristics of the developing zebrafish heart. Differentiation; research in biological diversity. 2015;89(5):117-27.
149. Midgett M, Rugonyi S. Congenital heart malformations induced by hemodynamic altering surgical interventions. Frontiers in physiology. 2014;5:287.
150. Midgett M, López CS, Rugonyi S. 3D Imaging of the Early Embryonic Chicken Heart After Altered Blood Flow with Focused Ion Beam Scanning Electron Microscopy. Microscopy and Microanalysis. 2015;21(S3):909-10.
151. Poelmann RE, Gittenberger-de Groot AC, Hierck BP. The development of the heart and microcirculation: role of shear stress. Medical & biological engineering & computing. 2008;46(5):479-84.
152. Lindsey SE, Butcher JT, Yalcin HC. Mechanical regulation of cardiac development. Frontiers in physiology. 2014;5:318.
153. Boselli F, Vermot J. Live imaging and modeling for shear stress quantification in the embryonic zebrafish heart. Methods. 2016;94:129-34.
154. Jamison RA, Samarage CR, Bryson-Richardson RJ, Fouras A. In vivo wall shear measurements within the developing zebrafish heart. PloS one. 2013;8(10):e75722.
155. Lee J, Moghadam ME, Kung E, Cao H, Beebe T, Miller Y, et al. Moving domain computational fluid dynamics to interface with an embryonic model of cardiac morphogenesis. PloS one. 2013;8(8):e72924.
156. Bulk A, Bark D, Jr., Johnson B, Garrity D, Dasi LP. Mechanisms influencing retrograde flow in the atrioventricular canal during early embryonic cardiogenesis. Journal of biomechanics. 2016;49(14):3162-7.
157. Hsu JJ, Vedula V, Baek KI, Chen C, Chen J, Chou MI, et al. Contractile and hemodynamic forces coordinate Notch1b-mediated outflow tract valve formation. JCI insight. 2019;5.
158. Paolini A, Abdelilah-Seyfried S. The mechanobiology of zebrafish cardiac valve leaflet formation. Current opinion in cell biology. 2018;55:52-8.
159. Steed E, Boselli F, Vermot J. Hemodynamics driven cardiac valve morphogenesis. Biochimica et biophysica acta. 2016;1863(7 Pt B):1760-6.
160. Kowalski WJ, Dur O, Wang Y, Patrick MJ, Tinney JP, Keller BB, et al. Critical transitions in early embryonic aortic arch patterning and hemodynamics. PloS one. 2013;8(3):e60271.
161. Bark DL, Jr., Johnson B, Garrity D, Dasi LP. Valveless pumping mechanics of the embryonic heart during cardiac looping: Pressure and flow through micro-PIV. Journal of biomechanics. 2017;50:50-5.
162. Yalcin HC, Amindari A, Butcher JT, Althani A, Yacoub M. Heart function and hemodynamic analysis for zebrafish embryos. Developmental dynamics : an official publication of the American Association of Anatomists. 2017;246(11):868-80.
163. Combs MD, Yutzey KE. Heart valve development: regulatory networks in development and disease. Circulation research. 2009;105(5):408-21.

164. Singleman C, Holtzman NG. Analysis of postembryonic heart development and maturation in the zebrafish, *danio rerio*. Developmental dynamics : an official publication of the American Association of Anatomists. 2012;241(12):1993-2004.
165. Iwamatsu T. Stages of normal development in the medaka *oryzias latipes*. Mechanisms of development. 2004;121(7-8):605-18.
166. Taneda Y, Konno S, Makino S, Morioka M, Fukuda K, Imai Y, et al. Epigenetic control of cardiomyocyte production in response to a stress during the medaka heart development. Developmental biology. 2010;340(1):30-40.
167. Parker T, Libourel PA, Hetheridge MJ, Cumming RI, Sutcliffe TP, Goonesinghe AC, et al. A multi-endpoint in vivo larval zebrafish (*danio rerio*) model for the assessment of integrated cardiovascular function. Journal of pharmacological and toxicological methods. 2014;69(1):30-8.
168. Schwerte T, Pelster B. Digital motion analysis as a tool for analysing the shape and performance of the circulatory system in transparent animals. The Journal of experimental biology. 2000;203(Pt 11):1659-69.
169. Watkins SC, Maniar S, Mosher M, Roman BL, Tsang M, St Croix CM. High resolution imaging of vascular function in zebrafish. PloS one. 2012;7(8):e44018.
170. Lee SJ, Choi W, Seo E, Yeom E. Association of early atherosclerosis with vascular wall shear stress in hypercholesterolemic zebrafish. PloS one. 2015;10(11):e0142945.
171. Fujita M, Isogai S, Kudo A. Vascular anatomy of the developing medaka, *oryzias latipes*: a complementary fish model for cardiovascular research on vertebrates. Developmental dynamics : an official publication of the American Association of Anatomists. 2006;235(3):734-46.
172. Ando J, Nomura H, Kamiya A. The effect of fluid shear stress on the migration and proliferation of cultured endothelial cells. Microvascular research. 1987;33(1):62-70.
173. Peiffer V, Sherwin SJ, Weinberg PD. Does low and oscillatory wall shear stress correlate spatially with early atherosclerosis? A systematic review. Cardiovascular research. 2013;99(2):242-50.
174. Cecchi E, Giglioli C, Valente S, Lazzeri C, Gensini GF, Abbate R, et al. Role of hemodynamic shear stress in cardiovascular disease. Atherosclerosis. 2011;214(2):249-56.
175. Davies PF. Hemodynamic shear stress and the endothelium in cardiovascular pathophysiology. Nature clinical practice Cardiovascular medicine. 2009;6(1):16-26.
176. Sugii Y, Nishio S, Okamoto K. In vivo PIV measurement of red blood cell velocity field in microvessels considering mesentery motion. Physiological measurement. 2002;23(2):403-16.
177. Nakano A, Sugii Y, Minamiyama M, Niimi H. Measurement of red cell velocity in microvessels using particle image velocimetry (PIV). Clinical hemorheology and microcirculation. 2003;29(3-4):445-55.
178. Salman HE, Yalcin HC. Advanced blood flow assessment in Zebrafish via experimental digital particle image velocimetry and computational fluid dynamics modeling. Micron. 2020;130:102801.
179. Miller LA. Fluid dynamics of ventricular filling in the embryonic heart. Cell biochemistry and biophysics. 2011;61(1):33-45.
180. Lee J, Chou TC, Kang D, Kang H, Chen J, Baek KI, et al. A rapid capillary-pressure driven micro-channel to demonstrate newtonian fluid behavior of zebrafish blood at high shear rates. Scientific reports. 2017;7(1):1980.

181. Lee J, Fei P, Packard RR, Kang H, Xu H, Baek KI, et al. 4-Dimensional light-sheet microscopy to elucidate shear stress modulation of cardiac trabeculation. The Journal of clinical investigation. 2016;126(5):1679-90.
182. Lucitti JL, Jones EA, Huang C, Chen J, Fraser SE, Dickinson ME. Vascular remodeling of the mouse yolk sac requires hemodynamic force. Development. 2007;134(18):3317-26.
183. Teichert AM, Scott JA, Robb GB, Zhou YQ, Zhu SN, Lem M, et al. Endothelial nitric oxide synthase gene expression during murine embryogenesis: commencement of expression in the embryo occurs with the establishment of a unidirectional circulatory system. Circulation research. 2008;103(1):24-33.
184. Udan RS, Vadakkan TJ, Dickinson ME. Dynamic responses of endothelial cells to changes in blood flow during vascular remodeling of the mouse yolk sac. Development. 2013;140(19):4041-50.
185. Reifers F, Walsh EC, Leger S, Stainier DY, Brand M. Induction and differentiation of the zebrafish heart requires fibroblast growth factor 8 (fgf8/acerebellar). Development. 2000;127(2):225-35.
186. Huang Q, Fang C, Wu X, Fan J, Dong S. Perfluorooctane sulfonate impairs the cardiac development of a marine medaka (*oryzias melastigma*). Aquatic toxicology. 2011;105(1-2):71-7.
187. Ilagan R, Abu-Issa R, Brown D, Yang YP, Jiao K, Schwartz RJ, et al. Fgf8 is required for anterior heart field development. Development. 2006;133(12):2435-45.
188. Kashiwada S, Ariza ME, Kawaguchi T, Nakagame Y, Jayasinghe BS, Gartner K, et al. Silver nanocolloids disrupt medaka embryogenesis through vital gene expressions. Environmental science & technology. 2012;46(11):6278-87.
189. George V, Colombo S, Targoff KL. An early requirement for nkx2.5 ensures the first and second heart field ventricular identity and cardiac function into adulthood. Developmental biology. 2015;400(1):10-22.
190. Guner-Ataman B, Paffett-Lugassy N, Adams MS, Nevis KR, Jahangiri L, Obregon P, et al. Zebrafish second heart field development relies on progenitor specification in anterior lateral plate mesoderm and nkx2.5 function. Development. 2013;140(6):1353-63.
191. Tan X, Rotllant J, Li H, De Deyne P, Du SJ. SmyD1, a histone methyltransferase, is required for myofibril organization and muscle contraction in zebrafish embryos. Proceedings of the National Academy of Sciences of the United States of America. 2006;103(8):2713-8.
192. Doubilet PM, Benson CB. Embryonic heart rate in the early first trimester: what rate is normal? Journal of ultrasound in medicine : official journal of the American Institute of Ultrasound in Medicine. 1995;14(6):431-4.
193. Yu Q, Leatherbury L, Tian X, Lo CW. Cardiovascular assessment of fetal mice by in utero echocardiography. Ultrasound in medicine & biology. 2008;34(5):741-52.
194. De Luca E, Zaccaria GM, Hadhoud M, Rizzo G, Ponzini R, Morbiducci U, et al. ZebraBeat: a flexible platform for the analysis of the cardiac rate in zebrafish embryos. Scientific reports. 2014;4:4898.
195. Santhanakrishnan A, Miller LA. Fluid dynamics of heart development. Cell biochemistry and biophysics. 2011;61(1):1-22.
196. Fung Y-c. Biomechanics: motion, flow, stress, and growth: Springer Science & Business Media; 2013.
197. Nakamura M, Wada S, Yokosawa S, ISODA H, TAKEDA H, YAMAGUCHI T. Measurement of blood flow in the left ventricle and aorta using clinical 2D cine phase-

contrast magnetic resonance imaging. Journal of Biomechanical Science and Engineering. 2007;2(2):46-57.
198. Vasudevan V, Low AJJ, Annamalai SP, Sampath S, Poh KK, Totman T, et al. Flow dynamics and energy efficiency of flow in the left ventricle during myocardial infarction. Biomechanics and modeling in mechanobiology. 2017;16(5):1503-17.
199. Mankad R, McCreery CJ, Rogers W, Weichmann RJ, Savage EB, Reichek N, et al. Regional myocardial strain before and after mitral valve repair for severe mitral regurgitation. Journal of Cardiovascular Magnetic Resonance. 2001;3(3):257-66.
200. Kiserud T, Acharya G. The fetal circulation. Prenatal diagnosis. 2004;24(13):1049-59.
201. Leiva MC, Tolosa JE, Binotto CN, Weiner S, Huppert L, Denis AL, et al. Fetal cardiac development and hemodynamics in the first trimester. Ultrasound in obstetrics & gynecology : the official journal of the International Society of Ultrasound in Obstetrics and Gynecology. 1999;14(3):169-74.
202. Mommens M, Fernandes JM, Bizuayehu TT, Bolla SL, Johnston IA, Babiak I. Maternal gene expression in Atlantic halibut (Hippoglossus hippoglossus L.) and its relation to egg quality. BMC research notes. 2010;3:138.
203. Nesan D, Vijayan MM. Embryo exposure to elevated cortisol level leads to cardiac performance dysfunction in zebrafish. Molecular and cellular endocrinology. 2012;363(1-2):85-91.
204. Seppola M, Johnsen H, Mennen S, Myrnes B, Tveiten H. Maternal transfer and transcriptional onset of immune genes during ontogenesis in Atlantic cod. Developmental and comparative immunology. 2009;33(11):1205-11.
205. Lin H, Hsu S, Hwang P. Maternal transfer of cadmium tolerance in larval Oreochromis mossambicus. Journal of Fish Biology. 2000;57(1):239-48.
206. Scherz PJ, Huisken J, Sahai-Hernandez P, Stainier DY. High-speed imaging of developing heart valves reveals interplay of morphogenesis and function. Development. 2008;135(6):1179-87.
207. Liu J, Stainier DY. Zebrafish in the study of early cardiac development. Circulation research. 2012;110(6):870-4.
208. Goenezen S, Rennie MY, Rugonyi S. Biomechanics of early cardiac development. Biomechanics and modeling in mechanobiology. 2012;11(8):1187-204.
209. Peshkovsky C, Totong R, Yelon D. Dependence of cardiac trabeculation on neuregulin signaling and blood flow in zebrafish. Developmental dynamics : an official publication of the American Association of Anatomists. 2011;240(2):446-56.
210. Sedmera D, Pexieder T, Vuillemin M, Thompson RP, Anderson RH. Developmental patterning of the myocardium. The Anatomical record. 2000;258(4):319-37.
211. Haack T, Abdelilah-Seyfried S. The force within: endocardial development, mechanotransduction and signalling during cardiac morphogenesis. Development. 2016;143(3):373-86.
212. Watanabe-Asaka T, Sekiya Y, Wada H, Yasuda T, Okubo I, Oda S, et al. Regular heartbeat rhythm at the heartbeat initiation stage is essential for normal cardiogenesis at low temperature. BMC Dev Biol. 2014;14:12.
213. Miura GI, Yelon D. A guide to analysis of cardiac phenotypes in the zebrafish embryo. Methods Cell Biol. 2011;101:161-80.
214. Liu J, Stainier DY. Tbx5 and Bmp signaling are essential for proepicardium specification in zebrafish. Circulation research. 2010;106(12):1818-28.

215. Bajoghli B, Aghaallaei N, Soroldoni D, Czerny T. The roles of Groucho/Tle in left-right asymmetry and Kupffer's vesicle organogenesis. Developmental biology. 2007;303(1):347-61.
216. Forouhar AS, Liebling M, Hickerson A, Nasiraei-Moghaddam A, Tsai HJ, Hove JR, et al. The embryonic vertebrate heart tube is a dynamic suction pump. Science. 2006;312(5774):751-3.
217. Eelen G, Treps L, Li X, Carmeliet P. Basic and Therapeutic Aspects of Angiogenesis Updated. Circulation research. 2020;127(2):310-29.
218. Nicoli S, Standley C, Walker P, Hurlstone A, Fogarty KE, Lawson ND. MicroRNA-mediated integration of haemodynamics and Vegf signalling during angiogenesis. Nature. 2010;464(7292):1196-200.
219. Li J, Hou B, Tumova S, Muraki K, Bruns A, Ludlow MJ, et al. Piezo1 integration of vascular architecture with physiological force. Nature. 2014;515(7526):279-82.
220. Chatterjee A. An introduction to the proper orthogonal decomposition. Current science. 2000:808-17.
221. Bernero S, Fiedler H. Application of particle image velocimetry and proper orthogonal decomposition to the study of a jet in a counterflow. Experiments in Fluids. 2000;29:S274-S81.
222. Druault P, Guibert P, Alizon F. Use of proper orthogonal decomposition for time interpolation from PIV data. Experiments in Fluids. 2005;39(6):1009-23.
223. Kefayati S, Poepping TL. Transitional flow analysis in the carotid artery bifurcation by proper orthogonal decomposition and particle image velocimetry. Medical engineering & physics. 2013;35(7):898-909.
224. Willert CE, Gharib M. Digital particle image velocimetry. Experiments in fluids. 1991;10(4):181-93.
225. Eckstein A, Vlachos PP. Assessment of advanced windowing techniques for digital particle image velocimetry (DPIV). Measurement Science and Technology. 2009;20(7):075402.
226. Scarano F. Iterative image deformation methods in PIV. Measurement science and technology. 2001;13(1):R1.
227. Astarita T. Analysis of weighting windows for image deformation methods in PIV. Experiments in fluids. 2007;43(6):859-72.
228. Meinhart CD, Wereley ST, Santiago JG. A PIV algorithm for estimating time-averaged velocity fields. J Fluids Eng. 2000;122(2):285-9.
229. Kähler CJ, Scharnowski S, Cierpka C. On the uncertainty of digital PIV and PTV near walls. Experiments in fluids. 2012;52(6):1641-56.
230. Westerweel J, Scarano F. Universal outlier detection for PIV data. Experiments in fluids. 2005;39(6):1096-100.
231. Shinneeb A, Bugg J, Balachandar R. Variable threshold outlier identification in PIV data. Measurement Science and Technology. 2004;15(9):1722.
232. Vlachos P. https://sourceforge.net/projects/qi-tools/ 2010 [
233. Hund S, Kameneva M, Antaki J. A quasi-mechanistic mathematical representation for blood viscosity. Fluids. 2017;2(1):10.
234. Etebari A, Vlachos PP. Improvements on the accuracy of derivative estimation from DPIV velocity measurements. Experiments in Fluids. 2005;39(6):1040-50.

235. Xue Z, Charonko JJ, Vlachos PP. Particle image pattern mutual information and uncertainty estimation for particle image velocimetry. Measurement Science and Technology. 2015;26(7):074001.
236. Kannojiya V, Das A, Das PK. Simulation of blood as fluid: A review from rheological aspects. IEEE Reviews in Biomedical Engineering. 2020.
237. Li C, Tan XF, Lim TK, Lin Q, Gong Z. Comprehensive and quantitative proteomic analyses of zebrafish plasma reveals conserved protein profiles between genders and between zebrafish and human. Scientific reports. 2016;6:24329.
238. Kesmarky G, Kenyeres P, Rabai M, Toth K. Plasma viscosity: a forgotten variable. Clinical hemorheology and microcirculation. 2008;39(1-4):243-6.
239. Egginton S. Blood rheology of Antarctic fishes: viscosity adaptations at very low temperatures. Journal of Fish Biology. 1996;48(3):513-21.
240. Chen CY, Patrick MJ, Corti P, Kowalski W, Roman BL, Pekkan K. Analysis of early embryonic great-vessel microcirculation in zebrafish using high-speed confocal muPIV. Biorheology. 2011;48(5):305-21.
241. Chen JC, Chen MY, Fang C, Zheng RH, Jiang YL, Zhang YS, et al. Microplastics negatively impact embryogenesis and modulate the immune response of the marine medaka Oryzias melastigma. Marine pollution bulletin. 2020;158:111349.
242. Li Y, Wang J, Yang G, Lu L, Zheng Y, Zhang Q, et al. Low level of polystyrene microplastics decreases early developmental toxicity of phenanthrene on marine medaka (Oryzias melastigma). J Hazard Mater. 2020;385:121586.
243. Sun L, Zuo Z, Chen M, Chen Y, Wang C. Reproductive and transgenerational toxicities of phenanthrene on female marine medaka (Oryzias melastigma). Aquatic toxicology. 2015;162:109-16.
244. Zheng Y, Li Y, Yue Z, Samreen, Li Z, Li X, et al. Teratogenic effects of environmentally relevant concentrations of phenanthrene on the early development of marine medaka (Oryzia melastigma). Chemosphere. 2020;254:126900.
245. Pfaffl MW. A new mathematical model for relative quantification in real-time RT-PCR. Nucleic acids research. 2001;29(9):e45.
246. Russell K, Eriksen M, Aaberge L, Wilhelmsen N, Skulstad H, Remme EW, et al. A novel clinical method for quantification of regional left ventricular pressure-strain loop area: a non-invasive index of myocardial work. European heart journal. 2012;33(6):724-33.
247. Cauwenberghs N, Tabassian M, Thijs L, Yang WY, Wei FF, Claus P, et al. Area of the pressure-strain loop during ejection as non-invasive index of left ventricular performance: a population study. Cardiovasc Ultrasound. 2019;17(1):15.
248. Edwards NFA, Scalia GM, Shiino K, Sabapathy S, Anderson B, Chamberlain R, et al. Global Myocardial Work Is Superior to Global Longitudinal Strain to Predict Significant Coronary Artery Disease in Patients With Normal Left Ventricular Function and Wall Motion. Journal of the American Society of Echocardiography : official publication of the American Society of Echocardiography. 2019;32(8):947-57.
249. El Mahdiui M, van der Bijl P, Abou R, Ajmone Marsan N, Delgado V, Bax JJ. Global Left Ventricular Myocardial Work Efficiency in Healthy Individuals and Patients with Cardiovascular Disease. Journal of the American Society of Echocardiography : official publication of the American Society of Echocardiography. 2019;32(9):1120-7.

250. van der Bijl P, Vo NM, Kostyukevich MV, Mertens B, Ajmone Marsan N, Delgado V, et al. Prognostic implications of global, left ventricular myocardial work efficiency before cardiac resynchronization therapy. European heart journal cardiovascular Imaging. 2019;20(12):1388-94.
251. Espe EK, Aronsen JM, Eriksen GS, Zhang L, Smiseth OA, Edvardsen T, et al. Assessment of regional myocardial work in rats. Circulation Cardiovascular imaging. 2015;8(2):e002695.
252. Hu N, Yost HJ, Clark EB. Cardiac morphology and blood pressure in the adult zebrafish. The Anatomical record. 2001;264(1):1-12.
253. Hein SJ, Lehmann LH, Kossack M, Juergensen L, Fuchs D, Katus HA, et al. Advanced echocardiography in adult zebrafish reveals delayed recovery of heart function after myocardial cryoinjury. PloS one. 2015;10(4):e0122665.
254. Sreyashi Chakraborty EA, Maria S. Sepulveda, Pavlos P. Vlachos. Hemodynamic dependence of mechano-genetic evolution of the cardiovascular system in Japanese Medaka Royal Society Interface (under review). 2021.
255. Charonko JJ, King CV, Smith BL, Vlachos PP. Assessment of pressure field calculations from particle image velocimetry measurements. Measurement Science and technology. 2010;21(10):105401.